Bioengineering single-protein wires

Marta Pozuelo Ruiz

ADVERTIMENT. La consulta d'aquesta tesi queda condicionada a l'acceptació de les següents condicions d'ús: La difusió d'aquesta tesi per mitjà del servei TDX (**www.tdx.cat**) i a través del Dipòsit Digital de la UB (**diposit.ub.edu**) ha estat autoritzada pels titulars dels drets de propietat intel·lectual únicament per a usos privats emmarcats en activitats d'investigació i docència. No s'autoritza la seva reproducció amb finalitats de lucre ni la seva difusió i posada a disposició des d'un lloc aliè al servei TDX ni al Dipòsit Digital de la UB. No s'autoritza la presentació del seu contingut en una finestra o marc aliè a TDX o al Dipòsit Digital de la UB (framing). Aquesta reserva de drets afecta tant al resum de presentació de la tesi com als seus continguts. En la utilització o cita de parts de la tesi és obligat indicar el nom de la persona autora.

ADVERTENCIA. La consulta de esta tesis queda condicionada a la aceptación de las siguientes condiciones de uso: La difusión de esta tesis por medio del servicio TDR (**www.tdx.cat**) y a través del Repositorio Digital de la UB (**diposit.ub.edu**) ha sido autorizada por los titulares de los derechos de propiedad intelectual únicamente para usos privados enmarcados en actividades de investigación y docencia. No se autoriza su reproducción con finalidades de lucro ni su difusión y puesta a disposición desde un sitio ajeno al servicio TDR o al Repositorio Digital de la UB. No se autoriza la presentación de su contenido en una ventana o marco ajeno a TDR o al Repositorio Digital de la UB (framing). Esta reserva de derechos afecta tanto al resumen de presentación de la tesis como a sus contenidos. En la utilización o cita de partes de la tesis es obligado indicar el nombre de la persona autora.

WARNING. On having consulted this thesis you're accepting the following use conditions: Spreading this thesis by the TDX (**www.tdx.cat**) service and by the UB Digital Repository (**diposit.ub.edu**) has been authorized by the titular of the intellectual property rights only for private uses placed in investigation and teaching activities. Reproduction with lucrative aims is not authorized nor its spreading and availability from a site foreign to the TDX service or to the UB Digital Repository. Introducing its content in a window or frame foreign to the TDX service or to the UB Digital Repository is not authorized (framing). Those rights affect to the presentation summary of the thesis as well as to its contents. In the using or citation of parts of the thesis it's obliged to indicate the name of the author.

Universitat de Barcelona
Departament de Química Física
Programa de doctorat: Biotecnologia

BIOENGINEERING SINGLE-PROTEIN WIRES

Memòria que presenta Marta Pozuelo Ruiz per optar al títol de Doctor per la Universitat de Barcelona

Directors:

Dr. ISMAEL DÍEZ PÉREZ
Professor del Departament de Química Física de la universitat de Barcelona

Dr. PAU GOROSTIZA LANGA
Professor ICREA. Institut de Bioenginyeria de Catalunya

Tutor:

PROF. FAUSTO SANZ CARRASCO
Catedràtic del Departament de Química Física de la universitat de Barcelona

Barcelona, març de 2017

Universitat de Barcelona
Facultat de Química
Departament de Química Física

Institut de Bioenginyeria de Catalunya
Nanoprobes and Nanoswitches group

BIOENGINEERING SINGLE-PROTEIN WIRES

Marta Pozuelo Ruiz
Barcelona, 2017

TESI DOCTORAL

Table of contents

PREFACE 1

A. OBJECTIVES

B. STRUCTURE

CHAPTER 1: INTRODUCTION 5

- 1.1. Electron Transfer in biology 8
  - 1.1.1. Biological Redox Components 8
    - 1.1.1.1. Energy storage and Release 8
    - 1.1.1.2. Electron Transfer through proteins 11
    - 1.1.1.3. Cupredoxins 12
    - 1.1.1.4. Azurin 14
- 1.2. Protein electron transfer theory 15
  - 1.2.1. Marcus theory 18
  - 1.2.2. Reorganization energy 20
  - 1.2.3. Tunnelling in proteins 21
  - 1.2.4. Protein electron pathways 23
  - 1.2.5. Electronic energy Landscapes 25
- 1.3. Bioelectronics: Strengths and weaknesses 25
- References 31

CHAPTER 2: TECHNIQUES 39

- 2.1. Structural Characterization techniques 41
  - 2.1.1. Fluorescence 41
  - 2.1.2. UV-vis Spectrophotometry 45
- 2.2. Electrical Characterization techniques 46
  - 2.2.1. Voltammetry electrochemistry 46
- 2.3. SPM techniques 48
  - 2.3.1. Our approach 49
  - 2.3.2. Electrochemical Scanning Tunneling Microscope (EC-STM) 51
- References 55

CHAPTER 3: BIOENGINEERING A MODEL REDOX-PROTEINS **59**
3.1. Standard protocol 62
3.2. Mutant 41: second metal coordination sphere 66
3.2.1. Mutagenesis, Expression and Production 68
3.2.2. Characterization 70
3.2.2.1. Structural characterization: Spectroscopic methods. 70
3.2.2.2. Electrochemical characterization 73
3.2.3. Metal/protein conjugation assays 75
3.3. Rationalizing Electron transfer (ET) through a redox/protein: other mutants 77
3.3.1. Mutagenesis, Expression and Production 79
3.3.2. Characterization 80
3.3.2.1. Structural characterization: Spectroscopic methods. 82
3.3.2.2. Electrochemical characterization 87
References 90

COMPUTATIONAL METHODS **95**
4.1. Visualization of the frontier orbitals and calculation of their energies for the studied protein fragment 97
4.2. Molecular Dynamics Simulations 100
4.2.1. MD simulations of Azurin in water: structural differences/similarities between Cu-Azurin, Wt and K41C mutant: 100
4.2.2. MD simulations of Wt-Azurin adsorption over Au (111): 104
4.2.3. Influence of a gold tip on the structural stability of the Azurin as a function of the tip indentation height: 108
References 110

SINGLE-PROTEIN WIRES **115**
5.1. Wt and K41C Azurin electron transport 117
5.1.1. Electrochemical gate-dependent single-protein transport 117
5.1.2. Temperature-dependent single-protein transport. 126

5.1.6. Blinking control experiments 129
5.1.4. Blinking of Apo-proteins 130
5.1.5. Analysis of the single-protein junction lifetimes 131
5.2. Electron transport of bioengineered D76C, S89C, and L120C Azurin variants 133
5.2.1. Electrochemical gate-dependent single-protein transport 133
5.2.2. Field Effect Transistor (FET) simulation 136
5.2.3. Blinking of Apo-proteins: 137
5.2.4. Analysis of the single-protein junction lifetimes for D76C, S89C and L120C 138
References 140

CONCLUSIONS 143

APPENDIX A: MOLECULAR DYNAMICS. SIMULATION DETAILS 147

APPENDIX B: SYMBOLS AND ABBREVIATIONS 151

APPENDIX C: PUBLICATION LIST 157

APPENDIX D: RESUMEN EN CASTELLANO 161

PREFACE

OBJECTIVES

The main goal of this thesis is to bioengineered single-protein wires. To this aim we selected Azurin protein as starting model, because is a well-studied small globular redox protein. Additionally is a robust protein that presents high 3D stability in front of time and temperature.

The specific objectives of this thesis have been:

i) Bioengineer Azurin mutants in order to insert anchoring groups (single point mutations in the outer shell) for wiring electrode-protein-electrode through site-directed mutagenesis protocol. The protocol will be modified to perform that task in a non-bioengineering lab.

ii) Structural and electrical characterization of the Azurin mutants to determine any disruption provoked by the point mutation.

iii) Study the 3D conformation changes produced by a single point mutation.

iv) Study the preferred orientation of wild type Azurin to anchor the electrode.

v) Characterized the electron transport as a function of the electrochemical gate potential in a single-protein wire.

vi) Characterized the electron transport as a function of the temperature in a single-protein wire.

STRUCTURE

This thesis has been organized in six chapters:

Chapter 1: An introduction to the role of electron transfer in biology: why is it important? What is the relevance of redox proteins? How they work? What are the fundamentals of the electron transfer processes in life? These questions and many others are answer in first introduction part.

On the other hand it was introduced the bioelectronics term and its importance as well as their main drawbacks.

Chapter 2: This chapter corresponds to the fundamentals of the techniques used in the thesis. It is explained how and why they are essential to develop our work.

Chapter 3: In this section is presented in detail the bioengineered processes as well as the results and their discussion.

Chapter 4: Correspond to a theoretic chapter done in collaboration with Juan Carlos Cuevas' group at the University Autónoma de Madrid. It was a key research part to support our results.

Chapter 5: Describes in detail how the single-protein wires are formed and their characterization of the electron transport.

Chapter 6: General conclusions of this thesis and future perspectives in the field.

At the end you will find in a compendium of appendixes the abbreviations and symbols used in the thesis, a publication list and a summary of the manuscript in Spanish.

1

INTRODUCTION

1. INTRODUCTION

Biological Electron Transfer (ET) is the key step in many basic cellular processes such as respiration and photosynthesis[1]. Nature has developed highly specialized molecular building blocks capable of transporting charge with unprecedented efficiency, i.e. fast and at long distances[2]. These building blocks are composed by many several proteins involved in the ET. Through the fundamental understanding of the mechanism behind protein ET, it will be able to correlate disruptions in the protein activity throw changes in the ET. But why is that important to localize an altered protein function? Because a malformed or a missing protein usually is related to a disease, such as: sickle cell disease (DNA mutation disrupt hemoglobin, so the blood vessels are unable to transport oxygen effectively); cystic fibrosis (a DNA mutation affects de protein in charge of sodium chloride move in and out of cells); Huntington's Disease (DNA mutation is translated in a protein disruption affecting a person's ability to think, talk, and move); etc[3–5].

Fundamental knowledge or identifying specific protein mutations are not the only gain from studying biological ET. Such knowledge can also be used to design bioelectronic devices, i.e. exploiting the ET molecular machinery in biology to our advantage since biological ET has been improved during thousands of years to achieve the most efficient behaviour. Therefore, it is necessary to put light into the ET mechanism to unveil what are the key parameters for the transduction of the electrical signal between the active biomolecules and the electrodes[6,7]. In other words, engineering the biomolecule-electrode interface could be the most difficult part, because the coupling of the biomolecule-electrode will define if they are able to communicate.

In addition to that, bioelectronics is also a way to comply with the increasingly demanding downsizing of the microelectronics industry. Having the latest bioelectronic advances focused on bottom-up perspectives[7], aiming for maximum sensitivities, high signal-to-noise ratios and enhanced efficiency in order to reduce energy consumption.

1.1. Electron Transfer in biology

1.1.1. Biological Redox Components

1.1.1.1. Energy storage and Release

As introduced previously, there are plenty of processes in life that requires the presence of electron transferases such as collagen synthesis, steroid metabolism, immune response, drug activation, neurotransmitter metabolism, nitrogen fixation, etc. However the most relevant ones are photosynthesis and respiration1, because of their role in the production of the major energy necessary to run the cell. In addition, aerobic respiration and photosynthesis are complementary processes. CO2 and H2O are the main nutritional components for photosynthetic organisms, which are at the same time the final products of the aerobic respiration (figure 1.1). The same holds in the opposite direction. Energy production is in charge of some catabolic cycles, they oxidize organic compounds to oxygen and water and obtained water soluble reductants. These reductants donate electrons to the mitochondrial inner membrane, which are managed by an ET chain and are accompanied by protons translocation. The complexity of the ET processes lies on the huge protein composition net that are responsible that the electron can move far distances within the minimum time with the highest efficiency. For example figure 1.2 shows the schema for the respiratory chain located at the inner mitochondrial memebrane8–10. It is possible to appreciate the complexity of the ET chain. It is formed by four complexes: Complex I with a weight of 600 KDa owns five iron-sulphur clusters and FMN (flavin mononucleotide); Complex II with a weight of 150 KDa have several iron-sulphur clusters, FAD (flavine adenine dinucleotide), and a cytochrome b568; Complex III with a weight of 250 KDa has an iron-sulphur centre and cytochromes b562, b560, c1; and Complex IV weight 200 KDa and contain at least two copper ions and cytochromes a and a3. Q is a prosthetic group that binds to complexes I, II, and III (this interaction may happen at a hydrophobic patch of the complexes). Cytochrome c is a small periplasmic protein, it has been largely studied and is the first example shown as electron transferase protein. Those proteins form a fifty percent of the inner membrane, which can diffuse laterally. As a summary, we can see that more than twenty redox centres form the complex pathway for the electron transport. This pathway is also determined by the redox potentials of each active site. On the other hand, photosynthesis11–16 plays a role of light harvesting for chemical energy production. But how does it happen? At the heart of a photosystem lies the reaction centre, which is an enzyme that uses light to reduce molecules (provide with electrons). This reaction centre is surrounded by light-harvesting complexes that enhance the absorption of light, which are composed by hundreds of pigments (such as chlorophylls, carotenoids, phycoerythrin, and phycocyanin) also called antennas. Then the light is transformed to chemical energy in the reaction centre. If we look closer this reaction, what happens when a phonon is capture by an antenna pigment is that the pigment is promoted to an excited state. This energy is transferred through several pigments till it reaches to the reaction centre. Then the reaction centre will transform this energy of the exited state into electrochemical potential energy. This contains a primary electron donor which will transfer an electron to a closer acceptor[17].

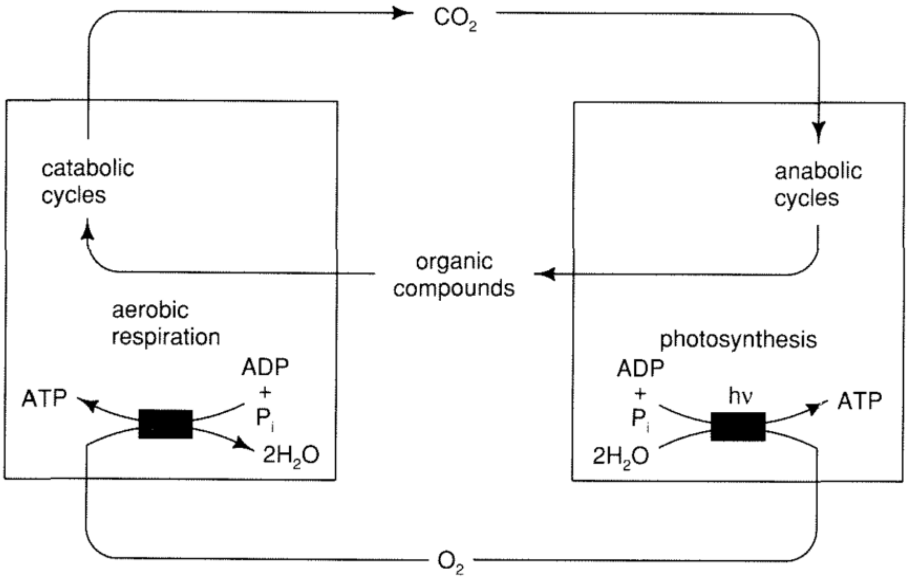
CO2
catabolic cycles
anabolic cycles
organic compounds
aerobic respiration
photosynthesis
ADP + Pi
ATP
2H2O
hv
ADP + Pi
ATP
2H2O
O2

Figure 1.1. Aerobic respiration and photosynthesis

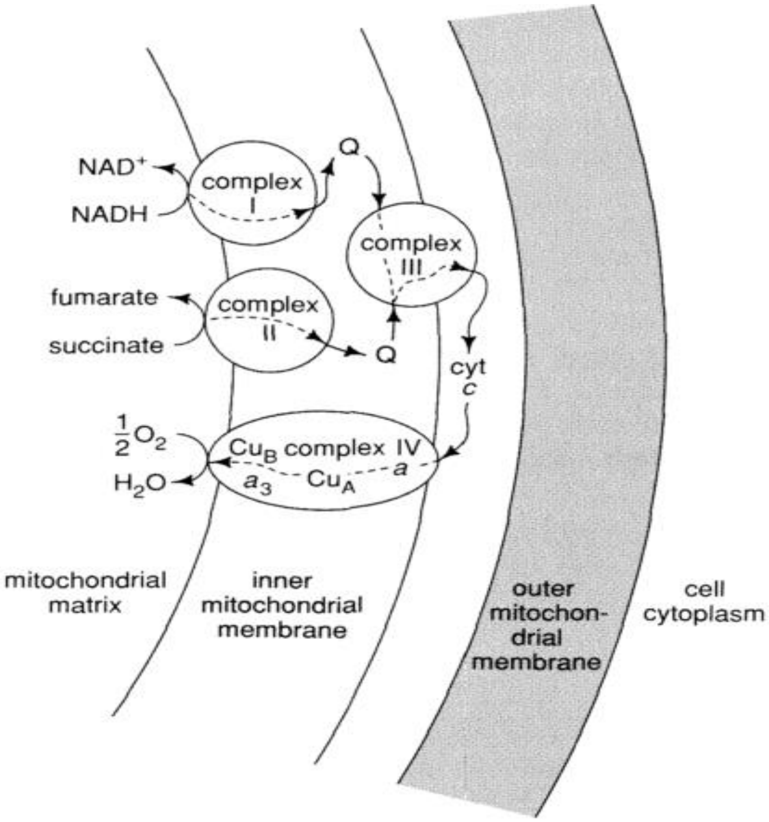
NAD+
NADH
complex I
Q
complex III
fumarate
succinate
complex II
Q
cyt c
1/2 O2
H2O
CuB complex IV
a3 CuA a
mitochondrial matrix
inner mitochondrial membrane
outer mitochondrial membrane
cell cytoplasm

Figure 1.2. Redox components in mitochondria.

Mother Nature has developed exceptionally efficient oxidation-reduction (redox) centres for ET process clustered inside the protein, which are known as metalloproteins or electron-transferases. The redox centre in metalloproteins plays the role of cofactor or prosthetic group[18], which are typically placed in a hydrophobic environment with additional hydrogen bonds provided from the peptide protein chain to assist in stabilizing both the oxidized and the reduced forms of the cofactor. Redox cofactor could be both a single metal ion directly coordinated to the protein peptide chain or a small complex with a metal ion that is clustered inside the protein. As we explain later, the metal-ligand bonds remain intact upon electron transfer to minimize inner-sphere reorganization. All kind of metalloproteins are sharing some common characteristic factors[19], even though they belong to different processes:

i) They own of a suitable cofactor to act as an electron sink.

ii) The cofactor is buried inside the protein peptidic matrix but close enough to the surface to allow electrons to move in and out.

iii) Existence of a hydrophobic shell adjacent to, but not always entirely surrounding, the cofactor

iv) Small structural changes accompanying electron transfer

v) An architecture that permits slight expansion or contraction in preferred directions upon electron transfer.

1.1.1.2. Electron Transfer through proteins

Redox proteins are on charge of ET processes and some can diffuse freely. In general big building blocks of proteins can diffuse somehow in the mitochondrial membrane, but some smaller ones, such as Cytochrome c, plastocyanin or ferrodoxin, are able to move through bigger distances within the cell to connect big protein complexes.

It is probed that proteins present highly specific recognition for their interactions, resulting in stable protein-protein complexes. However the interaction between redox proteins needs high affinity interactions to get a proper electron transfer. This is accomplished by the interaction of the region in the outer sphere close to the cofactor buried place. The orientation of the coupling and the nature of the interaction region play an important role. The more hydrophobic is the patch the stronger will be the coupling. Since it involves a highly specific recognition, which avoids non-desirable reactions, it implies a determined geometry. The electron will only propagate when for the exact coupling between active centres.

The stability of these protein complexes can vary from one protein to another. For example the photosynthetic reaction centre as well as some mitochondrial electron transport chains are enough stable in time to study the factors involved in electron transfer rates. Of course, there are several transiently stable complexes. Charged residues, the nature of the outer sphere surface topology and other geometric features are the responsible of the complex formation between redox partners. Moreover, after the complex formation, the electron transfer rate will be controlled by other set of factors, such as the difference between energetic levels of the oxidized and reduced states, the activation energy, the electronic coupling, and the reorganization energy.

Electron transfer is classified into different categories. One-electron carrier proteins form the simplest category. The electron is only transiently held in the protein cofactor, such as a metal atom or heme group. These are small proteins (8 – 15 KDa) with unique role of carry out electrons. Usually they are designed to interact specifically with different physiological partners. Cytochromes, cupredoxins and ferredoxins are some examples. Other categories more sophisticated will include two or more domains and they carry on with electron transfer and other roles (for example oxidation or reduction of organic substrates).

1.1.1.3. Cupredoxins

One of the most common electron transferases are formed by cuppredoxins[20]. Cupredoxins, also known as blue copper proteins, are electron transferases localized in plants and bacteria[21]. They own a single copper atom, which switch between cupric and cuprous states. As the concentration of copper can be dangerous it is highly controlled through a complex bioregulatory process. Cu (II)/(I) own the highest affinity for coordinate organic compounds. That is why copper is as useful in biology as a redox couple in oxidation-reduction processes. In addition, Cu(I) is a strong π-electron donor. Blue copper proteins is a quite large family of copper-containing electron transfer proteins found broadly in nature[22–24]. Having a small weight (10-20 KDa) they are responsible to connect bigger embedded protein complexes into the membrane. So they act as electron carriers between other larger proteins that are not able to move freely. They are characteristic for an intense Ligand-to-Metal Charge Transfer band absorption around 600 nm from the Cu → S(Cys), an uncommon small hyperfine coupling constant at an axial Electron Paramagnetic Resonance (EPR) spectrum, and high reduction potentials[25–27]. Through X-ray technique the general structure of the active sites was elucidate, which is close to trigonal planar[28]. This geometry is formed by the coordination of the copper with three ligands (two histidines and one cysteine). Also the copper could be bound to two extra axial ligands. Depending on the interactions between the ligands (commonly the axial are the weaker ones) the active centre could have different geometries. Also the weakness or strengthen of some ligands is directly related to the variations of the reduction potentials[28]. For example *Alcaligenes denitrijicans* Azurin (figure 1.3) presents 176 mV as redox potential while *Proteus vulgaris* plastocyanin has a higher one, 360 mV. The difference between both proteins lays in the distances bonds of Cu-S(Met) (longer for the *Alcaligenes denitrijicans* Azurin) and a carbonyl a bit closer to the Cu in Azurin than in plastocyanin. This length differences make the oxidation state more stable for *Alcaligenes denitrijicans* Azurin, and so that it has a lower reduction potential. The protein environment also has a role in the reduction potentials, and affects all electron transferases. Additionally hydrogen bonding, geometric constraints, electrostatic effects, and low dielectric constants are also determined factors. However these factors are not fully understood yet.

Both Azurin and plastocyanin are the most characterized. Plastocyanin plays its electron transfer role in the photosynthetic process in chloroplasts, connecting photosystem I to photosystem II; Azurin is thought to transfer electrons between cytochrome c-551 to cytochrome oxidase in bacteria. The typical secondary structure of blue copper proteins contains eight β-strands forming two twisted β-sheet structure sandwiching and hydrophobic interior. The copper ion is placed in a pocket at the 'northern' end of the sandwich, which is coordinated to amino acids from both β-sheets. The copper is coordinated in a distorted tetrahedron configuration, while in Azurin it has an extra ligand, a peptide carbonyl, which gives trigonal bipyramidal geometry. A rigid structure is achieved through a network of hydrogen bonding. The copper is buried in a hydrophobic patch; however it has a ligand (histidine) solvent accessible. This amino acid is at the same time surrounded by hydrophobic residues. This outer sphere patch is the responsible in most of the binding processes for electron transfer. As in Azurin no more sites were identify to such electron transfer, for plastocyanin a second site has been postulated. It consist on residues negatively charged surrounding a tyrosine residue[20].

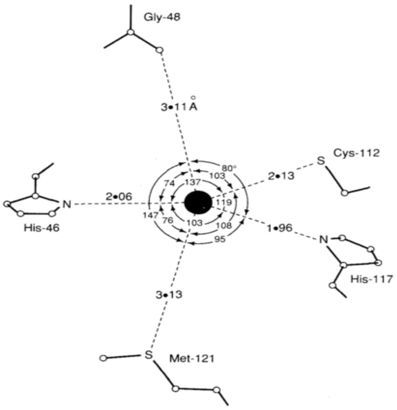

Figure 1.3. Structure of the blue copper centre in *Alcaligenes denitrijicans* Azurin.

1.1.1.4. Azurin

In this thesis we have selected Azurin protein form *Pseudomonas aeruginosa*. Azurin is a type 1 copper Azurin with three strong coordinated residues (His46, His117 and Cys112) and two weaker axial ligands (Gly45 and Met121) in a distorted tetrahedral geometry. This protein is a widely robust protein studied by several groups, which has been electrochemical and structural characterized both in bulk and at single molecules level[29–35]. Also it has been used widely as a scaffold for protein engineering efforts. Tuning redox potentials is easily done by exchanging residues of the second coordination sphere. In fact, it is probed the importance of the hydrogen bonding contributions and the hydrophobicity of the residues for increasing the redox potential. So that by playing with this parameters high redox potentials have been achieved, because of the additive behaviour of the effects of individual structural features[36,37]. Met121, a copper axial ligand and exposed to solvent residue, is a key amino acid for tuning redox values of Azurin[38], however is also a key residue to modify the active site. Having bioengineered met121 several groups have been switching the blue copper center into a red copper center[39] or a purple copper center (Cu_A)[40,41]. These studies have pointed out a number of roles the axial ligand can play in the blue copper centre, including steric protection of the copper ion from interaction with water and exogenous ligands[42–45], electronic modulation of the “in-plane” S(Cys)-Cu(II) interaction[46], control of the geometry of the blue copper center[47], and fine-tuning of the stability of the oxidation states of the copper ion and thus the reduction potential of the blue copper site.

1.2. Protein electron transfer theory

We have seen previously that both respiration and photosynthesis are such important processes in life. They involved a big deal of electron transfer. In both processes the redox potential gradient is correlated with the transmembrane proton gradient, which is known as chemiosmotic hypothesis[48]. This gradient is generated by membrane proteins in their role of electron transfer (between and within the proteins). The mechanism for this biological energy transduction is constructed by three components:

i) The motion of electron carriers between the major redox complexes.

ii) The coupling of electron and proton motion at the specific sites to control bond the formation/breaking chemistry.

iii) The tunnelling mechanism. This case involves the electron transfer through the medium without any electron transferase.

Actually, there is a lot of work to do because only the peak of the iceberg is seen nowadays. Since, the smallest protein involved in such complex processes has several thousands of atoms in a specific intricate configuration.

The iii) part is about electron tunnelling. But, how it works? Let's start for the simplest event where an electron tunnels. Considering an electron as a free particle, having a wavefunction, $|\psi 2(x)|$, that hits an 'impenetrable barrier', will be impossible for the electron to cross it according to classical mechanics theory. Since the electron has a lower energy, E, than the barrier potential, V. But Schrödinger equation does not permit the wavefunction to go to zero suddenly. So the wavefunction and its derivate must be continuous and derivate at all points. It is clearly seen that the wavefunction becomes a real exponential decay (figure 1.4). Quantum mechanics present a small but finite probability to find the electron inside the potential barrier, despite classical mechanics does not allow it. When the electron penetrates the potential barrier exist a chance for reaching another classical allowed region, which correspond to the process of the transmission of an electron from a donor to an acceptor[20].

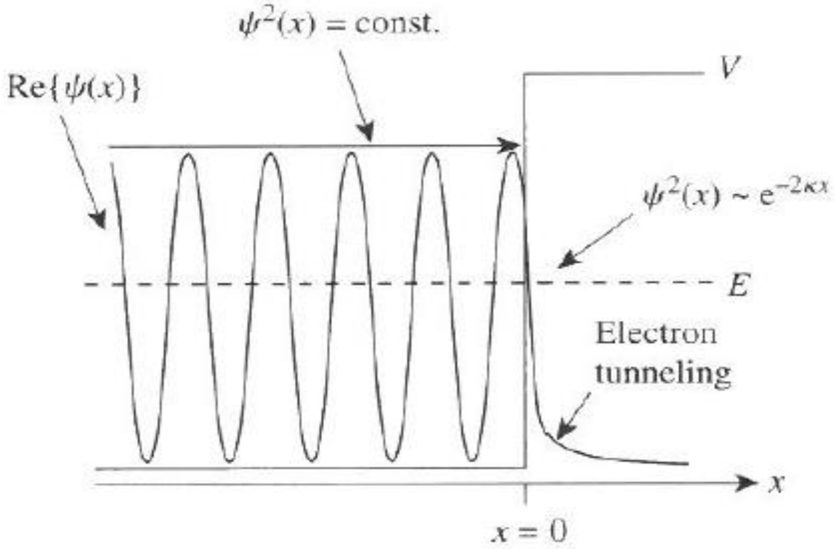

Figure 1.4. The real part of the wavefunction as a free particle (left of x = 0) impinging on a region where V > E and the electron is not classically allowed to enter is shown. The wavefunction has two components, a real part, oscillating like cos(kx) and an imaginary part oscillating like sin(kx) on the left of the barrier, and both swing between positive and negative values. The probability distribution is the square of these components, and it is constant on the left of the barrier (recall $\sin^2 + \cos^2 = 1$). The wave-matching requirements of the quantum mechanics imply some probability of finding the electron on the classically forbidden side of the barrier –a phenomenon called tunnelling. In the classically forbidden region on the right-hand side of the barrier, both the wavefunction and its square decay exponentially.

In the simplest quantum mechanical view the electron will go from the donor to the acceptor and then back to the donor, and so on when both energy wells are of the same magnitude. Actually in biology the energy wells of the acceptor and the donor are slightly different. This differing energies break up the resonance of the electron transfer, herein it will depend on time. The electron transfer rate is defined by the equation (1) for non-adiabatic electron transfers theory, also known as Fermi's golden rule:

$$k_{et} = \frac{2\pi}{\hbar} H_{AB}^2 \, FC \qquad (1)$$

where H^2_{AB} represents the square of the electronic coupling of the donor and the acceptor states which is related to the square of the integrated overlap of the donor and acceptor electronic wave functions, ħ is Planck’s constant and FC refers to the Franck-Condon weighted density of states. This only will be valid for systems where the donor and acceptor do not interact directly. Thus this is another adiabatic process[20].

At some points when a the second classical allowed region is placed close enough the electron will continue propagate through it due to the probability of the electron propagating through the barrier by tunnelling as shown in figure 1.5. This is the model that works for the STM system, where a free electron with a certain wavefunction and energy (E) hits a potential barrier of height V_0. As it exist a probability for electron propagation through the classical forbidden region by tunnelling, it will continue propagating as a free particle through the second region.

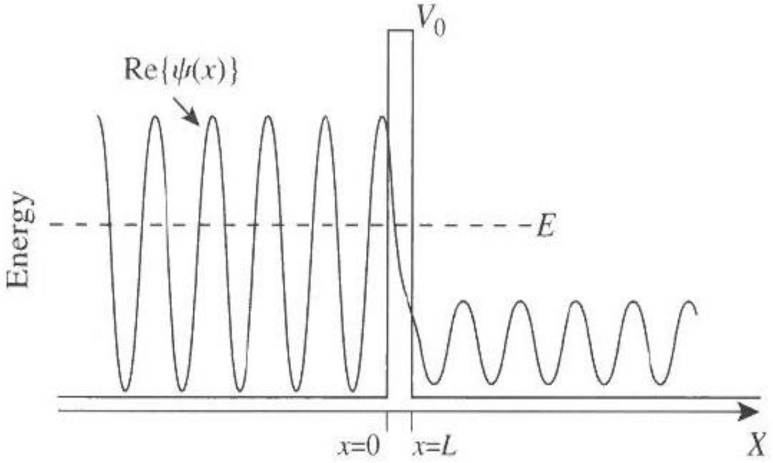

Figure 1.5. Electron penetration of a thin barrier as a model for the scanning tunnelling microscope. Just one component of the wavefunction is known. The vertical axis is energy (and also probability amplitude-the wavefunction oscillates between maximum + and – amplitudes). An electron is incident from the left on a classically forbidden region (V > E) but a second allowed region (V < E) is placed close enough such that there is a finite probability that electrons will propagate through the barrier by tunnelling. The form of the wavefunction is shown for one particular time.

1.2.1. Marcus theory

Having that the electron transfer is an outer sphere reaction, the molecule that owns the electron is stabilized by environmental polarization, which is a contribution of solvent polarization and polarization coming from bond distortions inside the molecule. All this polarization is storage of free energy. When the electron is transferred, not all the polarization is transferred and some work has to be done to restore it. This work is what is called reorganization energy, λ. Sometimes λ needs of geometry intramolecular modifications, which magnitude will depend on the system.

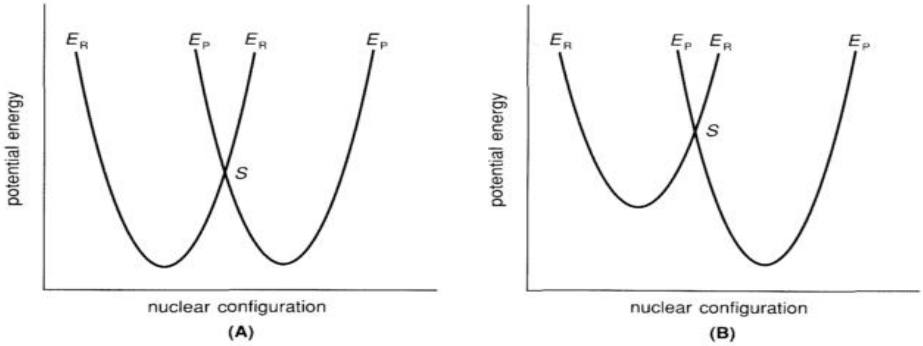

Figure 1.6. Potential energy diagram: (A) self-exchange reaction; (B) cross reaction. Point S represents the activated complex. E_R and E_P are the reactant and product surfaces, respectively.

Frank-Condon principle states that the electron transfer is happening so quickly that the system does not have enough time to be modified. In this manner the electron transfer happens at a non-variable nuclei configuration.

Marcus made an interpretation of Frank-Condon principle[49,50]. He represent with a single harmonic oscillator along a reaction coordinate, as the one for the product. Both minimum well correspond to the equilibrium state, having a lower energy the product and is displaced along the reaction coordinate to reach the equilibrium geometry. Geometry variation is correlated to the reorganization energy.

The Marcus theory states that the probability that an electron will transfer from a donor to an acceptor during a transition state decreases with increasing distance between the donor and acceptor. Factors that control the rate constant of electron transfer (ket) involved in a unimolecular electron transfer, in whom the probability of transfer from a donor to an acceptor is identified by the term kT/h, include: the distance between donor-acceptor complex; the Gibbs energy of activation; and the reorganization of energy. The distance between the donor-acceptor complexes (r) determines the probability of an electron transferring and is the general concept of Marcus theory of electron transfer. The Gibbs energy of activation (ΔG) is determined by the standard reaction Gibbs energy (ΔG°) and the reorganization energy (λ). The reorganization energy (λ) is an energy change resulting from the molecular rearrangement that occurs as the charge is distributed throughout the donor-acceptor complex in the medium[51]. The expression of the rate constant for electron transfer is given below:

$$k = e^{-\mathrm{\alpha r}} e^{-\mathrm{\alpha \Delta G/RT}} \qquad (2)$$

where r is distance between donor and acceptor, T is the temperature (a constant) and α is a constant dependent on the medium through which the electron must travel between the donor and the acceptor.

The activation energy, Ea, of the process corresponds to the intersection (S see figure 1.6) of both parabolas, taking as zero the minimum of the reactants. Ea will predict the rate of electron transfer. Also as reorganization energies will be lowered for electron transfer in unpolarizable environment because they need a minimum rearrangement (0.2 – 0.7 eV low[52] λ, while 1.4 eV high λ). Figure 1.6 suppose that electrons are confined on the donor or the acceptor while no ET is possible[17].

For non-adiabatic reactions (weak interactions between donor-acceptor complexes) need to cross the transition state many times before the electron is transferred. In that case the rate will depend on the electronic coupling. In this non-adiabatic reactions the electron is tunnelling through a certain potential barrier (non-classical allowed region) where the H_{AB} experiments, as a function of distance, an exponential decay. Herein the medium in the gap between donor-acceptor can control long range electron transfer. This system can be explained as an electron moving forward and backward. The electron will cross several times the intersection point till a weak coupling is stablished that allow the electron to transfer.

For adiabatic reactions -donor-acceptor are highly coupling by van der Waals interactions and the electron transfer is only limited by H_{AB}, which depends on the motion frequency along the reaction coordinate. So they are characterized by a transfer of the electron so rapidly due to the strong interaction between the donor and the acceptor. In figure 1.7 is possible to see the three different situations based on the region of the intersection of the reactant and product surfaces.

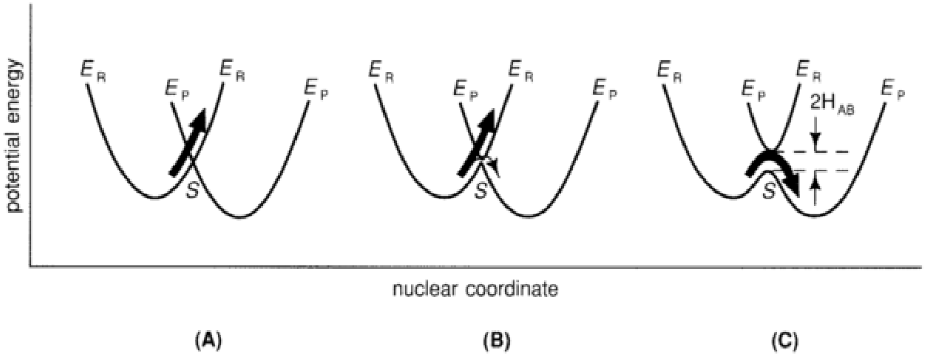

Figure 1.7. Potential energy diagrams: (A) $H_{AB} = 0$, $k = 0$ (no transfer); (B) H_{AB} small, $k << 1$ (nonadiabatic transfer); (C) H_{AB} large, $k = 1$ (adiabatic transfer). The arrows indicate the relative probability of crossing to the product surface (E_R to E_P).

1.2.2. Reorganization energy

Previously we have seen that for extremely rapid electron transfer the geometry of the donor-acceptor has no time to be affected. This system owns low reorganization energy because there is no such requirement of work to build up a stabilizing environment. So it is possible to relate low reorganization energy with a high efficient and ultrafast electron transfer. The reorganization energy in proteins is controlled by the folding[53,54]. As the activation centre is more clustered in a hydrophobic patch lower will be the reorganization energy. So that, the λ of the outer sphere can be decreased upon a 50%[55]. In addition, the λ of the inner-sphere could also be controlled by tightening the coordination environment around the active site[54]. The confinement of poorly redox centre results in an improvement of its efficiency. An excellent is example is copper. $Cu(Phe)_2^{++/+}$ present a λ ~2.4 eV, while Cu (II/I) in *Pseudomonas aeruginosa* has a decrease to 0.7 eV. This λ

decrease reflects the environmental change for copper, showing that such clustered enhance its stability[53].

Reorganization energies for electron transfer are estimated through two strategies:

i) Variations of the driving force versus variation of rates.

ii) Studying the electron transfer rates dependence on temperature. Only accurate λ are achieved for systems with a determined temperature dependence of the ΔGo.

1.2.3. Tunnelling in proteins

Intraprotein electron transfer follows Marcus-like free energy dependence. Many examples are found in photosynthetic reaction centers[56–65]. Since the tunnelling electron transfer occurs in the order of submillisecons, which implies that the cofactors should not be further than 17 Å. This distance plays a key role for the active site, because it is necessary to have it protected for any exogenous redox acceptor. This distance could be reduced for weaker reductant or oxidants. However when a protein is taken a role in interprotein electron transfer, it is essential that the cofactor is not more than 9 Å from the edge. So this distance has to be exploited for having the active site sheltered from the environment[20].

An example could be seen in cytochrome c, where the heme group is placed asymmetrically on one side of the protein at only 5 Å from the outer shell. Here the cofactor protects itself with the asymmetry, which ensures a specific binding site with its partner coupling protein. In addition to that, some strategic charged amino acids are placed around the cofactor that enhances the coupling with the desirable protein making them complementary.

In these proteins where the active sites are insulated between them, the electron transfer is happening without the formation of long-lives intermediate protein states. This long-range electron transfer between the donor and the acceptor jumps the energy gap of both frontier orbitals.

Tunnelling processes happens from cryogenic temperatures to room temperatures[66]. This insensitivity to temperature is what characterized the activationless processes and/or tunnelling. Electron transfer is composed by both the motion of the electron between donor-acceptor and the motion associated with the reorganization energy of the nuclei itself. Electron transfer in biology occurs commonly through weak interactions between donor-acceptor complexes. That is due to the buried cofactors inside the proteins that do not allow a direct interaction. They are non-adiabatic reactions which only depends on the nuclear barrier[50,66]. When the donor-acceptor complex is formed a singular geometry is achieved. At that point both energies for donor and acceptor are resonant and only at that instant the electron can tunnel.

Rates of tunnelling transitions (non-adiabatic reactions) can be described with the Fermi's golden rule, which sets the transition rate directly proportional to HDA (electronic coupling matrix) squared to the Franck-Condon nuclear factor[20,67–69]. The superexchange is qualitatively described by Hopfield. It is founded on the protein energetics of the electronics states[70]. Having the N_a and N_b atoms as localization for the donor and the acceptor, respectively, Hopfield estimated a value of 2 eV for the tunnelling barrier. Having 1 eV interaction between both orbitals in bonded contact, HDA is set as:

$$H_{DA} = \frac{2.7\ eV}{\sqrt{N_a N_b}} \exp[-0.72R] \tag{3}$$

The distance-decay exponent is $\sqrt{2\mathrm{m}_e E_{barrier}/\hbar}$ with $E_{\mathrm{barrier}} = 2$ eV. R corresponds to the separation between donor-acceptor centres. 2.7 eV factor is reduced to 1 eV when R ~ 1.5 A. For electron tunnelling through a square potential barrier (H^2_{DA}, for a non-adiabatic reaction) it appears a β of 1.44 Å^{-1}, while for H_{DA} is a β of 0.72 Å^{-1}.

Reorganization energy of electron transfer is predicted to be distance dependent for shorter distances[50]. Compared to the squared electronic factor, the Marcus regime gives an overall rate with stronger distance dependence.

For a structureless barrier model, equation (3) define the short-range (matching with atomic interaction energies) and long-range behaviours (an exponential decay factor). H^2_{DA} model of electron tunnelling in proteins neglects any variation providing from tunnelling barriers on the length scale of chemical bonds. However, as we see above the β can be doubled for electron propagation through space in comparison with the propagation through bond. However it is not that simple, because between donor-acceptor protein medium contributes bonded and non-bonded interactions. So that, how to take into consideration both contributions?

1.2.4. Protein electron pathways

The electron pathway involves two different kinds of steps: through-bond and through-space tunnelling. Each interaction owns a different decay factor. The coupling could be easily estimated by listing all the possible through-bond and through-space decay between every pair of atoms of the protein. There will be a predominant pathway connecting donor to acceptor that has a minimum value of β. β values are easily obtained from theoretical estimates as well as from experimental data. The electronic coupling will be dominated by one pathway, however it does not mean that if a connection is broken it is the electron transfer. At that point the electron will follow another way to reach the acceptor, since there are more alternatives.

Beratan and Onuchic had defined the tunnel pathway composed by different units: a covalent bond, a hydrogen bond, and through-space step (figure 1.8). If the decay factors are compared of the through-bond versus the through-space it could be easily seen that if the electron wants to jump through the space it has a bigger penalty. But why the electron propagates through-space if it takes a much bigger penalty (barrier about 8 eV) than through-bond (about 0.5 eV)? Because it is highly necessary since the distance between active sites through peptide bone could be amazingly long which is translated in unviable electron transfer[71]. This limitation creates the necessity to use ‘short cuts’. Through-space step is the ‘short cut’ used for electron propagation. Hydrogen bonding provides a short through-space interaction preferred rather than a van der Waal interaction (experimentally probed).

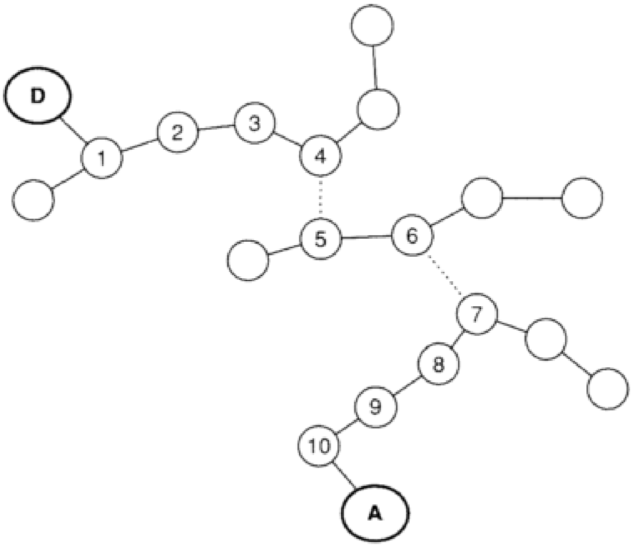

Figure 1.8. Example of a tunnelling pathway. The donor is coupled to the bonded pathway through bond 1 and the acceptor through bond 10. There are three bonded segments and two through-space jumps (between orbitals 4 and 5 and between orbitals 6 and 7).

Also they found that proteins with large β-sheet rather than α-helices were more effective in long-range couplings.

Five main points are characteristic for the pathway prediction[72,73]:

i) Coupling for donor-acceptor is obtained as an approximation from the product of the decay factors.

ii) Covalent and hydrogen bonds are priorized in front of van der Waals interactions.

iii) The coupling average comes from a balance between through bond and through-space decay.

iv) Decay coupling is anisotropic which gives ‘hot’ spots to electron transfer

v) The average distance decay is bond to the secondary structure of the protein.

1.2.5. Electronic energy Landscapes

As we previously seen, the simplest proteins acting as electron transferases are flavodoxins, blue copper proteins, iron-sulphur proteins, and cytochromes[20,67–69]. Their electron localizing groups in the electron transfer pathways have an energy window about 2 eV[74]. When the window is not enough reducing or oxidizing to react with the peptide backbone both tyrosines and tryptophans could host an electron. So that, proteins could be seen as semiconductors owing a wide band-gap, where the cofactor is the 'dopant' agent.

Then the electron can be localized at the active site, and despite being buried inside the protein (insulating environment), the electron is capable to 'jump' from one active site to another within picoseconds. How is it possible? Thanks to its wave character the electron is able to mix through the protein to tunnel between cofactors. Proteins assist the tunnelling providing localization sites for the electron, which is called super-exchange electron transfer[20,67–69,75]. Having big different energy values for each electronic orbitals of the protein and the cofactors exist a really low probability to find the tunnelling electron within the protein. The probability decay exponentially to the distance of localizing sites.

1.3. Bioelectronics: Strengths and weaknesses

Bioelectronics is an interdisciplinary field that is rising incredibly fast. It evolved from the need of understanding fundamental issues and its promising useful applications. It involves the combination of biomolecules with electronics[76–78], thanks to the nanotechnology advances.

But which is the reason to pick biomolecules and use them in electronics? Since Nature have achieved during thousands of years of evolution the perfect biocomponents, having enzymes (best catalytic molecules ever), and the biomolecules that owns the ability of both specific and selectively recognition of other targets (antigen-antibody, hormone-receptor, or duplex DNA complexes). Through intensive biochemical and biotechnological study of this biomolecules, it is possible to synthesize new biomolecules (such as enzymes, protein receptors, antibodies, etc.) through genetic engineering or bioengineering for its implementation in non-biological substrates. Having this source of new functional groups, opens a broad window to new applications.

As for its study and implementation some electronic elements will be involved: electrodes, field effect transistor devices, piezoelectric crystal, magnetoresistance recording media, scanning tunnelling microscopy (STM) probes and others.

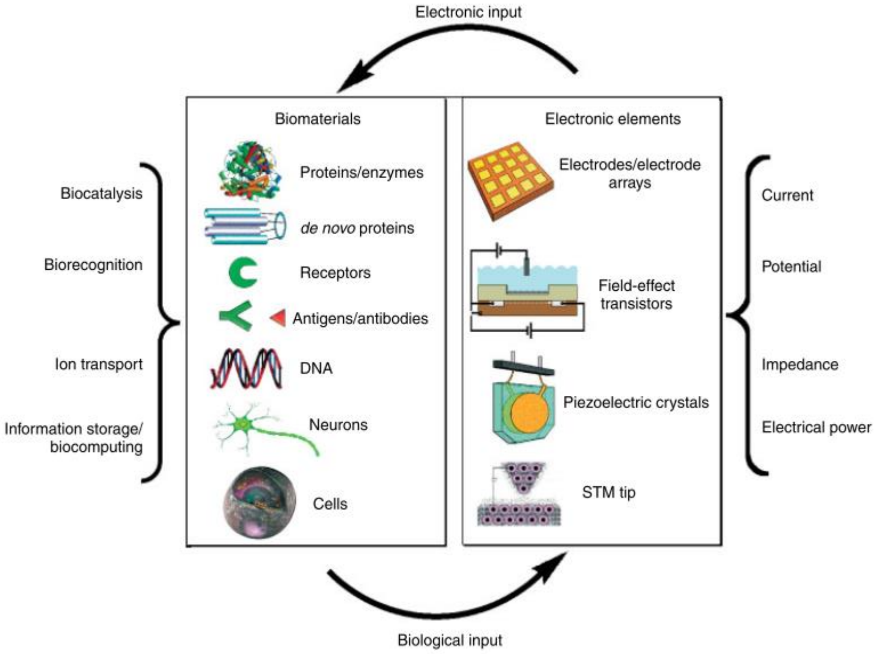
Electronic input
Biomaterials
Proteins/enzymes
de novo proteins
Receptors
Antigens/antibodies
DNA
Neurons
Cells
Electronic elements
Electrodes/electrode arrays
Field-effect transistors
Piezoelectric crystals
STM tip
Biocatalysis
Biorecognition
Ion transport
Information storage/ biocomputing
Current
Potential
Impedance
Electrical power
Biological input

Figure 1.9. Integrated systems of biomaterials and electronic elements for bioelectronics applications.

Bioelectronic devices need to operate in two ways. First, the bioelectronic system should be able to switch on the desired biomolecule function. And second, it needs a configuration where the biological element modifies the interfacial properties of the electronic component. This alteration has to be a complementary response to the reaction of the biomolecule, so its function could be transferred as readout signal like impedance, potential, charge transport, or any other electronic signal (figure 1.9).

The most studied process for bioelectronics are the ones involving biorecognition or biocatalysis, being able to transduce an electronic signal from the activity of the biomolecule attached to the device[79–81]. A lot of work has been done to push toward the conversion of organic fuel substrates into electrical energy[82,83].

The most important aspect in a bioelectronic system is the transduction issue. So it is a key step that a perfect coupling of the biomolecule with the electronic part is achieved. This essential part leaded to engineer special methods for immobilizing biomolecules on electronic solid supports without disrupting its native/inner activity. Of course the biomolecule should be stable on that conformation in quite long periods of time. Till now several inventive methods for biomolecule attachment have been reported[84]. The following step is to miniaturize the bioelectronic device, which required highly organized patterns of biomolecules on top of the electronic support.

The fundamental understanding of electron transfer in biological complexes has been studied during the past decades and is still an important issue nowadays, since there is a lot to discover yet. Both experimental and theoretical work is being developed to further investigate such efficient processes. As we have explained in the previous section Marcus theory[50], superexchange charge transport theory[85], and the definition of tunnelling pathways in proteins[86] has a big influence in the role of understanding how electron transfer processes occurs in some biology processes. For electron transfer processes studies a lot of work has been done in bioengineering metalloproteins. With experimental and theoretical coworking it is possible to face up the study of such electron flow in proteins[87]. For example DNA results in the previous years shows that it could behave as superconductive[88], conductive[89], semiconductive[90], and insulating[91] molecule. Different theories were ascribed for DNA electron transport explanation, including hopping mechanisms, tunnelling transport, or iron-assisted electron transfer[92,93].

As we mentioned before the coupling biomolecule-electrode is an essential characteristic for almost all bioelectronic systems. Several redox enzymes interact with other biological complexes to electron exchange. Between them we can recognize redox proteins, cofactors or molecule substrates. So that, if electrons are transferred from the electrode to the enzyme, which is coupling to the electrode, it could be possible to activate the biocatalytic function of it.

This may contribute with a new mechanism for some amperometric biosensors.

Nevertheless, there are some proteins which still do not have a proper coupling with the electrode. This lack of direct electron transfer communication between the interface biomolecule-electrode is one of the current problems to be solved in bioelectronics, which could be state as the major difficulty. Despite that interprotein electron transport is well defined by Marcus theory and also by spatial characteristic conformation of the active sites between biomolecules, it still is not clear in biomolecule-electrode interface.

Smart anchoring have been developed during the past years to anchor biomolecules for achieve a proper coupling. Those are some examples for interfacing biomolecules with electronic materials: steric alignment of proteins on electron relays associated with electrodes[94], immobilizing redox proteins in conductive polymers or redox active polymers[80], structural engineering of proteins with electron relays[95], and the incorporation of redox active intercalators in DNA[96].

As an example of engineered coupling of the hybrid is glucose oxidase. This molecule does not present a good communication with the electrode. To overcome that barrier it was incorporated inside a redox active biopolymer film, whose units are directly linked to the electrode surface. As the polymer units present some flexibility they are able to communicate electrically with the active site of the glucose oxidase. This is the main operation system of the already commercial glucose sensing devices. Nowadays its miniaturization is a fact; there are some implementations devices for continuous monitoring of glucose, which can be quite invasive so it is still a lot do.

Biofuel cells are another application for wiring enzymes to electronics. This technology is being widely studied, and its already well stablished, but there are lot to do for enhancing the energy yields conversions. This system involves two protein partners anchored to two electrodes, where energy is generated through the oxidation reduction process that happens at a catalytic anode and cathode, respectively.

2D and 3D nanostructures could be built up by self-organization of biomolecules, which forms channels or pores. This method is used for fabricating templates for other molecules achieving intricate structures. This particulars cavities are used as 'microreactors', because they own specific dimensions for synthesis of metallic or semiconductor nanodevices.

It seems to be really important for interface transducing the surface-to-volume size of the electronic part. It is the 'nanostructured' electronic part which is in charge of providing a high sensitive signal. So as bigger becomes the ratio less amount of analytes will be necessary to produce a detectable electrical signal. This is strongly related with the reduction of biomolecules required and the possibility to miniaturize the bioelectronic devices.

Nanoparticles constituted a kind of nanostructures with unprecedented electronic, optical, catalytic and photoelectrochemical properties[97–99]. They are in the same scale of sizes of enzymes, antigens/antibodies and DNA. New optoelectronic and electronic properties are found with the fusion of biomolecules with nanostructures, which has result in some bioelectronic applications[100]. Some examples for that hybrid combination are: the conjunction of redox enzymes with gold nanoparticles[101], or the photoelectrochemical assay of enzyme reactions by means of semiconductor nanoparticles[102].

Nanowires are a nanostructure that points to be perfect for connections in bioelectronics. And the best tool for their construction could be DNA[103]. Actually DNA can be easily controlled due to their characteristics: DNA sequences could be design in terms of base sequence and shape, could be manipulated with enzymes, metal ions could be bind to the phosphate units, molecular components could be specifically intercalate in DNA biopolymers, and they present specific DNA-protein interaction.

Neuronal networks are in being a big challenge for assembling with nanowires to get the challenging device that mimics brain functions such as information storage and processing memory devices. Figure 1.10 A shows one of the advances of the past twenty years. Neurons has been directly growth on top of electronic arrays to perform neurological functions[104]. Figure 1.10 B is a schema of how should work a processing device using neuronal network. Where a signal is received by a neuron from the electrode, the neuronal activity is transfer to the synapse to a second neuron cell that is linked to a transistor in charge of readout the signal. This kind of device will work as 'brain computers' as has been finding out recently.

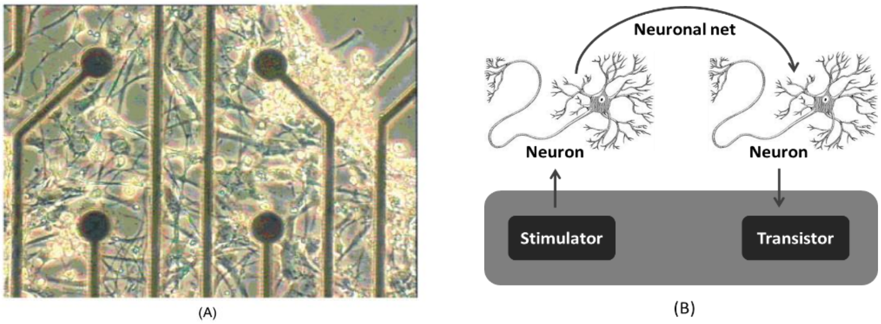

Figure 1.10. (A) Neurons on top of a multielectrode array. (B) A neuroelectronic hybrid system consisting of two neurons; the first neuron is activated by capacitive stimuli, the signal transmission occurs through a neuronal network to a second neuron, where the information is recorded by a transistor.

REFERENCES

1. Broda, E. *The evolution of the bioenergetic processes.* (Elsevier, 2014).
2. Gray, H. B. & Winkler, J. R. Long-range electron transfer. *Proc. Natl. Acad. Sci. U. S. A.* **102,** 3534–9 (2005).
3. Sue, C. M. & Schon, E. a. Mitochondrial respiratory chain diseases and mutations in nuclear DNA: a promising start? *Brain Pathol.* **10,** 442–450 (2000).
4. Stadtman, E. R. & Berlett, B. S. Reactive Oxygen-Mediated Protein Oxidation in Aging and Disease. *Drug Metab. Rev.* **30,** 225–243 (1998).
5. Gray, H. B. & Winkler, J. R. Electron flow through metalloproteins. *Biochim. Biophys. Acta - Bioenerg.* **1797,** 1563–1572 (2010).
6. *Bioelectronics: From Theory to Applications.* (John Wiley & Sons, 2006).
7. Zhang, A. & Lieber, C. M. Nano-Bioelectronics. *Chem. Rev.* **116,** 215–257 (2016).
8. Y., H. The mitochondrial electron transport and oxidative phosphorylation system. *Annu.Rev.Biochem.* **54,** 1015–1069 (1985).
9. Dixit, B. & Vanderkooi, J. in *Current Topics in Bioenergetics* 159–202 (Academic Press, 1984).
10. Jones, C. W. *Biological Energy Conservation.* (Chapman and Hall, 1981).
11. Clayton, R. K. *Photosynthesis: physixal mechanisms and chemical patterns.* (Cambridge University Press, 1980).
12. Fong, F. K. *Light Reaction Path of Photosynthesis.* (Springer-Verlag, 1982).
13. Clayton, R. K. & Sistrom, W. R. *The Photosynthetic Bacteria.* (Plenum, 1978).
14. in *Photosynthesis* (Academic Press, 1982).
15. Matthews, B. W. & Fenna, R. E. Structure of a green bacteriochlorophyll protein. *Acc. Chem. Res.* **13,** 309–317 (1980).
16. Deisenhofer, J., Epp, O., Miki, K., Huber, R. & Michel, H. X-ray structure analysis of a membrane protein complex. *J. Mol. Biol.* **180,** 385–398 (1984).
17. Raven, E., Le Brun, N. E., McMaster, J., Reedijk, J. & Robinson, N. J. *Bioinorganic chemistry. Dalton transactions (Cambridge, England : 2003)* **42,** (2013).
18. Hashmin, O. H. & Adnan, N. A. Coenzyme , Cofactor and

Prosthetic Ambiguous Biochemical Jargon. *Biochem. Educ.* **22,** 93–94 (1994).

19. Adman, E. T. A comparison of the structures of electron transfer proteins. *Biochim. Biophys. Acta* **549,** 107–144 (1979).
20. *Protein Electron Transfer.* (Bios Scientific Publishers, 1996).
21. Adman, E. T. Copper Protein Structures. *Adv. Protein Chem.* **47,** 145–197 (1991).
22. Farver, O. & Pecht, I. *Reactivity of copper sites in the blue copperproteins.* (1984).
23. Chapman, S. K. *Perspectives on Bioinorganic Chemistry. Blue copper proteins.* (Jai Press Inc., 1991).
24. Cotton, F. & Wilkinson, G. *Adavanced Inorganic Chemistry.* (John Wiley & Sons, 1988).
25. Gray, H. B. & Malmström, B. G. On the Relationship between Protein-Forced Ligand Fields and the Properties of Blue Copper Centers. *Comments Inorg. Chem.* **2,** 203–209 (1983).
26. Adman, E. T. *Metallopreoteins. Metal Proteins with Redox Roles.* (Macmillan, 1985).
27. Farver, O., Pecht, I. & Lontie, R. *Copper Proteins and Copper Enzymes.* (CRC Press, 1984).
28. Ainscough, E. W. *et al.* Spectrochemical studies on the blue copper protein azurin from Alcaligenes denitrificans. *Biochemistry* **26,** 71–82 (1987).
29. Amdursky, N. *et al.* Electronic Transport via Proteins. *Adv. Mater.* **26,** 7142–7161 (2014).
30. Jensen, P. S., Chi, Q., Zhang, J. & Ulstrup, J. Long-Range interfacial electrochemical electron transfer of Pseudomonas aeruginosa azurin-gold nanoparticle hybrid systems. *J. Phys. Chem. C* **113,** 13993–14000 (2009).
31. Fristrup, P. *et al.* Voltammetry of native and recombinant Pseudomonas aeruginosa azurin on polycrystalline Au- and single-crystal Au(111)-surfaces modified by decanethiol monolayers. *J. Electroanal. Chem.* **511,** 128–133 (2001).
32. Chi, Q., Zhang, J., Andersen, J. E. T. & Ulstrup, J. Ordered assembly and controlled electron transfer of the blue copper protein azurin at gold (111) single-crystal substrates. *J. Phys. Chem. B* **105,** 4669–4679 (2001).
33. Friis, E. P., Andersen, J. E. T.,

Madsen, L. L., Møller, P. & Ulstrup, J. In situ STM and AFM of the copper protein Pseudomonas aeruginosa azurin. *J. Electroanal. Chem.* **431,** 35–38 (1997).

34. Zhang, J., Kuznetsov, A. M. & Ulstrup, J. In situ scanning tunnelling microscopy of redox molecules. Coherent electron transfer at large bias voltages. *J. Electroanal. Chem.* **541,** 133–146 (2003).

35. Baldacchini, C., Bizzarri, A. R. & Cannistraro, S. Electron transfer, conduction and biorecognition properties of the redox metalloprotein Azurin assembled onto inorganic substrates. *Eur. Polym. J.* (2015). doi:10.1016/j.eurpolymj.2016.04.030

36. Marshall, N. M. *et al.* Rationally tuning the reduction potential of a single cupredoxin beyond the natural range. *Nature* **462,** 113–6 (2009).

37. Zanetti-Polzi, L. *et al.* A few key residues determine the high redox potential shift in azurin mutants. *Org. Biomol. Chem.* **13,** 11003–11013 (2015).

38. Garner, D. K. *et al.* Reduction potential tuning of the blue copper center in Pseudomonas aeruginosa azurin by the axial methionine as probed by unnatural amino acids. *J. Am. Chem. Soc.* **128,** 15608–15617 (2006).

39. Clark, K. M. *et al.* Transforming a Blue Copper into a Red Copper Protein:\rEngineering Cysteine and Homocysteine into the Axial\rPosition of Azurin Using Site-Directed Mutagenesis and\rExpressed Protein Ligation. *J. Am. Chem. Soc.* **132,** 10093–10101 (2010).

40. Hay, M. T. *et al.* Spectroscopic Characterization of an Engineered Purple Cu A Center in Azurin. *Inorg. Chem.* **37,** 191–198 (1998).

41. Hay, M., Richards, J. H. & Lu, Y. Construction and characterization of an azurin analog for the purple copper site in cytochrome c oxidase. *Proc. Natl. Acad. Sci. USA* **93,** 461–464 (1996).

42. Kroes, S. J. *et al.* The mutation Met121-->His creates a type-1.5 copper site in Alcaligenes denitrificans azurin. *Eur. J. Biochem.* **240,** 342–51 (1996).

43. Bonander, N., Karlsson, B. G. & Vänngård, T. Environment of copper in Pseudomonas aeruginosa azurin probed by binding of exogenous ligands to Met121X (X = Gly, Ala, Val, Leu, or Asp) mutants. *Biochemistry* **35,**

2429–2436 (1996).

44. Tsai, L. C. *et al.* Mutant Met121Ala of Pseudomonas aeruginosa azurin and its azide derivative: Crystal structures and spectral properties. *Acta Crystallogr. Sect. D Biol. Crystallogr.* **52,** 950–958 (1996).

45. Farver, O. *et al.* Intramolecular electron transfer in single-site-mutated azurins. *Biochemistry* **32,** 7317–7322 (1993).

46. Palmer, D. W. R. Spectroscopic studies and electronic structure description of the high potential T1 Cu site in fingal laccase. *Faseb J.* **13,** 7138–7149 (1999).

47. Messerschmidt, a *et al.* Rack-induced metal binding vs. flexibility: Met121His azurin crystal structures at different pH. *Proc. Natl. Acad. Sci. U. S. A.* **95,** 3443–8 (1998).

48. Mitchell, P. Coupling of phosphorylation to electron and hydrogen transfer by a chemi-osmotic type of mechanism. *Nature* **191,** 144–148 (1961).

49. Marcus, R. a. On the Theory of Oxidation-Reduction Reactions Involving Electron Transfer. I. *J. Chem. Phys.* **24,** 966 (1956).

50. Marcus, R. A. & Sutin, N. Electron transfers in chemistry and biology. *Biochim. Biophys. Acta* **811,** 265–322 (1985).

51. Atkins, P. & de Paula, J. *Atkins' Physical Chemistry.* (W. H. Freeman and Company).

52. Warshel, A., Chu, Z. T. & Parson, W. W. Dispersed Polaron Simulations of Electron-Transfer in Photosynthetic Reaction Centers. *Science (80-.).* **246,** 112–116 (1989).

53. Winkler, J. R., Wittung-Stafshede, P., Leckner, J., Malmström, B. G. & Gray, H. B. Effects of folding on metalloprotein active sites. *Proc. Natl. Acad. Sci. U. S. A.* **94,** 4246–4249 (1997).

54. Gray, H. B., Malmström, B. G. & Williams, R. J. Copper coordination in blue proteins. *J. Biol. Inorg. Chem.* **5,** 551–559 (2000).

55. Simonson, T. Gaussian Fluctuations and Linear Response in an Electron Transfer Protein. *Proc. Natl. Acad. Sci. U. S. A.* **99,** 6544–6549 (2002).

56. Bixon, M., Jortner, J. & Michel-Beyerle, M. E. A kinetic analysis of the primary charge separation in bacterial photosynthesis. Energy gaps and static heterogeneity. *Chem. Phys.* **197,** 389–404 (1995).

57. Dutton, P. L. & Mosser, C. C. Quantum biomechanics of long-range electron transfer in protein: hydrogen bonds and reorganization energies. *Proc. Natl. Acad. Sci. U. S. A.* **91,** 10247–10250 (1994).

58. Giangiacomo, K. M. & Dutton, P. L. In photosynthetic reaction centers , the free energy difference for electron transfer between quinones bound at the primary and secondary quinone-binding sites governs the observed secondary site specificity. **86,** 2658–2662 (1989).

59. Gunner, M. R. & Dutton, P. L. Temperature and -.DELTA.G.degree. dependence of the electron transfer from BPh.cntdot.- to QA in reaction center protein from Rhodobacter sphaeroides with different quinones as QA. *J. Am. Chem. Soc.* **111,** 3400–3412 (1989).

60. Gunner, R., Robertson, D. E. & Dutton, L. Kinetic Studies on the Reaction Center Protein from. 3783–3795 (1986).

61. Jia, Y. W. *et al.* Primary Charge Separation In Mutant Reaction Centers of Rhodobacter-capsulatus. *J Phys Chem* **97,** 13180–13191 (1993).

62. Lin, X. *et al.* Specific alteration of the oxidation potential of the electron donor in reaction centers from Rhodobacter sphaeroides. *Proc. Natl. Acad. Sci. U. S. A.* **91,** 10265–10269 (1994).

63. Lin, X., Williams, J. C., Allen, J. P. & Mathis, P. Relationship between rate and free energy difference for electron transfer from cytochrome c2 to the reaction center in Rhodobacter sphaeroides. *Biochemistry* **33,** 13517–13523 (1994).

64. Moser, C. C., Keske, J. M., Warncke, K., Farid, R. S. & Dutton, P. L. Nature of biological electron transfer. *Nature* **355,** 796–802 (1992).

65. Warncke, K. & Dutton, P. L. Influence of QA site redox cofactor structure on equilibrium binding, in situ electrochemistry, and electron-transfer performance in the photosynthetic reaction center protein. *Sect. Title Plant Biochem.* **32,** 4769–4779 (1993).

66. DeVault, D. *Quantum Mechanical Tunneling in Biological Systems.* (Cambridge University Press, 1984).

67. Bertini, I., Gray, H. B., Lippard, S. J. & Valentine, J. S. *Bioinorganic Chemistry.* (University Science Books,

1994).

68. *Electron transfer in Chemistry.* (Wiley).

69. Kuznetsov, A. M. & Ulstrup, J. *Electron Transfer in Chemistry and Biology: An Introduction to the Theory.* (John Wiley & Sons Inc, 1998).

70. Hopfield, J. J. Electron transfer between biological molecules by thermally activated tunneling. *Proc. Natl. Acad. Sci. U. S. A.* **71,** 3640–3644 (1974).

71. Beratan, D. N. & Onuchic, J. N. Electron tunneling pathways in proteins: influences on the transfer rate. *Photosynth. Res.* **22,** 173–186 (1989).

72. Beratan, D., Onuchic, J., Winkler & Gray, H. Electron-tunneling pathways in proteins. *Science (80-.).* **258,** (1992).

73. Beratan, D. N., Betts, J. N. & Onuchic, J. N. Protein Electron Transfer Rates Set by the Bridging Secondary and Tertiary Strcuture. *Science (80-.).* **252,** 1285–1288 (1991).

74. Cramer, W. A. & Knaff, D. B. *Energy Transduction in Biological Membranes.* (Springer-Verlag, 1990).

75. Mertzbacher, E. *Quantum Mechanics.* (Wiley, 1998).

76. Willner, I. Biomaterials for Fuel Sensors , Circuitry. *Science (80-.).* **298,** 2407–2408 (2002).

77. Nicolini, C. A. *Biophysics of Electron Transfer an dMolecular Bioelectronics.* (Plenum Press, 1998).

78. Hoffmann, K. H. *Coupling of Biological and Electronic Systems.* (Springer-Verlag, 2002).

79. Habermüller, K., Mosbach, M. & Schuhmann, W. Electron-transfer mechanisms in amperometric biosensors. *Fresenius. J. Anal. Chem.* **366,** 560–568 (2000).

80. Heller, A. Electrical wiring of redox enzymes. *Acc. Chem. Res.* **23,** 128–134 (1990).

81. Armstrong, F. a & Wilson, G. S. Recent developments in faradaic bioelectrochemistry. *Electrochim. Acta* **45,** 2623–2645 (2000).

82. Heller, A. Miniature biofuel cells. *Phys. Chem. Chem. Phys.* **6,** 209 (2004).

83. Katz, E., Shipway, A. N. & Willner, I. *Handbook of Fuel Cells – Fundamentals, Technology, Applications.* (Wiley, 2003).

84. Willner, I. & Katz, E. Integration of Layered Redox Proteins and Conductive Supports for Bioelectronic Applications.

Angew. Chem. Int. Ed. Engl. **39,** 1180–1218 (2000).

85. Bixon, M. & Jortner, J. *Electron Transfer—from Isolated Molecules to Biomolecules. Advances in Chemical Physics* (1999). doi:10.1002/9780470141656.ch3

86. Gray, H. B. & Winkler, J. R. Electron tunneling through proteins. *Q. Rev. Biophys.* **36,** 341–372 (2003).

87. Gray, H. B. & Winkler, J. R. Electron Transfer in Proteins. *Annu. Rev. Biochem.* **61,** 537–561 (1996).

88. Kasumov, A. Y. *et al.* Proximity-Induced Superconductivity in DNA. *Science (80-.).* **291,** 280–282 (2001).

89. Fink, H. W. & Schönenberger, C. Electrical conduction through DNA molecules. *Nature* **398,** 407–410 (1999).

90. Tran, P., Alavi, B. & Gruner, G. Charge Transport along the l -DNA Double Helix. *Phys. Rev. Lett.* **85,** 1564--1567 (2000).

91. De Pablo, P. J. *et al.* Absence of dc-conductivity in λ-DNA. *Phys. Rev. Lett.* **85,** 4992–4995 (2000).

92. Jortner, J., Bixon, M., Voityuk, A. A. & Rösch, N. Superexchange mediated charge hopping in DNA. *J. Phys. Chem. A* **106,** 7599–7606 (2002).

93. Schuster, G. B. & Landman, U. The Mechanism of Long-Distance\rRadical Cation Transport in Duplex DNA:\rIon-Gated Hopping of Polaron-Like Distortions. *Top Curr Chem* **236,** 139–161 (2004).

94. Willner, I. *et al.* Electrical wiring of glucose oxidase by reconstitution of FAD-modified monolayers assembled onto Au-electrodes. *J. Am. Chem. Soc.* **118,** 10321–10322 (1996).

95. Riklin, a, Katz, E., Willner, I., Stocker, a & Bückmann, a F. Improving enzyme-electrode contacts by redox modification of cofactors. *Nature* **376,** 672–675 (1995).

96. Patolsky, F., Katz, E. & Willner, I. Amplified DNA detection by electrogenerated biochemiluminescence and by the catalyzed precipitation of an insoluble product on electrodes in the presence of the doxorubicin intercalator. *Angew. Chemie - Int. Ed.* **41,** 3398–3402 (2002).

97. Khairutdinov, R. F. Physical-chemistry of nanocrystaline semiconductors. *Colloid J. Russ. Acad. Sci.* **59,** 535–548 (1997).

98. Mulvaney, P. Surface Plasmon Spectroscopy of

Nanosized Metal Particles. *Langmuir* **12,** 788–800 (1996).

99. Lewis, L. N. Chemical catalysis by colloids and clusters. *Chem. Rev. (Washington, DC, United States)* **93,** 2693–2730 (1993).

100. Katz, E., Shipway, A. N. & Willner, I. *Nanoparticles - Form Theory to Applications*. (Wiley-VCH, 2003).

101. Xiao, Y., Patolsky, F., Katz, E., Hainfeld, J. F. & Willner, I. 'Plugging into Enzymes': nanowiring of redox enzymes by a gold nanoparticle. *Science (80-.).* **299,** 1877–1881 (2003).

102. Pardo-Yissar, V., Katz, E., Wasserman, J. & Willner, I. Acetylcholine esterase-labeled CdS nanoparticles on electrodes: Photoelectrochemical sensing of the enzyme inhibitors. *J. Am. Chem. Soc.* **125,** 622–623 (2003).

103. Keren, K. Sequence specific molecular lithography on single DNA molecules. *Science (80-.).* **97,** 72–75 (2002).

104. Segev, R., Benveniste, M., Shapira, Y. & Ben-Jacob, E. Formation of electrically active clusterized neural networks. *Phys. Rev. Lett.* **90,** 168101 (2003).

2

TECHNIQUES

2. TECHNIQUES

Proteins have exceptionally well defined tertiary structures that make possible their roles within the cell. The structure is a key part in each protein, because small conformational variations can yield dramatic changes in their native activity. In fact, 3D conformation has been optimized for each specific protein to work properly in particular conditions of their environment. Surprisingly, outside the biological environment proteins appear to be more stable than was though[1]. This non-physiological stability along with their exceptional characteristics in electron transfer (ET)[2,3], catalyzing reactions, high specificity interactions, etc., make them promising for bioelectronics[4,3,5].

For that reason, a field in bioengineering proteins for the fundamental understanding and also for their connection in electronic components has been emerging. First the fundamental understanding of protein processes in biology is important not only to have more knowledge but also to advance in the design of biomolecule-electrode interface. At some points the protein-electrode fusion is not possible or do not has a good coupling to transduce signals in both directions. Here is where bioengineering makes it possible through some protein modifications. Although, those alterations could introduce structural changes that affect the native protein function. For that reason characterization techniques for both structural and functional protein properties are important in order to check that everything is working properly.

2.1. Structural Characterization techniques

2.1.1. Fluorescence

During the past years fluorescence has expand through many science fields from biotechnology, biochemistry, biophysics, and others, thanks to their highly sensitive detection, replacing other biochemical measurements involving radioactive tracers. By now fluorescence detection has become a primary technique in medical diagnosis, DNA sequencing, forensics, genetic analysis, cellular imaging, etc.

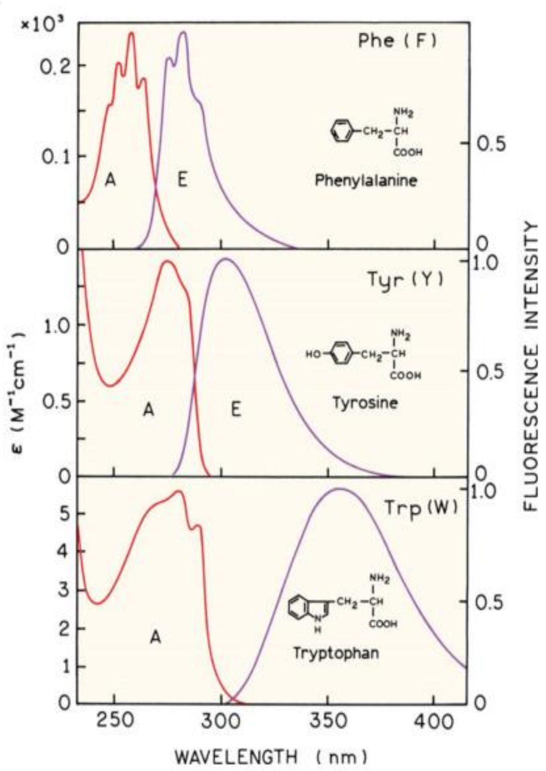

Figure 2.1. Absorption (A) and emission (E) spectra of the aromatic amino acids in pH 7 aqueous solution.

Protein fluorescence is originated by intrinsic aromatic amino acids tryptophan (trp), tyrosine (tyr) and phenylalanine (phe) (figure2.1). From them, trp is the one that stands out, because it is possible to be selectively excited at 295 nm without having extra contributions from tyr or phe. In addition the side chain of trp, indole group, is the dominant fluorophore in proteins. That is why the indole emission maximum is highly sensitive to the local environment, while tyr is insensitive. This high sensitivity of the fluorescence emission can be used as probe of the tertiary structure modifications, since any change from the native protein will be translate in a variation in the trp surrounding modifying the fluorescence emission[6] (figure 2.2). Trp emission in water occurs near 350 nm, but it could by quenched by proton transfer from nearby charge amino acids, electron acceptors, electron transfer by peptides bonds in the protein backbone and resonance energy transfer among the tryptophan residues modifying its maximum peak emission. Finally phe is only used as fluorescence marker when neither trp nor tyr are present in the protein because it has the shortest absorption and emission wavelength.

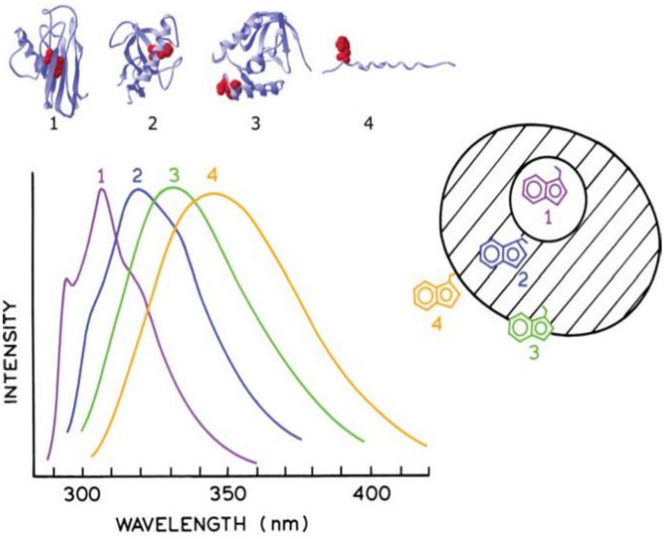

Figure 2.2. Effect of Tryptophan environment on the emission spectra. The emission spectra are those of apo-azurin Pfl, ribonuclease T_1, staphylococcal nuclease, and glucagon, for 1 to 4, respectively.

Azurin protein from *Pseudomonas aeruginosa* owns a single buried Trp48 in a hydrophobic region. The fluorescence emission for the native Azurin is around 300 nm when the indole is excited at 295 nm. Although exciting at 275 nm no fluorescence is visible from the tyr108 in this protein, the tyrosine is either quenched in the native structure or energy-transferred to the trp residue efficiently[6]. The trp48 fluorescence spectrum in this family of proteins is usually employed to get structural information. As we said previously, the trp48 fluorescence is shifted inside the hydrophobic core of the protein, having its maximum peak at 300 nm. So any change that structurally affects the 3D conformation of the Azurin will be visualized in a fluorescence emission peak shifted towards 350 nm[7,8]. The gradually trp48 exposure to the solvent by both chemical and thermal denaturation along with its fluorescence emission is shown in figure 2.3[9,7]. As the protein is unfolded the trp48 is exposed to aqueous solution quenching the trp48 fluorescence.

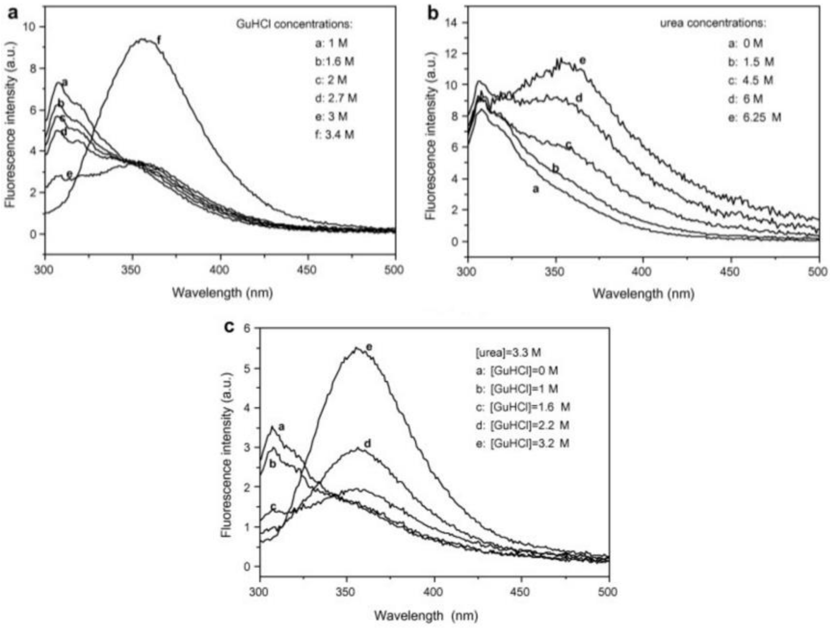

Figure 2.3. Denaturation of Azurin by (a) GuHCl; (b) urea, and (c) GuHCl plus urea[7]. (With permission from the journal).

Fluorescence information will tell that trp48 is being exposed, which means a partial modification in the structure, which at some point will be related to a fully or partially loss of the tertiary conformation. For instance, in the process of study the role of α-helix in Azurin, had driven to the entirely modification of the α-helix. The results show that the overall β-barrel structure is maintained, with a minor structural modification in the copper center. As a result they found a quenched fluorescence emission, which was red shifted to 334nm instead of the 308nm of the wild type[10]. That shows the importance and relevance of this technique as well as the necessity to use other complementary methods to build a proper conclusion upon structure modification.

2.1.2. UV-vis Spectrophotometry

UV-vis spectrophotometry is a measurement based on the light absorption of molecules in a range from 200 nm (in the near ultra-violet) to about 800 nm (in the very near infra-red), where only a limited number of the possible electron jumps absorb light in that region. As a result, a spectrum of absorbance versus the wavelength or frequency could be recorded.

In proteins the absorbance is a contribution from aromatic amino acids (trp, tyr and phe) and disulfide bonds of the protein structure. The resulting absorption peak is localized between 240 – 300 nm. Moreover the proteins containing a heme group or copper cofactors have extra absorption bands in the visible region[11].

In the literature we can find plenty of protein characterization using UV-vis measurements, because the shifts in the absorbance are related with structural changes in proteins. As an example, we show on figure 2.4 the UV-vis spectra for S-nitrosylation of *Pseudomonas aeruginosa* Azurin, which reaction converts a blue copper center of the Wt Azurin into a red copper center[12]. This center modification could be followed by UV-vis spectra thanks to the fact that Azurin has a Ligand-to-Metal Charge Transfer (LMCT) absorption bands at 600 nm that is shifted when the active site suffers any disruption.

Let's see the cause of this effect: the copper ion is strongly coordinated to Cys112, which results in a strong $p_{\pi(Cys)}$-to-Cu^{II} charge transfer band corresponding to the observed 600 nm absorption. This ligand field could be modified, for example, by strengthening axial interactions elongating Cu-S(Cys112) bond. This structure modification produces a rotation of the d_{x2-y2} ground state of the Cu^{II} ion leading to a better overlap with the p_{σ} orbital of the Cys112 instead of the p_{π}. This coupled distortion model results in a new absorption band at 400 nm due to the $p_{\sigma\ Cys)}$-to-Cu^{II} band while the 600 nm band decrease in intensity. This changes result in shifts of the LMCT band, which will provide structural information from the active site[13,14].

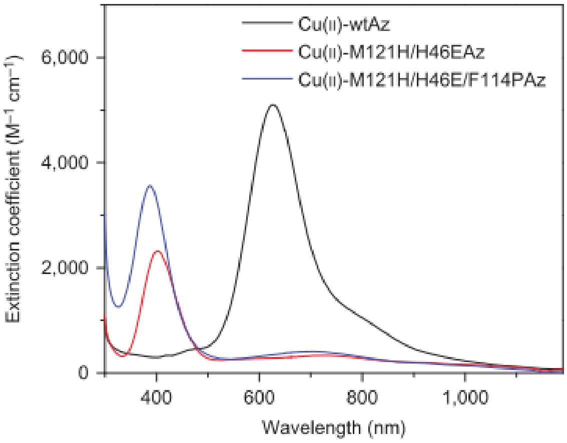

Figure 2.4. UV-vis absorption of S-nitrosylation in engineered red copper protein. UV–vis spectra of Cu(II)-WT Azurin, Cu(II)-M121H/H46EAz and Cu(II)-M121H/H46E/F114PAz. The S(Cys)→Cu(II) LMCT band of Cu(II)-M121H/H46E/F114PAz is at 390 nm, blue-shifted compared to WT Azurin, but identical to nitrosocyanin[12]

2.2. Electrical Characterization techniques

2.2.1. Voltammetry electrochemistry

As we state in chapter 1, redox proteins are excellent at long-range ET processes in different cell functions. They can be studied taking advance of this characteristic by direct electrochemistry. Redox proteins are attached to the surface electrode for a direct protein-surface exchange of electrons without any mediator. For that aim, some conditions should be accomplished. First, the protein has to be sufficiently stable at the electrode surface to avoid denaturation. And second, the ET at the interface has to be fast (reversible), which requires low reorganization energy and a high electronic coupling between protein-electrode[15].

Typical electrodes used for electrochemical determinations[16]:

i) Functionalized metal surfaces with monolayers that attached covalently to the surface and interacts usually with van der Waals interactions with a specific part (close to the redox active site) of the protein.

ii) Pyrolytic graphite edge or basal plane electrodes (such as platinum). Providing hydrophilic or hydrophobic interactions (respectively) are used with co-adsorbates (aminocyclitols, polymyxin, polylysine) for a cross-linkage with the protein onto the surface.

iii) Carbon-like electrodes (including nanostructured materials such as nanotubes) modified with aromatic groups to interact to a specific hydrophobic or carboxylate-rich patches in the protein outer shell.

iv) Various electrode materials covered with either non-biological surfactant (DDAB) or layers of polyions to incorporate large-membrane-bound proteins.

Voltammetry is being widely used to measure redox-oxidation potentials, which offers advantages over potentiometric titrations[15,17,16]:

i) Less sample concentration. As the protein is absorbed onto the surface electrode the concentration is much lower than the concentration required to get a signal from a bulk titration in solution

ii) It requires less time. Usually a single voltammogram takes a few seconds or minutes.

iii) As the sample is attached to the electrode it could be exposed to different environmental conditions. Samples can be tested in many buffers as long as the protein tolerates the conditions imposed.

iv) Reduction potentials could be study as a function of pressure or temperature.

v) There is no need to use data treatment for diffusion/convection phenomena of the proteins, so it is easier to analysis and model the data.

2.3. SPM techniques

The development of scanning probe microscopy (SPM) techniques had played an important role in the nanotechnology and nanobiotechnology fields. SPM has contributed to new opportunities in surface science, and especially in the characterization of single-biomolecules on surfaces (presents high spacial resolution) and also ET studies through single molecule junctions, being a key element for the demonstration of the long-range ET. Scanning tunneling microscopy (STM, was an invention of Gerd Binning and Heine Rohrer at IBM labs in Switzerland at 1979 being the father of the SPM group) can both image conductive substrates as well as measure tunneling currents versus voltage characteristics of a complex electrode/electrolyte interface.

Atomic force microscopy (AFM) is another SPM technique widely used for protein surface characterization[18]. AFM consist on a small probe attached to a cantilever for surface imaging. It scans the surface either in contact or in tapping mode, where the tip oscillates at a certain frequency close to the surface and their amplitude and oscillation phase register changes upon van der Waals forces. It allows topographic images, where single molecules are seen, and it is possible to measure biologically relevant forces/interactions on individual biomolecules between complementary protein pairs, such as antigen-antibody[19–23].

Another application of SPM techniques is the ability to pattern surfaces at the nanoscale including molecules. Figure 2.5a show a pattern elaborated with dip pen lithography, where each bright point corresponds to a single protein. The proteins are deposited through the AFM tip and they electrostatically interact with the surface[24]. Figure 2.5b corresponds to a DNA SAM patterned with a functionalized tip. Here instead of drop molecules, the molecule on the tip are reacting with the DNA (on top of the surface) which produce a pattern[25].

SPM techniques appear also as key techniques for the development of bioelectronics. SPM are essential for the characterization of the interfacial interactions as well as it fulfills the necessity to study at single molecule level (understand protein structure, explore use of protein properties for bioelectronics) for further miniaturization of the devices.

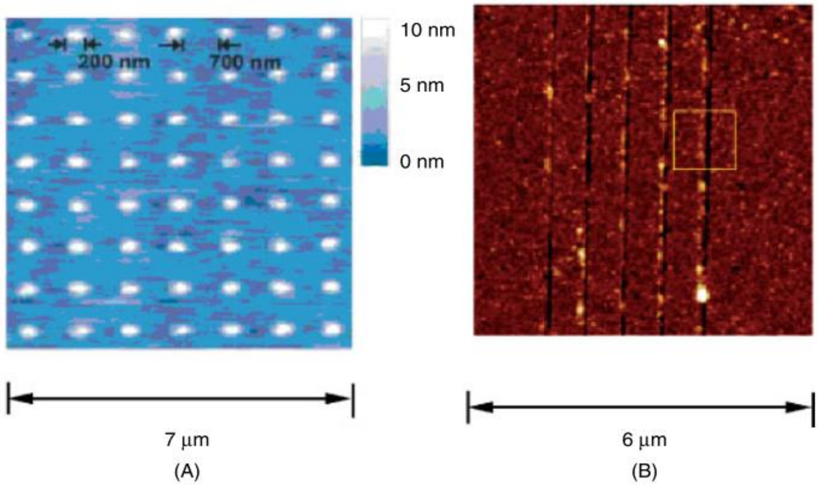

Figure 2.5. A) AFM image of a retronectin protein array generated by dip-pen nanolithography. B) AFM image of a patterned surface consisting of a DNA monolayer treated with a DNase-modified AFM tip that cleaves off the DNA units upon contact with the surface.

2.3.1. Our approach

Scanning tunneling microscopy (STM) has demonstrated its ability to not only image surfaces at the single atomic/molecular level but also it has shown capabilities to interact/manipulate at this level. These abilities have boosted the field of nanoscience and nanotechnology. The ability of atomic manipulation of a sample as well as the possibility to work under practical conditions, e.g. air, wet environment, etc. has facilitated the STM to overcome the electron microscopies in many applications.

In an STM, a metallic sharp probe is approached to a flat, clean surface. The STM probes have been usually prepared by electrochemically etched to get a sharp tip end (figure 2.6)[26]. The STM probe is approach to the surface till a set point tunneling current of few picoampers is reached. A feedback system is used to control the current flowing through the probe and as a function of it adjust the height of the probe, so as to keep the tunnel current constant. Because of the exponential dependence of the tunnel current on distance, every time the tip 'sees' a feature and the feedback loop modifies the height, the correction signal that is generated will be plotted as a spot of intensity. As a consequence of the strong exponential decay, only the closest atoms to the surface contribute to the tunnel resulting in atomic resolution. But the most important component is the piezoelectric scanning transducer. It controls the three directions of movement of the STM probe (x, y, z). As the piezoelectric component is very sensitive to potential changes the movements of the tip could be very accurately controlled which contributes to the atomic resolution.

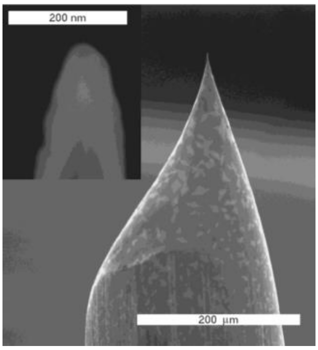

Figure 2.6. Scanning electron micrograph of an etched Pt-Ir tip showing the tip shape against the wire diameter. Inset: Magnification of the above micrograph showing the radius of the tip apex[26].

The tunneling current recorded from the scanning will be a convolution of the tunneling bias applied between the probe-sample, the sample topography, and the number of electronic states from the tip and the sample having energies close to the Fermi energy level. Also the 'direction' of the electrons could be controlled through the bias: from a negative bias most of the electrons are from the tip to the surface while at a positive bias it is inverted.

In fact we have selected STM technique to build single-protein wires due to the fact that is been used by several groups to form molecular wires. Nichols *et al.* have form short chain wires of polyporphyrins up to 10 nm long and they found low attenuation electron transport (ETp), which show their possible suitable future role in molecular electronics or photovoltaics devices[27]. In EC-STM Ulstrup and co-workers has been doing lot of work of single protein measurements combined with cyclic voltammetry. They had demonstrated controlled protein adsorption on a substrate[28,29]. Also previously in our group, EC-STM have been used for Azurin from *Pseudomonas aeruginosa* characterization[30–32]. So, we considered that STM could be a powerful technique for building our single-protein wires for ETp measurement since it has been largely used for characterization of ETp in a huge variety of molecules.

2.3.2. Electrochemical Scanning Tunneling Microscope (EC-STM)

In this thesis we want to obtain information on single-protein ETp behaviour over protein conformation fluctuations. For that purpose we have used Electrochemical Scanning Tunnelling Microscope (EC-STM) configuration since it allows to work under physiological conditions. In this ambient mode, an issue to control is the environmental perturbations since we are no longer controlling the atmosphere of the sample. It is easily solved by placing the STM onto a mechanism (figure 2.7) that owns an intrinsic resonant frequency (e.g. 1Hz) which absorbed any surrounding perturbation.

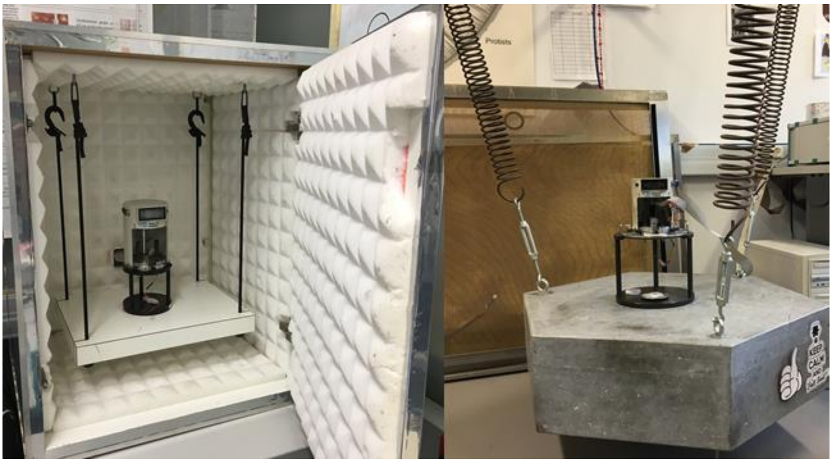

Figure 2.7. Two isolation systems are shown for the EC-STM. Both are based in the same concept of a platform (for the STM support) suspended from bungees (left image) or springs (right image).

For the EC-STM approach, both working electrodes (STM tip and conducting substrate) are set at different potentials independently control by a bipotentiostat. The difference between tip-substrate represents the STM tunneling bias. Two extra electrodes, reference and counter will be placed inside the electrolyte to opposite sides of the STM tip. The importance of the bipotentiostatic control raw on the ability to control the protein redox state (surface electrode potential) at the same time that the 'direction' of the current flow is set up (tip potential).

More concretely we have used to two EC-STM methodologies to study the conductance of the single-protein wires: the dynamic STM break-junction method (STM-BJ) and the static "blinking" STM method[31]. Shortly, in STM-BJ – a dynamic mode - the probe is approach to a tunnel distance from the sample and the feedback loop is turned off. Through a LabVIEW routine, a voltage is applied to the piezo so the STM tip is withdrawn and approached to the sample in order to form and break the contact between the STM tip and the Au substrate (figure 2.8). Current distance curves were recorded during the withdrawing stage, with only ~20% of them bearing steps or plateaus corresponding to the formation of a single-protein junction (figure 2.8). The conductance value of the single-protein junction is calculated through the expression $G=I_{step}/U_{bias}$. The ramps containing steps are used to construct the 1D histogram where a peak will represent the most probable single-protein conductance value. In contrast, in the "blinking" method – a static mode – the probe is set at tunnel distance from the sample and the feedback is turned off after a period of mechanical stabilization. Current versus time traces are then recorded in packets of few seconds during a total time of several hours.

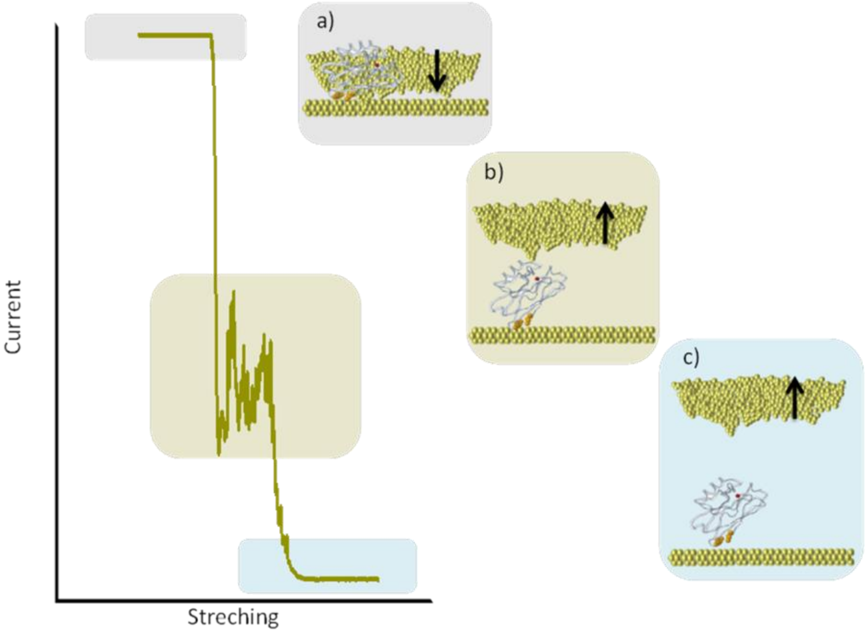

Figure 2.8. Scheme of a dynamic break junction (STM-BJ) experiment: a) tip approaching to the surface until a maximum feedback current is reached that sets the minimum STM tip-Au substrate separation; b) single molecule junction between tip and substrate. As the STM probe withdraws from the sample, chances are that a protein bridges and a plateau in the current shows up; c) the single-protein junction is broken and the current decays exponentially till zero as the tip goes out of the tunneling range.

When a protein spans the STM tip-substrate gap, a "jump" or "blink" is observed in the current transient in the form of telegraphic noise (Figure 2.9). Likewise, the current is transformed in conductance value of the single-protein junction using $G=I_{blink}/U_{bias}$. Up to a hundred of such blinks are used to build 2D blinking maps and its corresponding 1D conductance histogram without any data selection. 2D maps show the conductance versus the lifetime of the spontaneous junction, which provides extra information about the wire stability in contrast to 1D conductance histograms.

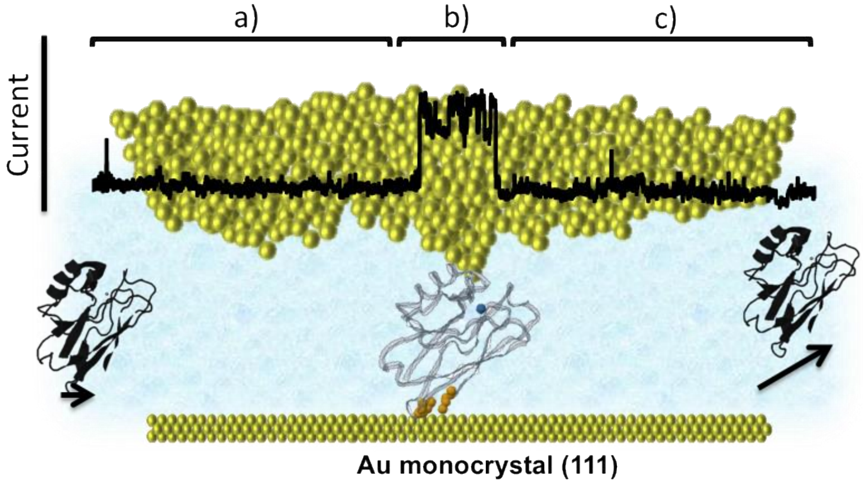

Figure 2.9. Scheme of a blinking experiment: a) the STM tip is set at a tunneling distance from the Au substrate (initial set point tunneling current) and the current feedback control is switched off; b) a protein bridge is established between the STM tip and the substrate with the corresponding change in the current ("blink"); c) the protein bridge eventually breaks and the current goes back to the initial tunneling set point value.

REFERENCES

1. Li, W. *et al.* Temperature and force dependence of nanoscale electron transport via the Cu protein azurin. *ACS Nano* **6,** 10816–10824 (2012).
2. *Bioelectronics: From Theory to Applications*. (John Wiley & Sons, 2006).
3. Zhang, A. & Lieber, C. M. Nano-Bioelectronics. *Chem. Rev.* **116,** 215–257 (2016).
4. D'Amico, S. *et al.* Ambipolar transistors based on azurin proteins. *IEEE Proc. nanobiotechnology* **151,** 173–175 (2005).
5. Gray, H. B. & Winkler, J. R. Electron Transfer in proteins. *Annu. Rev. Biochem.* **61,** 537–561 (1996).
6. Lakowicz, J. R. *Principles of Fluorescence Spectroscopy Principles of Fluorescence Spectroscopy. Principles of fluorescence spectroscopy, Springer, New York, USA, 3rd edn, 2006.* (2006). doi:10.1007/978-0-387-46312-4
7. Huang, Q. & Quiñones, E. Assessment of the stability and unfolding pathways of azurin from Pseudomonas aeruginosa through the combination of denaturating osmolytes. *Arch. Biochem. Biophys.* **477,** 175–182 (2008).
8. Fuentes, L., Oyola, J., Fernández, M. & Quiñones, E. Conformational changes in azurin from Pseudomona aeruginosa induced through chemical and physical protocols. *Biophys. J.* **87,** 1873–1880 (2004).
9. Guzzi, R., La Rosa, C., Grasso, D., Milardi, D. & Sportelli, L. Experimental model for the thermal denaturation of azurin: a kinetic study. *Biophys. Chem.* **60,** 29–38 (1996).
10. Manetto, G. D. *et al.* The role played by the helix in the unfolding pathway and stability of azurin: Switching between hierarchic and nonhierarchic folding. *ChemBioChem* **8,** 1941–1949 (2007).
11. Schmid, F. Biological Macromolecules : UV-visable Spectrophotometry. *Encycl. Life Sci.* 1–4 (2001). doi:10.1038/npg.els.0003142/abstrac
12. Tian, S. *et al.* Reversible S-nitrosylation in an engineered azurin. *Nat. Chem.* **8,** 670–677 (2016).
13. Clark, K. M. *et al.*

Transforming a Blue Copper into a Red Copper Protein:\rEngineering Cysteine and Homocysteine into the Axial\rPosition of Azurin Using Site-Directed Mutagenesis and\rExpressed Protein Ligation. *J. Am. Chem. Soc.* **132,** 10093–10101 (2010).

14. Abdelhamid, R. F. *et al.* π-π interaction between aromatic ring and copper-coordinated His81 imidazole regulates the blue copper active-site structure. *J. Biol. Inorg. Chem.* **12,** 165–173 (2007).
15. Armstrong, F. A. Voltammetry of proteins. *Encycl. Electrochem.* **Vol. 9,** 13–29 (2002).
16. Léger, C. An Introduction to Electrochemical Methods for the Functional Analysis of Metalloproteins. *Pract. Approaches to Biol. Inorg. Chem.* 179–216 (2013). doi:10.1016/B978-0-444-56351-4.00008-7
17. Fristrup, P. *et al.* Voltammetry of native and recombinant Pseudomonas aeruginosa azurin on polycrystalline Au- and single-crystal Au(111)-surfaces modified by decanethiol monolayers. *J. Electroanal. Chem.* **511,** 128–133 (2001).
18. Möller, C., Allen, M., Elings, V., Engel, A. & Müller, D. J. Tapping-Mode Atomic Force Microscopy Produces Faithful High-Resolution Images of Protein Surfaces. *Biophys. J.* **77,** 1150–1158 (1999).
19. Willemsen, O. H. *et al.* Biomolecular interactions measured by atomic force microscopy. *Biophys. J.* **79,** 3267–3281 (2000).
20. Albrecht, C. *et al.* DNA: A Programmable Force Sensor. *Science (80-.).* **301,** 367–370 (2003).
21. Nussio, M. R. *et al.* AFM study of the interaction of cytochrome P450 2C9 with phospholipid bilayers. *Chem. Phys. Lipids* **163,** 182–189 (2010).
22. Doan, T. T. *et al.* Electrochemical analysis of azurin thermodynamic and adsorption properties at monolayer-protected cluster film assemblies - Evidence for a more homogeneous adsorption interface. *J. Colloid Interface Sci.* **352,** 50–58 (2010).
23. Bayburt, T. H. & Sligar, S. G. Single-molecule Height Measurements on Microsomal Cytochrome P450 in Nanometer-Scale Phospholipid Bilayer Disks. *Proc. Natl. Acad. Sci.* **99,** 6725–6730 (2002).
24. Ginger, D. S., Zhang, H. &

Mirkin, C. A. The Evolution of Dip-Pen Nanolithography. *Angew. Chemie - Int. Ed.* **43,** 30–45 (2004).

25. Hyun, J., Kim, J., Craig, S. L. & Chilkoti, A. Enzymatic Nanolithography of a Self-Assembled Oligonucleotide Monolayer on Gold. *J. Am. Chem. Soc.* **126,** 4770–4771 (2004).
26. Güell, A. G., Díez-Pérez, I., Gorostiza, P. & Sanz, F. Preparation of reliable probes for electrochemical tunneling spectroscopy. *Anal. Chem.* **76,** 5218–5222 (2004).
27. Sedghi, G. *et al.* Long-range electron tunnelling in oligo-porphyrin molecular wires. *Nat. Nanotechnol.* **6,** 517–523 (2011).
28. Karlsson, J., Nielsen, M. F., Thuesen, M. H. & Ulstrup, J. Electrochemistry of Cytochrome c 4 from Pseudomonas stutzeri. *J. phys. chem.* **101,** 2430–2436 (1997).
29. Chi, Q. *et al.* Approach to Interfacial and Intramolecular Electron Transfer of the Diheme Protein\rCytochrome c4 Assembled on Au(111) Surfaces. *J. Phys. Chem. B* **114,** 5617–5624 (2010).
30. Artés, J. M. *et al.* Current-voltage characteristics and transition voltage spectroscopy of individual redox proteins. *J. Am. Chem. Soc.* **134,** 20218–20221 (2012).
31. Artés, J. M., Lõpez-Martínez, M., Díez-Pérez, I., Sanz, F. & Gorostiza, P. Conductance switching in single wired redox proteins. *Small* **10,** 2537–2541 (2014).
32. Artés, J. M., Díez-Pérez, I., Sanz, F. & Gorostiza, P. Direct measurement of electron transfer distance decay constants of single redox proteins by electrochemical tunneling spectroscopy. *ACS Nano* **5,** 2060–2066 (2011).

3

BIOENGINEERING A MODEL REDOX-PROTEINS

3. BIOENGINEERING A MODEL REDOX-PROTEIN

In this chapter, I will describe the bioengineering procedures to prepare the protein variants that will be studied in this thesis. The goal of the bioengineering part is to introduce an anchoring point in the protein outer shell to wire it between to gold electrodes (STM probe and sample electrode). Since we want to introduce an extra anchoring residue (exchange a selected residue for a Cys, due to it covalently anchor to the gold electrode) we need a robust protein upon structural modifications, that allow characterization with a wide range of techniques, and a robust structure for the lately absorption on gold electrodes. Azurin from *Pseudomonas aeruginosa* is our selected protein to work with. We have chosen this protein because is a widely studied model metalloprotein. This specific Azurin (type 1, 14KDa, 128 residues) is a small globular blue copper protein that has an electron carrier role in the respiratory chain of several bacteria. The copper is buried in a hydrophobic patch strongly coordinated to three residues (His46, His117 and Cys112) with two weaker axial contributions (Gly45 and Met121) in a distorted tetrahedral geometry[1] (figure 3.1). In the opposite surface of copper located metal-ion there is a disulphide bridge (Cys3-Cys26), which has been demonstrated to be an excellent anchoring point to gold surfaces[2]. Through STM imaging we have observed the individual proteins attached to the sample electrode (figure 5.2). Also it has been largely electrochemically and structurally characterized[2–6]. The ET between the copper to disulphide (Cys3-Cys26) has been analysed using fast photolysis approaches with mutated metal complexes[7]. Besides, its temperature stability has been observed to be very high up to 84ºC (irreversible denaturation of the protein structure)[8]. In addition, a wide variety of mutations have been performed on Azurin to study the effect of the α-helix, the β-sheet motifs and other key residues in the structural conformation and the electrochemical properties[9–19].

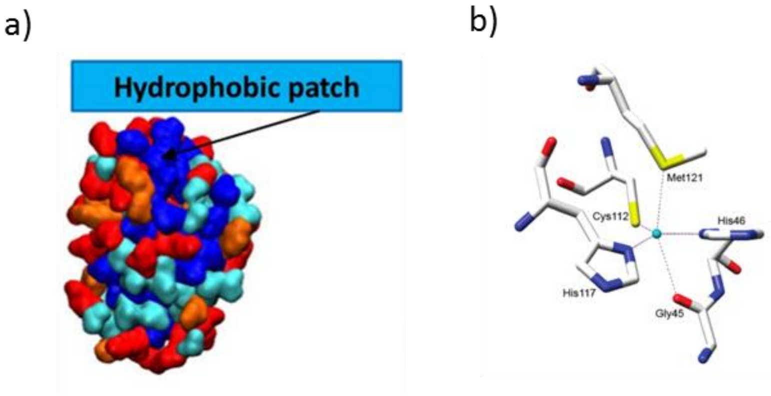

Figure 3.1. a) Residue distribution for all the Azurin structures colored in accordance with their hydrophobicity index: very hydrophobic (blue), hydrophobic (cyan), neutral (orange), and hydrophilic (red) residues. **b)** The coordinating ligands of the copper atom in the Azurin molecule (nitrogen atoms in purple, oxygen atoms in red, sulphur atoms in yellow, carbon atoms in white).

3.1. Standard protocol

I am going to briefly describe how we bioengineer and produce our protein mutants. It is important to mention here that a large part of this thesis implied setting up all bioengineering protocols in our laboratory.

Wt Azurin is a commercial product (Azurin from Pseudomonas aeruginosa, lyophilized powder from Sigma Aldrich). Dr. Jeff Warren (California Institute of Technology, Pasadena) kindly provided us the Wild type (Wt) Azurin gene (table 3.1) that was directly used to design and perform the mutagenesis.

The Azurin gene is inserted in a plasmid pet3a (figure 3.2). Pet3a is a small circular DNA molecule within the cell separated from the chromosomal DNA and its replications goes independently (it acts as an extra DNA sequence independent from the chromosomal DNA). It is used in bioengineering as a vector to introduced desired genes into the cells (namely also cell transformation). First, we have sequenced the Azurin gene to determine the nucleotide order that codes for the Azurin protein (every 3 base-pairs –codon- encodes for an amino acid). At some cases, when the protein is expressed in a non-native cell the third base pair of some codons are exchanged to a more suitable one for the new cell (different codons can encode for one amino acid). Sequencing requires a short oligonucleotide 'primer' complementary to the DNA template at the desired region (Azurin gene). We have chosen a primer called T7, which is a standard one for plasmids having T7 promoter part placed before de gene (figure 3.2). The results show that some codons have been modified its third base, because in this case Azurin comes from *Pseudomonas aeruginosa* and its being expressed at by *Escherichia coli* (*E. coli*) bacteria. This information is essential for the next step: design the point mutation.

We will exchange a single amino acid by a cysteine (Cys). That modification implies a maximum of three bases change in the gene. Two primers -backward and forward- were design for each protein mutant (two primers are needed one for each DNA strand). To maximize the success the primers must contain a high percentage of guanine (G) and cytosine (C), with a large amount in the extremes. This ensures a proper primer-gene coupling despite the mismatches (is not totally complementary to the gene, it incorporate different bases to code for cysteine residue instead of other selected residue).

We used QuikChange® Site-Directed Mutagenesis Kit for the Polymerase Chain Reaction (PCR). PCR is a technique used in molecular biology to amplify a piece of DNA across several orders of magnitude (figure 3.3). We placed a tiny DNA sample (pet3a containing the Azurin gene) with the designed primers together and we go straight with the exact temperatures, timings and cycles that the protocol kit recommended. All the mutated plasmids were inserted into E. coli through temperature shock. When the bacterial cells are exposed to temperature contrasts they 'open' their membranes to adsorb possible plasmids in the media. The aim is to search in those plasmids genes coding for proteins that makes them survive in the new conditions. At that point, we have the plasmid bearing the Azurin gene mutated, so we proceed with a plasmid preparation method for both amplify the DNA and select the correctly mutated (some plasmids will contain extra mutations, or erroneous ones). It consist on three main steps: i) insert the gene in a bacteria -in our case, we transform *E. coli* with pet3a vector coming out from the PCR- and grow a bacterial culture; ii) Harvest and cell lysis (breaking down the cell membrane); iii) purification of plasmid DNA (done with NucleoSpin Plasmid kit from Cultek) , it is ready to use for protein expression after its verification throw sequencing (this sequencing part is done with the T7 primer since it allows us to fully sequence the Azurin gene).

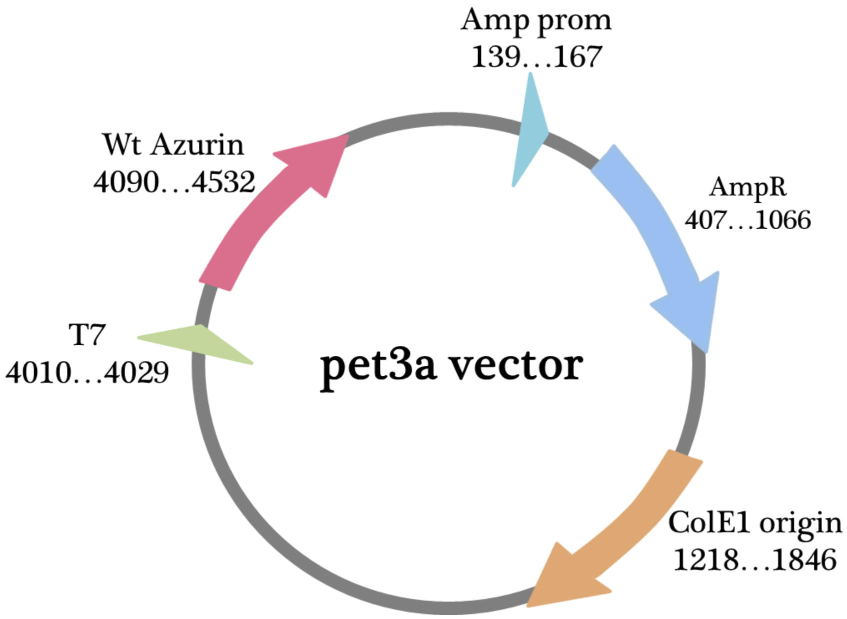

Figure 3.2. pet3a vector: including T7 promoter (starts transcription), Wt Azurin (gene inserted), Ampicillin promoter (is a region of DNA that initiates transcription of a particular gene), Ampicillin (code for ampicillin), ColE1 origin (Origin of replication).

Then, for the mutants expression we transform the plasmid with the mutation to *E.coli* (BL_21). We start picking one colony of the transform cells and inoculate 6 ml of culture media as a starter culture (to indicate the bacterial grow). We allow it to grow at 37ºC until being slightly translucent (4-5 hours with vigorous shaking). We spin the cultures to removed β-lactamase, since degrade the antibiotic's structure (antibiotic is added to avoid non-desirable bacterial growth), and suspended the pellet in a fresh 6 ml culture media aliquot. We let it grow at 32ºC overnight (O/N) with vigorous shaking. The standard temperature for this step is 32ºC that gave us higher values of expression. Then the 6 ml were inoculated to a 500 ml LB medium and incubated at 37ºC until the optical density was close to 0.6. At that point IPTG (molecule used for the induction of the protein expression) was added to a final concentration of 1 mM. After 5h of induction the cells were harvested by centrifugation. Again we modify the following step to our benefit. The bacteria were frozen at -20ºC O/N for crack the cell membrane. After defrosting, the solution assumes a viscous consistency because DNA has been freed from the cracked cells. Sonication was used to break genomic DNA and restore a thin consistency instead of adding DNAse or RNAse (enzymes that catalysed the degradation of the DNA and the RNA). At this point the Azurin mutant (a periplasmic protein) will remain at the supernatant after centrifugation (the pellet was removed).

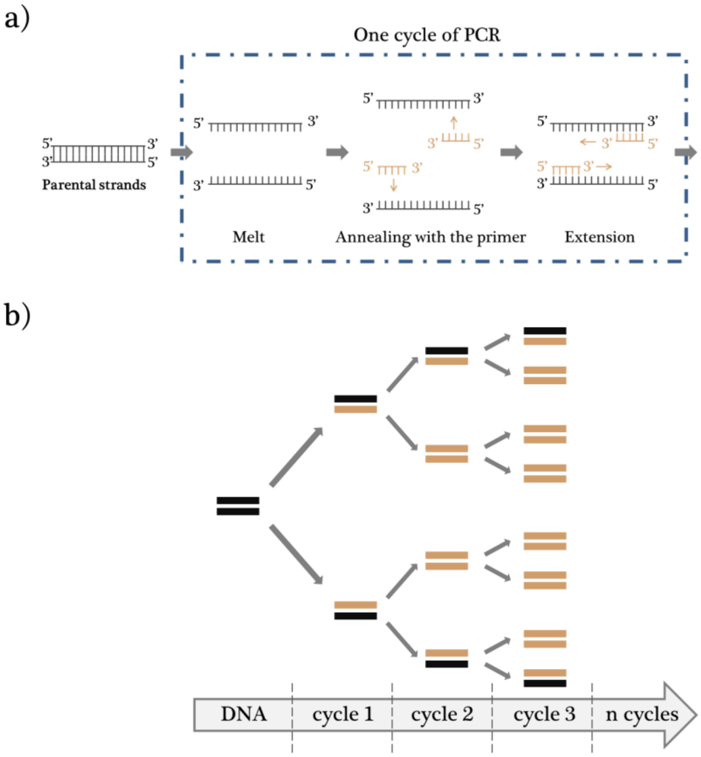
a)
One cycle of PCR
5'
3'
Parental strands
Melt
Annealing with the primer
Extension
After first cycle
b)
DNA
cycle 1
cycle 2
cycle 3
n cycles

Figure 3.3. PCR (Polymerase Chain Reaction) scheme: 3 steps → melt, anneal and elongation

To start with the purification, other proteins present in the same medium are precipitated by simply adding an acidic solution of 500 mM ammonium acetate (pH 4.5), where our protein is soluble (we followed Azurin protein with SDS-Polyacrylamide gel electrophoresis SDS-PAGE). To the final purification step, we use an ionic exchange column. This step requires adjusting the ionic strength to 25 mM ammonium acetate pH 4.5. For the first mutant we used a Hiload 26/10 SP Sepharose column, while for the rest we used HiTrap SP XL. We used a gradient of pH 4.5 - 9 in 25 mM ammonium acetate buffer. At this point, the mutant is completely pure (figure 3.4).

Because Azurin mutants can contain other metal ions like zinc (coming from the bacteria or the media) we convert all the holo-Azurin (Azurin with the metal ion coordinated) into Apo-protein (without the metal ion) through dialysis into a solution containing potassium cyanide (KCN, which coordinate the metal ions from the protein). Then we add 10 mM Cu^{+}/Cu^{2+} solution to the Apo-azurin to yield the holo. Note that between cyanide solution and copper solution we dialysed in front of ammonium acetate several times to fully remove all Zn $(Cu)_2$ complex.

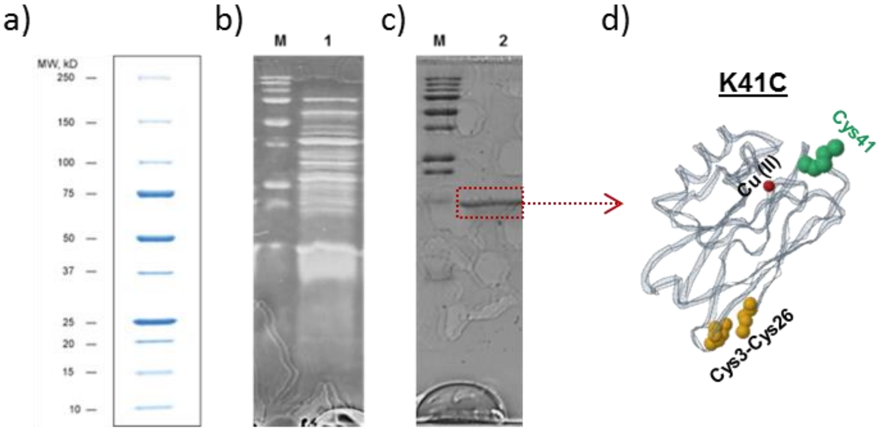

Figure 3.4. SDS-PAGE. a) Molecular mass standard employed in Lanes M in both b) and c). b) Lane 1 corresponds to the solution before purification through a HiLoad 26/10 SP Sepharose column. Multiple proteins are present in the solution. c) Lane 2 corresponds to the fraction obtained from the HiLoad 26/10 SP Sepharose column containing the purified K41C. Only a band at 14 KD is seen in that fraction, which corresponds to the K41C protein. d) K41C mutant structures. New amino acid Cys41 coloured in green, and disulphide bond Cys3-Cys26 coloured in orange.

3.2. Mutant 41: second metal coordination sphere

To select the proper amino acid to be exchanged we have to be aware of the aim of the bioengineering in this work: do a single-protein wire (figure 3.5b). This implies two gold electrodes (EC-STM tip and substrate electrode), where the Azurin will be anchored.

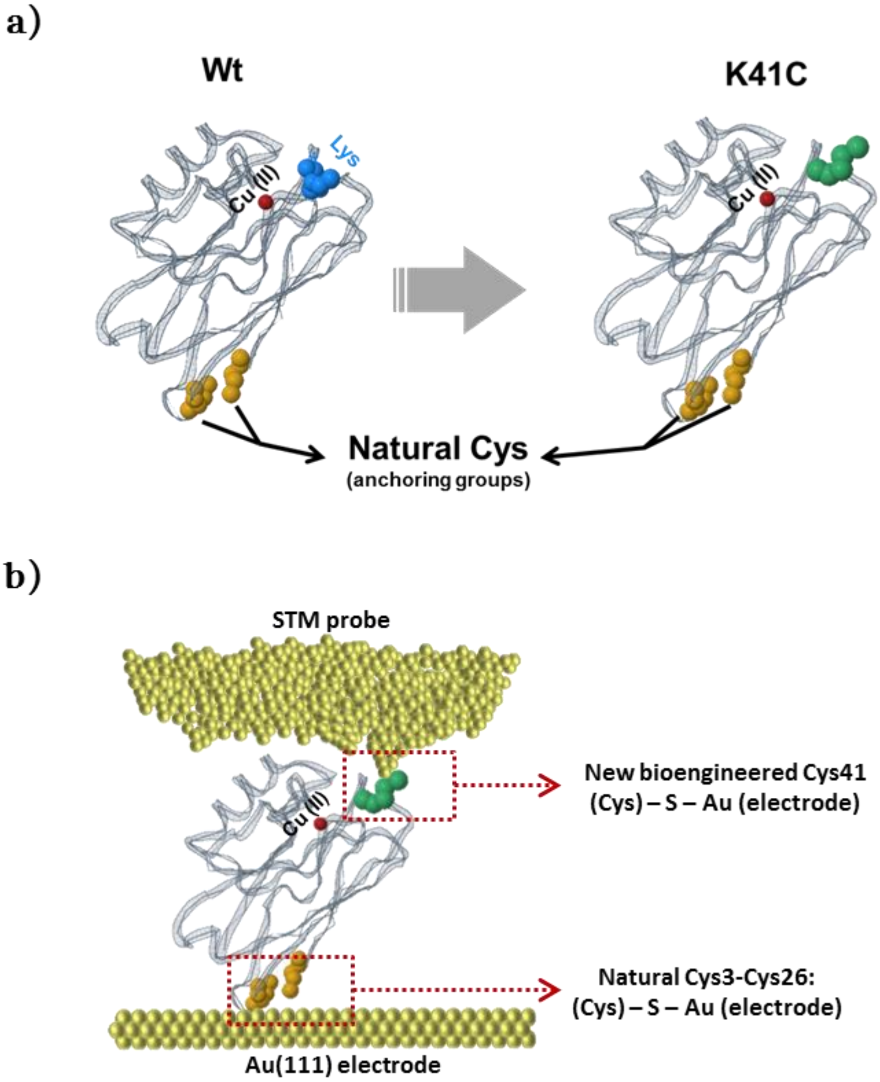
a)
Wt
K41C
Lys
Cu (II)
Cu (II)
Natural Cys
(anchoring groups)
b)
STM probe
Cu (II)
New bioengineered Cys41
(Cys) – S – Au (electrode)
Natural Cys3-Cys26:
(Cys) – S – Au (electrode)
Au(111) electrode

Figure 3.5. a) Structural models of the studied Wt Azurin (left structure extracted from the Protein Data Bank (PDB)[36]) and the modification introduced in the K41C variant (right structure). Natural Cys are coloured in orange. The wild-type amino acid Lys41 (blue) was substituted by a Cys41 (green) through point-site mutation. b) Schema of the single-protein wire using as electrodes the STM probe and the Au(111) substrate.

We first chose Lys41 to be exchange for a cysteine (figure 3.5a) for several reasons. The Wt Azurin has been aligned previously with several peptide binding materials, which show that there are two main priority regions: i) the disulphide bond (Cys3-Cys26) region due to the –SH reactivity, and ii) the comprised amino acids between His35 and Trp48. This second region is opposed to the Cys3-Cys26 disulphide bond, and it is known to be the hydrophobic pocket where the copper is buried[1]. Especially Lys41 stands out as the priority amino acid for the interaction, due to its side charge group that it is thought to be involved in redox-partner coupling for ET[20]. We will use these two points to anchor the protein at the junction and study the electron transport (ETp) through the disulphide bond Cys3-Cys26 and the new Cys41. Figure 3.5a show the 3D view of the Azurin natural cysteines (in orange) and in the opposite site is placed the Lys41 residue (left image) and the representation of the exchange with a cysteine (right image). Cys41 will be the anchoring point to the STM probe while the Cys3 and Cys26 will anchor the gold substrate (the –SH solvent-exposed thiol group from the Cys residue is the chemical connection in both sites).

3.2.1. Mutagenesis, Expression and Production

Here, three bases had to be modified to exchange a lysine for a cysteine, so the primers (table 3.2) were as long as it was possible having a high GC% (>50%). These measurements had been taken in order to create a high affinity interaction between the primers and the gene despite the three mismatches introduced to modify the residue 41. After the PCR and before the transformation of the bacterial cells (introducing the plasmid with the mutated gene inside the E.coli cells), the plasmid was sent to be sequenced. Once the sequence verifies that the mutation has been successful we proceed to the expression of the mutant. Table 3.3 shows the final 128 amino acid chain for Wt and the newly synthesized K41C (K41C corresponds to the same Wt sequence with a cysteine -C- instead of a lysine –K- in the 41 position) obtained from the sequencing.

Table 3.1. Amino acid sequence of the Wt Azurin gene.

Gene	Amino Acid sequence
Wt Azurin	MLRKLAAVSLLSLLSAPLLAAECSVDIQGNDQMQFNTNAIT VDKSCKQFTVNLSHPGNLPCNVMGHNWVLSTAADMQGVV TDGMASGLDKDYLKPDDSRVIAHTKLIGSGEKDSVTFDVSK LKEGEQYMFFCTFPGHSALMKGTLTLK

Table 3.2. Sequence of the forward and backward primers for the K41C mutant production. The highlighted bases in bold and underlined correspond to the ones designed to exchange the Lys41 residue by a Cyst residue of the Wt.

Primer	Amino Acid sequence
K41C_Reverse	5'-GTTGTGACCCATAACGTT**GCA**CGGCAGGTTACCTGGG
K41C_Forward	5'-CCCAGGTAACCTGCCG**TGC**AACGTTATGGGTCACAAC

Table 3.3. Sequence of the Wt Azurin and mutant K41C proteins. Amino acid 41 is highlighted in bold and underlined in both Wt and mutant sequences.

Description	Amino acid sequence
Wt Azurin	AECSVDIQGNDQMQFNTNAITVDKSCKQFTVNLSHPGNLP**K**NVMGHNWVLSTAADMQGVVTDGMASGLDKDYLKPDDSRVIAHTKLIGSGEKDSVTFDVSKLKEGEQYMFFCTFPGHSALMKGTLTLK
K41C Azurin	AECSVDIQGNDQMQFNTNAITVDKSCKQFTVNLSHPGNLP**C**NVMGHNWVLSTAADMQGVVTDGMASGLDKDYLKPDDSRVIAHTKLIGSGEKDSVTFDVSKLKEGEQYMFFCTFPGHSALMKGTLTLK

After the expression and the purification, we got a pure aliquot of K41C mutant which will be concentrated upon different necessities of the techniques required. The solution is stored at -20ºC in order to preserve the mutant.

3.2.2. Characterization

Once we have produced the K41C mutant, we proceed through the characterization process to study and discern any change occurred in the mutant versus the Wt. Despite the lack of crystalline structural information of the K41C mutant, we will show results from different characterization techniques (see chapter 2) to support evidences of both the preservation of its tertiary folding structure and its ET activity.

3.2.2.1. Structural characterization: Spectroscopic methods.

For structural characterization, we have used two different techniques: i) UV-visible spectroscopy to analyse the typical blue absorption band of the copper proteins and ii) fluorescence spectroscopy that relates the effect of the quenched fluorescence of the buried tryptophan reside to the protein folding state. To support these results we have run molecular dynamics for both Wt and K41C in collaboration with Juan Carlos Cuevas' group (further theoretical details will be explained in the next chapter 4).

UV-visible spectroscopy

Blue copper proteins are characteristic by a strong Ligand-to-metal charge transition (LMCT) absorption band around 600 nm. For *Pseudomonas aeruginosa* Azurin, this is ascribed to the $p_{\pi(Cys)}$-to-Cu^{II} charge transfer band. When the interaction of this coordinated ligand to the copper is modified the absorption band shifts (see chapter 2 for more information and examples). This coordination ligand field could be modified by axial interaction variations (Cu-Met121 for example could be strengthened or weakened). Because of that the exact position of these bands has been extensively used to extract details on the copper ligand-field structure in blue copper proteins upon specific mutations of their sequence[10,13,21]

In our work the K41C UV-vis absorption spectra was obtained at room temperature using an Infinite M200 PRO Multimode Microplate Reader from Tecan. Protein samples were approximately of 7 μM in 50 mM ammonium acetate buffer pH 4.5. Figure 3.6a shows the UV-visible absorption spectra for the Wt Azurin and its K41C variant, both displaying strong LMCT absorption bands within the range of the typical blue site of Cu proteins; 634 and 615 nm respectively for Wt and K41C. The observed slight blue shift for the K41C suggests a small perturbation of the Cu binding site upon mutation[10,16,22–24] usually ascribed to a decrease in the ligand-field energy as a result of the axial coordination weakening of the Methionine (Met) 121 residue binding the Cu metal center[10,18,24].

As control UV-visible experiments, we thermally denaturize (unfold) both proteins structures and observed the complete disappearance of the Cu^{II} absorption peak (figure 3.6a). The thermal denaturation for the Wt was performed at 90ºC above the well-known 84.4ºC value for the irreversible unfolding of the Wt[25]. This experiment constitutes the irreversible break for both tertiary and secondary conformations. On the other hand, we have used the same electronic transition to study the unknown thermal stability of the K41C. For this reason, we have studied the UV-vis of the K41C variant in a wide range of temperatures (figure 3.6b). We determine that the folding structure for the K41C variant is stable for temperatures below 70ºC above which it experiences an irreversible unfolding.

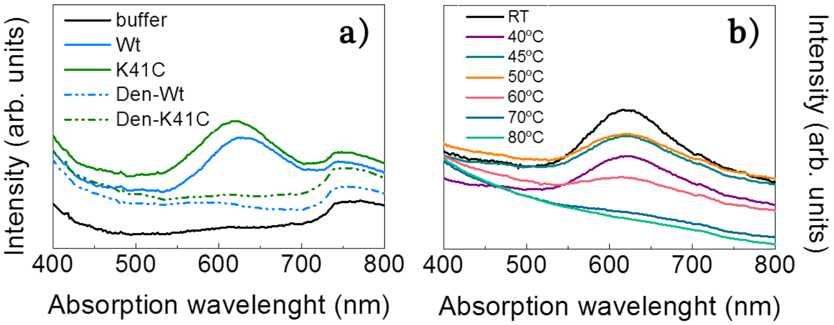

Figure 3.6. a) Absorption spectra of Wt Azurin (blue line), K41C (green line), denatured-Wt (blue dotted line) and denatured-K41C (green dotted line). Maximum peak absorptions appear at 634 nm and 615 nm for Wt and K41C, respectively. **b)** Absorption spectra of K41C mutant after heating the sample for 10 minutes at increasing temperatures from room temperature (RT) to 80 ºC (see legend).

Summing up, we can see through UV-vis measurements that the copper coordination centre has experienced a minimal change upon the K41C mutation, as well as it preserved a high thermal stability.

Fluorescence spectroscopy

Proteins and peptides with aromatic amino acids are intrinsically fluorescent when excited with UV light. The three amino acid residues that are primarily responsible for the inherent fluorescence of proteins are tryptophan, tyrosine and phenylalanine. The fluorescent properties of tryptophan are solvent dependent. As the polarity of the solvent decreases, the spectrum shifts to shorter wavelengths and increases in intensity. For this reason, tryptophan residues buried in hydrophobic domains of folded proteins exhibit a spectral shift about 10 to 20 nm upon any structural 'opening' (partial unfolding that expose the trp to the solvent). This phenomenon has been utilized to study protein denaturation[26].

In the case of Azurin, only one aromatic residue -Tryptophan (Trp) 48- buried in the core of the tertiary structure. Fluorescence spectra were recorded using a Horiba spectrofluorometer. Trp48 fluorescence band is monitored after exciting at 290 nm. The fluorescence peak for the Wt Azurin is centred on 308 nm. This band is characteristic for a completely buried Trp48 when the protein folding structure is preserved and it does not interact with the outer solvent[27].

Both Wt and K41C variants were measured as well as their denaturized homologous (figure 3.7.). Both proteins present fluorescent maxima centred at 315 nm before denaturation, which indicates that both proteins preserve the 3D folding structure and the trp48 keeps buried. After thermal denaturation of the samples (90ºC during 20 minutes), the fluorescent peak shifts to ~360 nm, which indicates that Trp48 has been exposed to the solvent, evidencing their unfolded state for both proteins. The exact values are shown in figure 3.7.

So these results assess that the 3D folding structure is preserved in the K41C variant with minimal or non-modifications *vs.* the Wt Azurin.

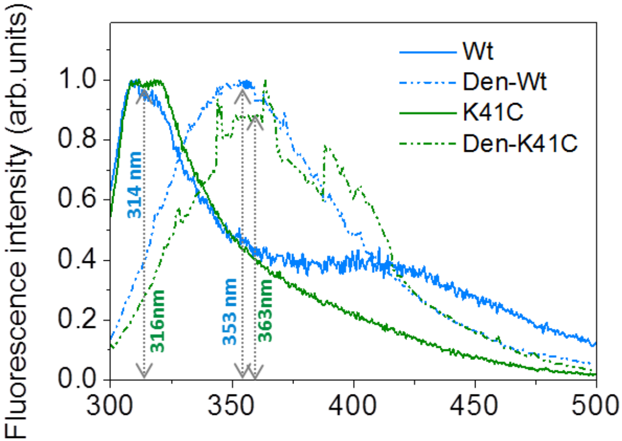

Figure 3.7. Florescence spectra of Wt Azurin and K41C mutant with the respectively denatured homologous (Den-Wt and Den-K41C). Samples were selectively excited at 290nm.

3.2.2.2. Electrochemical characterization

Cyclic voltammetry (CV)

Once we have structural proof of the 3D conformation of both proteins, namely Wt and K41C variant, we test their electrical activity by electrochemical measurements. The selection of the working electrode (a functionalized hexanethiol Au(111) surface - $CH_3(CH_2)_5S$-Au(111)-) was selected because the Azurin protein has a hydrophobic patch nearby the copper centre that allows direct van der Waals interactions with the methyl end of the alkanethiols forcing the copper centre to be closer to the electrode surface (figure 3.8a). It has been proven that Azurin proteins in this configuration allows an efficient electron exchange between the Cu centre and the Au surface[3]. In addition to the Wt and K41C voltammetry, electrochemical analysis of denaturized proteins was also done to prove that unfolded protein lacks redox activity (figure 3.8c,d).

Cyclic voltammograms were undertaken using an Autolab PGSTAT-12 Galvanostat-Potentiostat equipped with a three electrode electrochemical cell composed by a platinum wire as a counter electrode, a miniaturized ultralow leakage membrane Ag/AgCl (SSC) as a reference electrode, and $CH_3(CH_2)_5S$-Au(111) as a working electrode. All the electrolytes solutions were deoxygenated with purified argon. Cyclic voltammograms were done at a scan rate of 50 mV·s^{-1}. The experiments were performed in 50 mM ammonium acetate buffer pH 4.55.

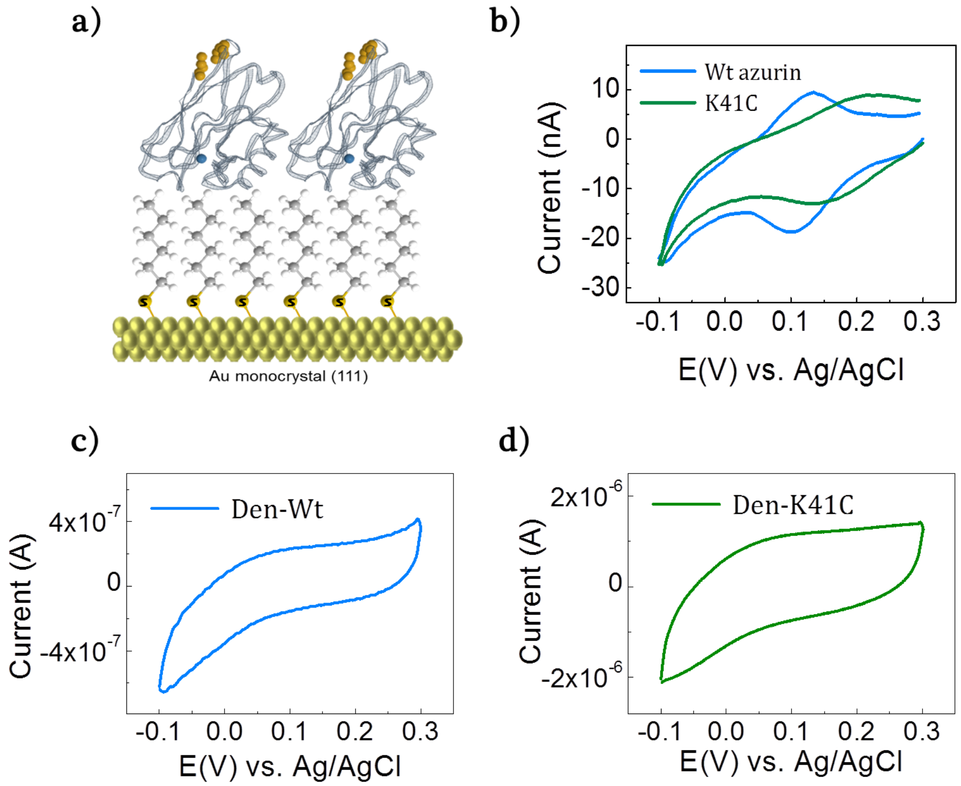

Figure 3.8. **a)** Schematic representation of the protein adsorption on the hexanethiol-functionalized Au (111) electrode. **b)** Electrochemical cyclic voltammetry response of the two protein variants adsorb on an Au(111) substrate in 50 mM ammonium acetate buffer (pH 4.55) as the electrolyte. The electrochemical potential scan rate was set to 50 mV/s. **c)** and **d)** cyclic voltammograms of denaturized-Wt Azurin (Den-Wt, blue line) and denaturized-K41C (Den-K41C, green line) respectively on the hexanethiol-functionalized Au(111) electrode in 50 mM ammonium acetate buffer, pH 4.55. Scan rate 50 mV·s^{-1}.

The slight different "energetic" chemical surrounding for the Cu centre in the Wt and the K41C mutant already shows an impact on the protein redox properties. A decrease in the ligand-field energy typically worsens the stability of the Cu(II) oxidation form because the –S coordination bond of the Met elongates, thus destabilizing the oxidized Cu form and raising the observed midpoint redox potential[15,16,18]. Figure 3.8b shows the cyclic voltammograms of both Wt and K41C variants of the Cu-Azurin adsorbed on the functionalized Au (111) surface (the extracted redox midpoints from the CVs for Wt and K41C are 120 mV and 172 mV respectively). In agreement with the UV-vis measurements, the measured mid-redox potential displays an anodic shift of ~50 mV for the K41C mutant with respect to the Wt, which points to a reduction of the electron density around the Cu centre with the corresponding destabilization of the Cu(II) oxidation state. Moreover, the larger cathodic (E_{red})-to-anodic (E_{ox}) peaks separation (E_{ox}-E_{red} of 0.038 V and 0.096 V for the Wt and K41C respectively) evidences a reversibility loss in the K41C mutant versus the Wt[28] owing to the stabilization of one of the Cu oxidation states and implying a markedly slower electron transfer rate for the electron exchange.

Summing up, the K41C mutant displays similar folding characteristics when compared to the Wt and small structural variations of the first coordination sphere of the Cu centre. Unexpectedly, the K41C shows significant changes in its redox properties as seen by a 50 mV anodic shift and a slower electrochemical kinetics, which evidences the high sensitivity of the ET to wild structural changes in redox proteins.

3.2.3. Metal/protein conjugation assays

The aim of the K41C mutation is to build a stable single-protein wire through the Cys41 in addition to the natural Cys3-Cys26 disulphide bond (figure 3.5b). In order to confirm the bridging efficiency of the extra thiol anchoring point in the K41C variant versus the Wt, three different systems were studied by TEM: i) free-protein Au Nanoparticles (NP); ii) Au NP-Wt (10:1 molar); iii) Au NP-K41C (10:1 molar). The solutions were prepared by having a low NP concentration of $2.8 \cdot 10^{+13}$ NP/ml suspended in the working buffer with and without the proteins for a period of 2 hours. Then it was deposited in a gold grid, and dried at air conditions (standard sample preparation). Figure 3..9b and c show both EDS spectrums of NP-Wt and NP-K41C samples. They were taken on a small region covering few NPs. It is clearly seen that a peak for Cu appears, which indicates the presence of protein (the only source of Cu). The gold peak corresponds to the NPs as well as the TEM grid.

Both proteins covalently are expected to bind to Au NP through the two natural Cysteine residues (*Cys*3 and *Cys*26)[29] as previously observed[30]. Wide TEM images were taken (N~10) for each system and the percentage of Au NPs dispersion/aggregates was calculated through an imaging analysis software (DigitalMicrograph software). As shown in Figure 3.9a and Table 3.4, and the presence of both proteins favour in general the NP interconnection. The percentage of NP dimers formation is significantly larger in the case of the K41C, ~20%, than in the Wt case, ~13%. The K41C is however the only one capable of forming large NP networks (number of NP > 5) at the very low employed concentrations. These observations support the fact that the K41C variant presents enhanced capability to bridge two NP through their two axial thiol (-SH) groups, namely, the two natural *Cys*3 and 26 and the bioengineered *Cys*41. These results will also foresee superior stabilities of the single-protein wires for the K41C (see chapter 5).

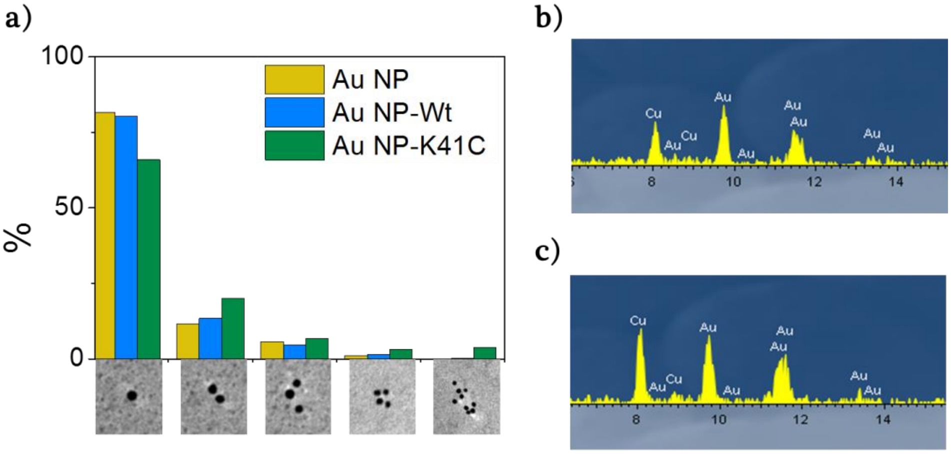

Figure 3.9. Transmission electron microscopy (TEM). The percentages (%) of Au NPs dispersion/aggregates (single NP, two NP, three NP, four NP, >five NP) were calculated for the three studied samples: free-protein Au NP (yellow), Au NP incubated with Wt protein (blue) and Au NP incubated with K41C variant (green). **b,** EDS spectrum of Au NP-Wt (10:1) and **c,** EDS spectrum of Au NP-K41C (10:1), both performed on a gold grid.

Table 3.4. Percentages (%) of Au NPs aggregates (single NP, two NP, three NP, four NP, >five NP network).

	1 NP	2 NP	3 NP	4 NP	≥5 NP
Au NP	81.5 %	11.6 %	5.8 %	1.1 %	0 %
Au NP-Wt	80.3 %	13.5 %	4.5 %	1.5 %	0.2 %
Au NP-K41C	66 %	20.1 %	6.8 %	3.2 %	3.9 %

3.3. Rationalizing Electron transfer (ET) through a redox/protein: other mutants

The K41C mutation shows that we have the ability to allocate anchoring groups in the form of Cys residues. We propose next a variety of point mutations on the outer part of the Azurin for anchoring purposes. Such mutants will be exploited in chapter 5 to control the orientation of the individual redox protein trapped in the tunnelling junction. We are focusing only on the most proper binding site for the EC-STM probe. We list all the amino acids available in the outer sphere of the protein (figure 3.10), which are exposed to the electrolyte because it is essential to build the single-protein wire. Being exposed to the solvent is not enough to be bioengineered; also the residue has to be accessible for EC-STM probe interaction. To elucidate how Azurin is laying onto the gold electrode, some calculations were done by Juan Carlos Cuevas' group (see chapter 4 for more detailed information). From that information we first removed the residues in close proximity to the sample electrode or those ones that are not accessible to wire the protein due to anchoring position achieved by the protein. As we want to preserve the tertiary structure, all amino acids forming hydrogen bonds, whose contribution asserts to the 3D structure, are rejected. The last step was to evaluate several groups of amino acids that are sequential in the protein peptidic chain. In order to control the protein/electrode coupling, we select residues for anchoring purposes at different distances from the active redox copper centre at the first coordination sphere of the copper. At that point, the list has strongly decreased to mainly 8 priority amino acids: Glutamine (Glu, Q) 12, Valine (Val, V) 43, Alanine (Ala, A) 65, Leucine (Leu, L) 68, Aspartic acid (Asp, D) 76, Serine (Ser, S) 89, Proline (Pro, P) 115 and Leu120 (figure 3.10).

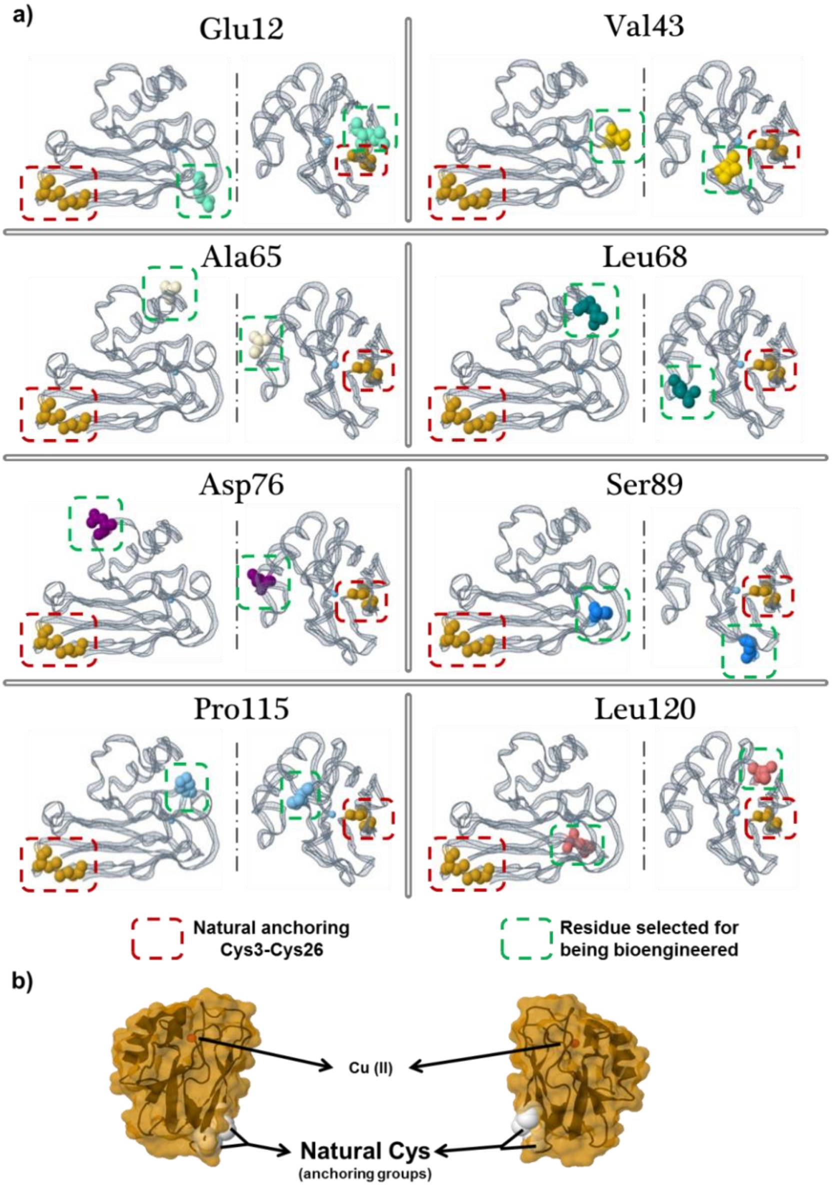
a)
Glu12
Val43
Ala65
Leu68
Asp76
Ser89
Pro115
Leu120
Natural anchoring Cys3-Cys26
Residue selected for being bioengineered
b)
Cu (II)
Natural Cys
(anchoring groups)

Figure 3.10. a) Structural models of the studied wild-type Azurin (structure extracted from the Protein Data Bank (PDB)[31]). Natural cysteines (*Cys*3 and *Cys*26) are coloured in orange. The different amino acids selected to be replaced for a Cys are coloured: Glutamine (Glu, light green) 12, Valine (Val, yellow) 43, Alanine (Ala, white) 65, Leucine (Leu, dark green) 68, Aspartic acid (Asp, purple) 76, Serine (Ser, blue) 89, Proline (Pro, light blue) 115 and Leu (pink) 120. **b)** Surface in orange representing the solvent exposed area of the Azurin.

3.3.1. Mutagenesis, Expression and Production

The procedure of mutagenesis for these new mutants is the same described in ‘3.1 Standard protocol Section’. Table 3.5 shows the new primers designed for every new residue to be exchange by a Cys, whose length always was regulated by the GC% and the T_m. No difficulties occurred in this process neither for the mutagenesis, the expression or the purification.

Table 3.5. Sequence of the forward and reverse primers for the point mutations of Q12C, V43C, A65C, L68C, D76C, S89C, P115C and L120C. The bases in bold correspond to the ones designed to exchange the desired residue instead a cysteine.

Primer	Amino Acid Sequence
Q12C_Forward	5’-gctccgttgatatc**tgc**ggtaatgatcagatgcag
Q12C_Reverse	5’-ctgcatctgatcattacc**gca**gatatcaacggagc
V43C_ Forward	5’-ggtaacctgccgaagaac**tgc**atgggtcacaactggg
V43C_ Reverse	5’-cccagttgtgacccat**gca**gttcttcggcaggttacc
A65C_ Forward	5’-ggcgttgtcactgacggtatg**tgc**agcggtctgg
A65C_ Reverse	5’-ccagaccgct**gca**cataccgtcagtgacaacgcc
L68C_ Forward	5’-ggtatggctagcggt**tgc**gataaagactacctgaagcc
L68C_ Reverse	5’-ggcttcaggtagtctttatc**gca**accgctagccatacc
D76C_ Forward	5’-cctgaagccg**tgc**gactctcgagttatcgccc
D76C_ Reverse	5’-gggcgataactcgaga**gca**atccggcttcagg
S89C_ Forward	5’-gcccacaccaagctgatcgga**tgc**ggtgaaaaagactcc
S89C_ Reverse	5’-ggagtctttttcacc**gca**tccgatcagcttggtgtgggc
P115C_ Forward	5’-gttcttctgcactttc**tgc**ggtcactccgcactgatgaaggg
P115C_ Reverse	5’-cccttcatcagtgcggagtgacc**gca**gaaagtgcagaagaac
L120C_ Forward	5’-cccgggtcactccgca**tgc**atgaagggtaccc
L120C_ Reverse	5’-gggtacccttcat**gca**tgcggagtgacccggg

After the expression and the purification, we have of each eight mutants pure aliquots, one for each mutant, which will be concentrated upon the different necessities of the techniques required. The solutions were stored at -20ºC in order to preserve the mutants' structure.

3.3.2. Characterization

We proceed through the characterization process to study possible structural changes occurred after the residue exchange by means of spectroscopic and electrochemical characterization techniques (see chapter 2).

Figure 3.11a shows the structure of the Cys in the centre surrounded by the residues to be replaced. Structural variations and electrochemical differences are expected due to the fact that a polar uncharged residue (cysteine) is being to replace at some points a really different residue both in structure a properties. Glu12 is a polar uncharged residue as Cys, but Cys is more hydrophobic. Glu12 is not directly bound to any ligand, but is positioned onto the copper binding site. It is a key position close to the binding site of Azurin for ET with its redox partner. This modification is expected to not disturb the copper centre geometry. Val43 is a non-polar uncharged residue placed in the hydrophobic patch of the Azurin (see figure 3.1a). In contrast, Cys presents high polarity and less hydrophobic character, so it is expected to slightly modify the 3D structure. Ala65 and Leu68 residues are both in the α-helix so these modifications are going to partially disrupt the 3D α-helix structure, however the copper centre and the β-sheet should not be modified. The α-helix is involved in the isolation of the trp48 from the solvent, so a minimal disruption in the helix would affect the fluorescence spectra. In this case we exchange non-polar residues for a polar one. Also, Leu is highly hydrophobic, while Cys is not that much. Asp76 is nearby the α-helix in the 3D conformation. So it is also placed on top of the trp48. Asp is a polar residue and more hydrophilic than Cys. It will probably affect the fluorescence of the trp48, but not the copper centre since it is far away of that region. Ser89 is like Cys, polar and uncharged residue but less hydrophobic. Its location in the folded structure is in the same region as residue 41 and 43. We suppose minimal changes to the active site and no major 3D variations. Maybe the trp48 fluorescence will show some shift because it is in close proximity to the residues covering trp48. Pro115 and Leu120 are contiguous residues to copper coordinated ligands. We are looking for a copper active site modification, but preserving the overall 3D conformation. Both are non-polar residues in contrast to Cys, and Leu has more hydrophobic character than Cys.

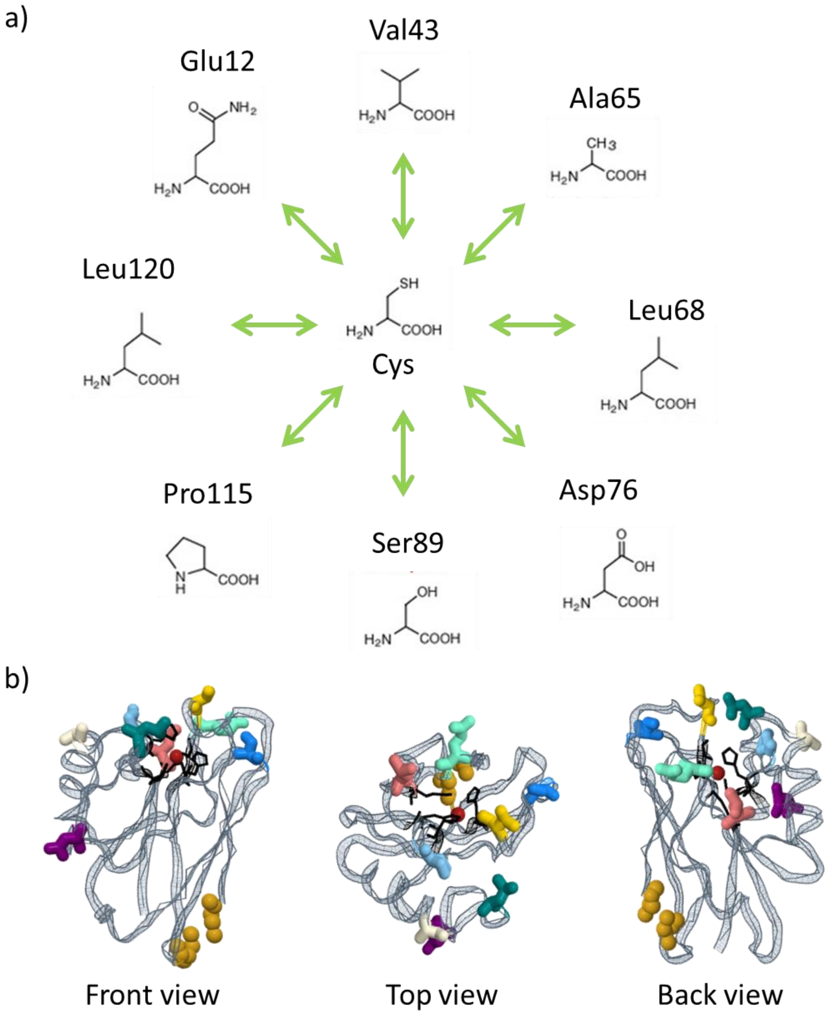

Figure 3.11. a) Scheme of the Amino acids exchanged in the Wt Azurin. In the centre is placed Cys, which replaces in every mutant one of the surrounding residues. **b)** Structural models of the studied wild-type Azurin (structure extracted from the Protein Data Bank (PDB)[31]). Natural cysteines (*Cys*3 and *Cys*26) are coloured in orange. The different amino acids selected to be replaced for a Cys are coloured: Glutamine (Glu, light green) 12, Valine (Val, yellow) 43, Alanine (Ala, white) 65, Leucine (Leu, dark green) 68, Aspartic acid (Asp, purple) 76, Serine (Ser, blue) 89, Proline (Pro, light blue) 115 and Leu (pink) 120. Cu is in red and the ligands (Gly45, His46, Cys112, His117, Met121) in black.

3.3.2.1. Structural characterization: Spectroscopic methods.

We use again two different techniques: UV-visible spectroscopy taking advantage of the typical blue absorption band of the copper proteins, and fluorescence spectroscopy related to the effect of quenched fluorescence of the buried try48 residue.

UV-visible spectroscopy

The LMCT absorption bands in the new set of mutants show a variety of effects in the Cu ligand field depending upon the position of the mutation.

Six of eight mutants Q12C, V43C, A65C, D76C, S89C, and L120C present similar absorption bands as K41C mutant. All present small blue shifts of the absorption peak between 11 to 25 nm. We have ascribed this effect to a small perturbation in the copper binding site, more specifically to a decrease in the ligand-field energy (figure 3.12)[10,14,16,18,23,24].

For the S89C and the L120C another band around 390 nm has appeared. This band correspond to p_σ(Cys)→Cu^{II} ligand to metal charge transfer. This band is the result of a weakened ligand Cu(II)→S(Cys) by a strengthened axial coordination. For L120C, the amino acid exchanged is adjacent to the axial copper coordinated his121. We supposed that the exchanged of the Leu (nonpolar residue, isobutyl as side group) for a cysteine (polar residue, SH side group) has produced a changed in the his121-Cu length which is reflected on to the Cu(II)→S(Cys) LMCT absorption band. Cys present less steric interaction than Leu, so maybe the his121 could penetrate more toward the copper centre. On the other hand S89C is relatively far away from any coordinated residue in the sequenced peptidic chain, however in the 3D conformation it is placed on top of the imidazole side chain from the strong coordinated his46. The elongation of the Cu(II)→S(Cys112) coordination bond results in a rotation of the d_{x2-y2}, so the ground state of the Cu(II) ion overlaps in a better way with the p_σ orbital of Cys112 corresponding to a charge transfer band at higher energy (~400 nm). This strengthened Cu-S(Met) interaction, which induce a weaker Cu-S(Cys) interaction, and tetragonal distortion has been referred to as the coupled distortion[10,13].

Finally, both P115C and L68C show a red shift, having the absorption band at ~700 nm. This weak absorption band is related to forbidden d-d transitions. So these two mutants are expected to have the most different electron transfer behaviours changes[13,21,24,32–34]. The P115C variant has modified a residue between two strongly coordinated ligands (cys121 and his117) which may affect the LCMT of the copper. Besides L68C disruption of the absorption bans seems to be related with a 3D modification in the folding structure, since it is far away from the copper centre to affect it directly.

Figure 3.12 show the absorption bands shifted for the eight mutants (exact values at table 3.6) as well as the absorption spectra for each denatured mutant where no absorption is observed.

Table 3.6. Values obtained from the maximum absorption band.

Q12C	634 nm
V43C	626 nm
A65C	626 nm
L68C	~700 nm
D76C	628 nm
S89C	384 nm / 640 nm
P115C	770 nm
L120C	385 nm / 637 nm

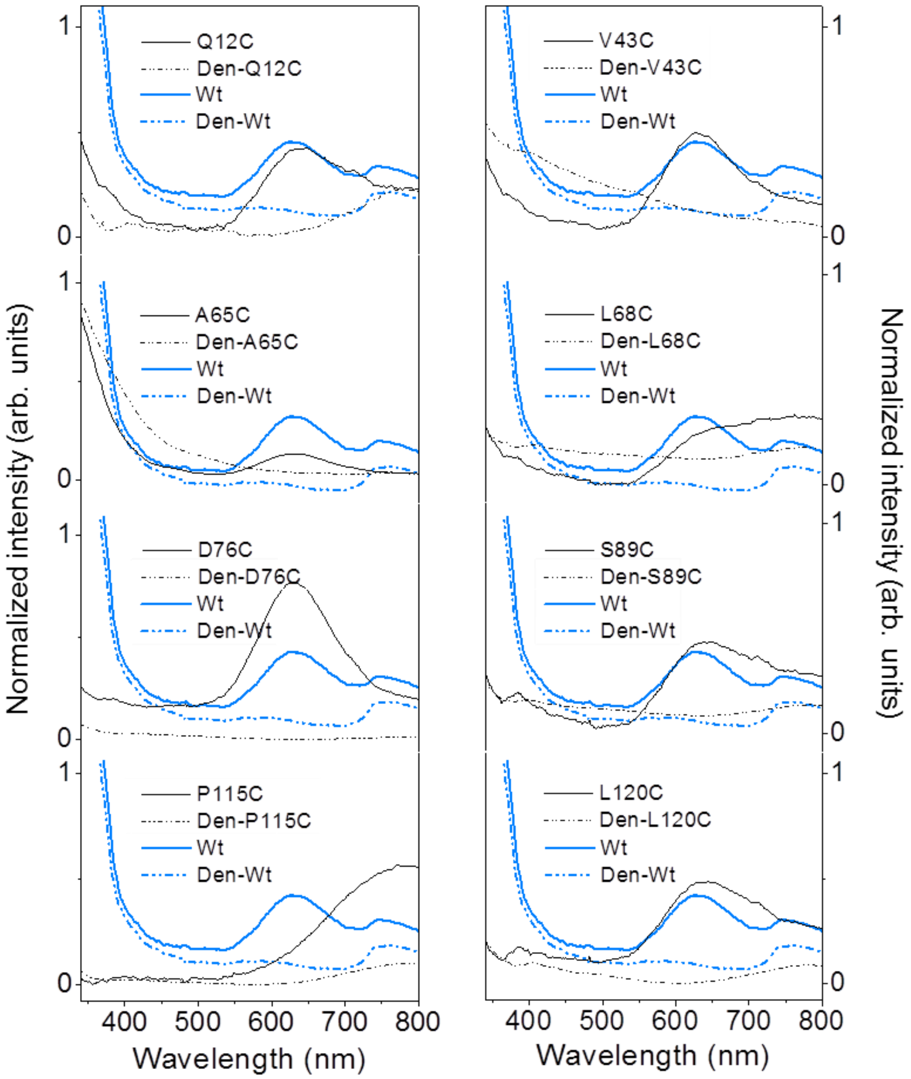

Figure 3.12. Absorption spectra of Q12C, V43C, A65C, L68C, D76C, S89C, P115C, L120C Azurin (solid lines) and the respectively denatured protein (dotted lines). See table 3.6 for maximum peak absorptions.

Fluorescence spectroscopy

For that set of new mutants, the results in fluorescence emission of Trp48 could be divided in two tendencies. The first group of mutations, which is formed by Val43C, Ala65C, Leu68C, Pro115C and Leu120C, shows similar behaviour as Wt Azurin: all of them have a Trp48 fluorescence emission peak typical of the Azurin folded state (see figure 3.13). However, the fluorescence emission peak for these thermally irreversible denaturized mutants has been shifted towards ~360 nm (same behaviour showed by the denaturized-Wt). When the protein starts to open their folded structure the solvent penetrates the inner core and quenched the trp48 fluorescence. So as the trp48 is being exposed to solvent its fluorescence is started to be quenched.

Val43C, Pro115C and Leu120C show the biggest fluorescence shifts between both states, while for Ala65C and Leu68C the difference is almost insignificant. This evidences that the mutation is in the helix which is partially covering the Trp48. So in the folded state the new amino acid may incorporate a minimal geometric modification facing a little bit the Trp48 towards the solvent, which produce a quenching effect.

On the other hand, Glu12C, Asp76C and Ser89C have no change in the fluorescence spectra between folded protein and the thermally denaturized protein, which means the 3D folding structure has been largely modified by the mutation (it is a sign of some 3D medication). As it is state by Manetto et al. (see chapter 2) some modifications in the outer sphere of the protein could be translated to minimal geometric rearrangements. In some cases they disrupt a closer part of the Trp48, as a result the fluorescence is no quenched any longer. Because the minimum disruption around the Trp48 that opens a window to the solvent will be translated in a quenched Trp48. These three Azurin variants have incorporate a 3D conformational change that involves a solvent exposed trp48[25,27,35,36].

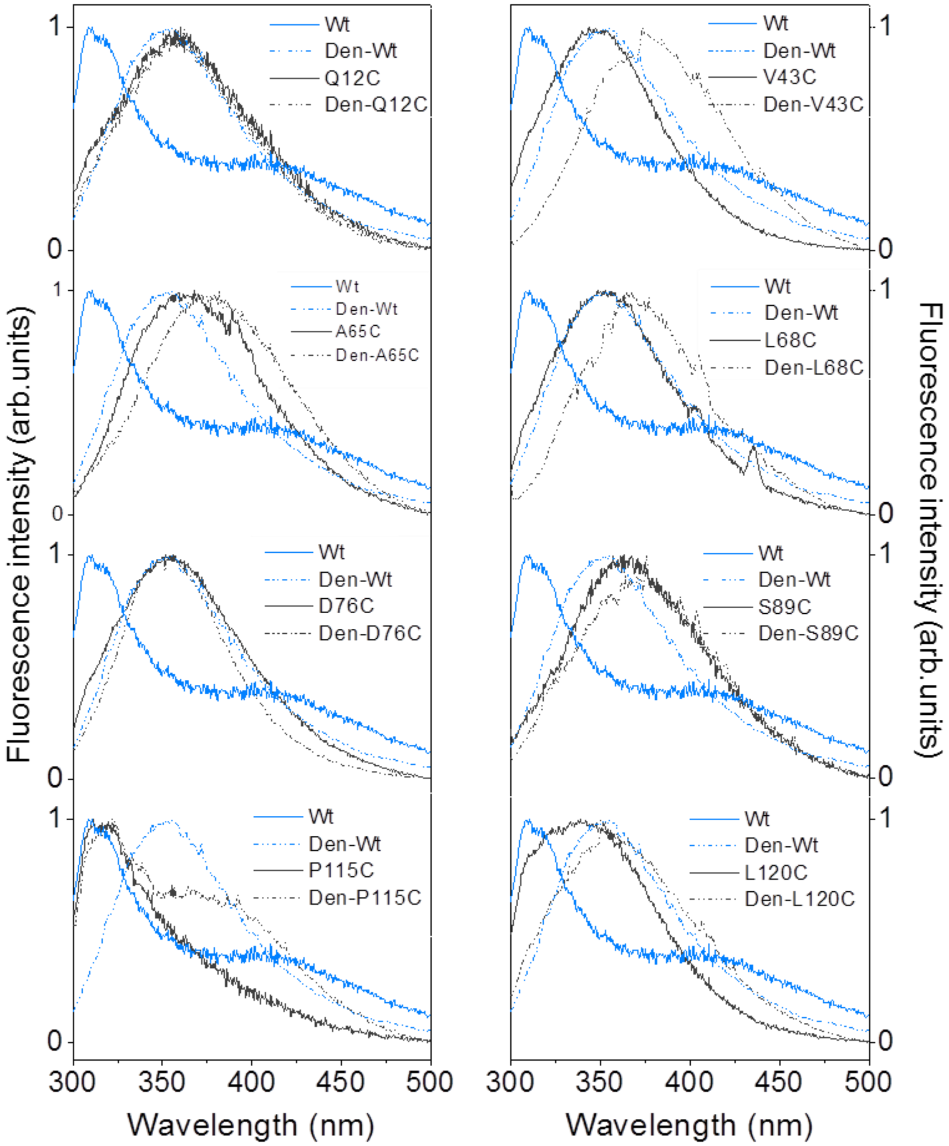

Figure 3.13. Florescence spectra of Wt, Q12C, V43C, A65C, L68C, D76C, S89C, P115C, and L120C with the respectively denatured homologous (Den-Wt, Den-Q12C, Den-V43C, Den-A65C, Den-L68C, Den-D76C, Den-S89C, Den-P115C, and Den-L120C). Samples were selectively excited at 290nm.

3.3.2.2. Electrochemical characterization

Cyclic voltammetry (CV).

For Q12C and A65C there is no electrochemical activity observed (figure 3.14). One explanation corresponds to a slight 3D structure modification which difficult or block the coupling protein-electrode, so the electron flow at the interface is no longer possible for that changed configuration. Residue 12 and 65 are placed close to the hydrophobic patch, which is the region that interacts with the hexanethiol SAM of the electrode for CVs (figure 3.11b). An extra argument for Q12C is related with the Trp48 exposed to the solvent (as seen in previously fluorescence characterization). It is possible that this residue could be involved in electron transfer process. So when it is exposed its ability to sink an electron is modified as well as the pathway of the electron propagation. This will be translated another time to a modification in the coupling between protein-electrode.

Another big modification observed was for P115C, which is placed between two copper ligands (his117 and cys112). In this case only the oxidation peak is observed with a displaced oxidation peak toward higher values. This mutant has shown big absorption band changed, related with a modification of the geometry of the active site. Since the copper ligand field is varied could be affect the charge transport mechanism or disrupted it. It seems that the protein is no longer reversible once it is oxidized. However, another possibility could be a bigger displacement of the redox peak toward negative values due to a huge increase on the reorganization energy. L68C as P115C has shown an effect on the first coordination as seen in the shift of the absorption bands.

The mutants that present a bigger effect on the reorganization energies are L68C and S89C, having 52 and 64 mV between peaks in contrast with the other values: 34 mV V43C, 39 mV D76C and 35 mV L120C. In the case of V43C and D76C is similar to Wt value, as well as the UV-vis values, which means that the active site has not suffered major modifications. That points to a change in the electron pathway through the protein peptide chain.

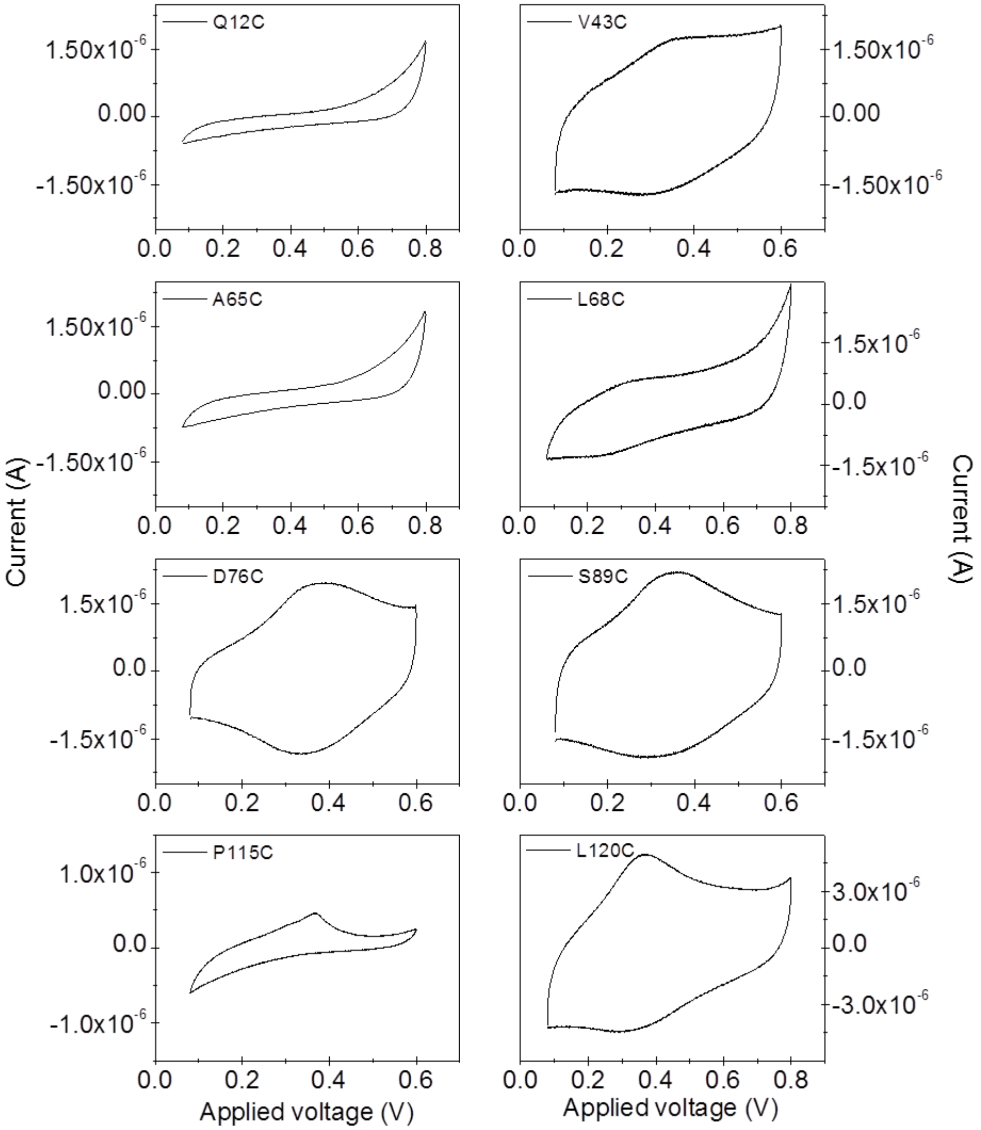

Figure 3.14. Electrochemical cyclic voltammetry response of five protein variants adsorb on an Au(111) substrate in 50 mM ammonium acetate buffer (pH 4.55) as the electrolyte. The electrochemical potential scan rate was set to 50 mV/s. See table 3.7 for redox potentials values.

Finally, V43C, L68C, D76C, S89C, and L120C, show big redox potential displacements. In literature is seen how point mutation increases the redox potentials to really higher values. But every mutation produce a variation as a result of different structural modifications to the first or second coordination sphere. It is possible that for D76C and S89C the partially exposed Trp48 plays a role, and also affect it by increasing the reorganization energies, which is appreciated in the higher separation peaks. For L68C, S89C and L120C the modification suffered by the active site seems to play a role in it. Off course each modification does not have the same effect on the redox potential. Besides it also depends on the hydrophobicity, the hydrogen interactions modification and the perturbations included in the electron density around the copper binding site. Residues 43, 68, 115 and 120 residues are also placed at the interface protein-electrode, in those cases the change in the electrochemical potential could be a contribution from the structural part as well as the interaction with the electrode. Cys is a polar residue and V43, Leu68, and L120 are hydrophobic ones, so the interaction is being weakened.

Table 3.7. Corresponding values of the redox mid-point of the voltammograms in figure 3.15.

Q12C	-
V43C	329 mV
A65C	-
L68C	278 mV
D76C	365 mV
S89C	304 mV
P115C	Only oxidation peak observed
L120C	347 mV

REFERENCES

1. Nar, H., Messerschmidt, A., Huber, R., van de Kamp, M. & Canters, G. W. Crystal structure analysis of oxidized Pseudomonas aeruginosa azurin at pH 5.5 and pH 9.0. A pH-induced conformational transition involves a peptide bond flip. *J. Mol. Biol.* **221,** 765–772 (1991).

2. Chin, Q. *et al.* Molecular monolayers and interfacial electron transfer of Pseudomonas aeruginosa azurin on Au(111). *J. Am. Chem. Soc.* **122,** 4047–4055 (2000).

3. Chi, Q., Zhang, J., Andersen, J. E. T. & Ulstrup, J. Ordered Assembly and Controlled Electron Transfer of the Blue Copper Protein Azurin at Gold (111) Single-Crystal Substrates. *J. Phys. Chem. B* **105,** 4669–4679 (2001).

4. Fristrup, P. *et al.* Voltammetry of native and recombinant Pseudomonas aeruginosa azurin on polycrystalline Au- and single-crystal Au(111)-surfaces modified by decanethiol monolayers. *J. Electroanal. Chem.* **511,** 128–133 (2001).

5. Chi, Q., Farver, O. & Ulstrup, J. Long-range protein electron transfer observed at the single-molecule level: In situ mapping of redox-gated tunneling resonance. *Proc. Natl. Acad. Sci. U. S. A.* **102,** 16203–16208 (2005).

6. Facci, P., Alliata, D. & Cannistraro, S. Potential-induced resonant tunneling through a redox metalloprotein investigated by electrochemical scanning probe microscopy. *Ultramicroscopy* **89,** 291–298 (2001).

7. Gray, H. B. & Winkler, J. R. Electron Transfer in Proteins. *Annu. Rev. Biochem.* **61,** 537–561 (1996).

8. Larosa, C., Milardi, D., Grasso, D., Guzzi, R. & Sportelli, L. Thermodynamics of the Thermal Unfolding of Azurin. *J. Phys. Chem.* **99,** 14864–14870 (1995).

9. Berry, S. M., Baker, M. H. & Reardon, N. J. Reduction potential variations in azurin through secondary coordination sphere phenylalanine incorporations. *J. Inorg. Biochem.* **104,** 1071–1078 (2010).

10. Clark, K. M. *et al.* Transforming a Blue Copper into a Red Copper Protein:\rEngineering Cysteine and Homocysteine into the Axial\rPosition of Azurin Using Site-Directed Mutagenesis and\rExpressed Protein Ligation. *J. Am. Chem. Soc.* **132,** 10093–10101 (2010).

11. Bernini, C. *et al.* Effects of the protein environment on the spectral properties of tryptophan radicals in *Pseudomonas aeruginosa* azurin. *J. Am. Chem. Soc.* **135,** 4822–4833 (2013).

12. Hay, M. T. *et al.* Spectroscopic Characterization of an Engineered Purple Cu A Center in Azurin. *Inorg. Chem.* **37,** 191–198 (1998).

13. Tian, S. *et al.* Reversible S-nitrosylation in an engineered azurin. *Nat. Chem.* **8,** 670–677 (2016).

14. Zanetti-Polzi, L. *et al.* A few key residues determine the high redox potential shift in azurin mutants. *Org. Biomol. Chem.* **13,** 11003–11013 (2015).

15. Garner, D. K. *et al.* Reduction potential tuning of the blue copper center in Pseudomonas aeruginosa azurin by the axial methionine as probed by unnatural amino acids. *J. Am. Chem. Soc.* **128,** 15608–15617 (2006).

16. Marshall, N. M. *et al.* Rationally tuning the reduction potential of a single cupredoxin beyond the natural range. *Nature* **462,** 113–6 (2009).

17. New, S. Y., Marshall, N. M., Hor, T. S. A., Xue, F. & Lu, Y. Redox tuning of two biological copper centers through non-covalent interactions: same trend but different magnitude. *Chem. Commun.* **48,** 4213–4217 (2012).

18. Warren, J. J., Lancaster, K. M., Richards, J. H. & Gray, H. B. Inner- and outer-sphere metal coordination in blue copper proteins. *J. Inorg. Biochem.* **115,** 119–126 (2012).

19. Manetto, G. D. *et al.* The role played by the helix in the unfolding pathway and stability of azurin: Switching between hierarchic and nonhierarchic folding. *ChemBioChem* **8,** 1941–1949 (2007).

20. Artés, J. M., Díez-Pérez, I. & Gorostiza, P. Transistor-like behavior of single metalloprotein junctions. *Nano Lett.* **12,** 2679–2684 (2012).

21. Abdelhamid, R. F. *et al.* π-π interaction between aromatic

ring and copper-coordinated His81 imidazole regulates the blue copper active-site structure. *J. Biol. Inorg. Chem.* **12,** 165–173 (2007).

22. Zanetti-Polzi, L. *et al.* A few key residues determine the high redox potential shift in azurin mutants. *Org. Biomol. Chem.* **13,** 11003–11013 (2015).

23. Springs, S. L., Bass, S. E. & McLendon, G. L. Cytochrome b562 variants: A library for examining redox potential evolution. *Biochemistry* **39,** 6075–6082 (2000).

24. Lancaster, K. M., George, S. D., Yokoyama, K., Richards, J. H. & Gray, H. B. Type-zero copper proteins. *Nat Chem* **1,** 711–715 (2009).

25. Guzzi, R., Rosa, C. La, Grasso, D., Milardi, D. & Sportelli, L. Experimental model for the thermal denaturation of azurin : a kinetic study. *Methods* **60,** (1996).

26. Lakowicz, J. R. *Principles of Fluorescence Spectroscopy Principles of Fluorescence Spectroscopy. Principles of fluorescence spectroscopy, Springer, New York, USA, 3rd edn, 2006.* (2006). doi:10.1007/978-0-387-46312-4

27. Huang, Q. & Quiñones, E. Assessment of the stability and unfolding pathways of azurin from Pseudomonas aeruginosa through the combination of denaturating osmolytes. *Arch. Biochem. Biophys.* **477,** 175–182 (2008).

28. Bard, A. J. & Faulkner, L. R. *Electrochemical methods : fundamentals and applications.* (Wiley, 2001).

29. Delfino, I. & Cannistraro, S. Optical investigation of the electron transfer protein azurin–gold nanoparticle system. *Biophys. Chem.* **139,** 1–7 (2009).

30. Gurunatha, K. L. *et al.* Nanoparticles Self-Assembly Driven by High Affinity Repeat Protein Pairing. *ACS Nano* **10,** 3176–3185 (2016).

31. Adman E.T., J. L. H. Structural Features of Azurin at 2.7 Angstroms Resolution. *Isr.J.Chem.* **21,** 8 (1981).

32. Basumallick, L. *et al.* Spectroscopic and density functional studies of the red copper site in nitrosocyanin: Role of the protein in determining active site geometric and electronic structure. *J. Am. Chem. Soc.* **127,** 3531–3544 (2005).

33. Hay, M., Richards, J. H. & Lu, Y. Construction and characterization of an azurin analog for the purple copper site in cytochrome c oxidase. *Proc. Natl. Acad. Sci. USA* **93,**

461–464 (1996).

34. Solomon, E. I. Electronic structures of active sites in copper proteins: Contributions to reactivity. *J. Inorg. Biochem.* **51,** 450 (1993).

35. Fuentes, L., Oyola, J., Fernández, M. & Quiñones, E. Conformational changes in azurin from Pseudomona aeruginosa induced through chemical and physical protocols. *Biophys. J.* **87,** 1873–1880 (2004).

36. Held, P. Quantitation of Peptides and Amino Acids with a Synergy ™ HT using UV Fluorescence. *BioTek Appl. Note* 1–8 (2006).

4

COMPUTATIONAL METHODS

4. COMPUTATIONAL METHODS

This work described in this chapter is in collaboration with Professors Juan Carlos Cuevas and Ruben Pérez at the 'Universidad Autónoma de Madrid'. Since we have bioengineered a protein and we have no information about the mutants' crystal structure we need to access as much computational information as possible on their folding structure under the working conditions. Also the data extracted from the previous spectroscopic techniques do not show a clear result about the 3D conformation. So that, in this collaboration several calculations were run to study the K41C mutant tertiary structure modifications. Computational methods also bring the opportunity to look at the stability of proteins when they are interfaced with an electrode. This fast assessment is important in order to reinforce the reliability of the method as well as the most likely protein to surface orientation

4.1. Visualization of the frontier orbitals and calculation of their energies for the studied protein fragment

We have performed *ab initio* computational calculations in the structurally relevant proteins segment for charge transport. We have used DFT computational methods using the long-range corrected B3LYP functional (CAM-B3LYP) to visualize the distribution of the frontier orbitals nearby the redox active Cu(II) metal centre, for the Wt Azurin and the K41C variants. Due to the intrinsic computational limitations, we have considered only the sequence fraction involving the first coordination sphere of the Cu(II) centre and the segment of the second coordination including the mutated residue at the 41 position: Lys41 (or Cys41 for the K41C variant), Asn42, Val43, Met44, Gly45, His46, His117, Cys112, and Met121 (figure 4.1)[25,26]. Such protein fragment constitutes the ET pathway connecting the solvent-exposed hydrophobic patch of the protein, that will be more accessible to the STM tip electrode[27,6,28], and the active metal centre. The protein folding structure of the fragment used for the electronic structure calculations (figure 4.1) has been taken from the crystalline Wt structure[29] for both protein variants (figure 3.4). This is a good approximation given the minor disruption of the Cu coordination field after the outer-sphere mutation is performed, as deduced from our spectroscopic characterization. Fine structural analyses of the mutation effect will have to be considered for cases involving major structural changes in the mutant protein folding[30].

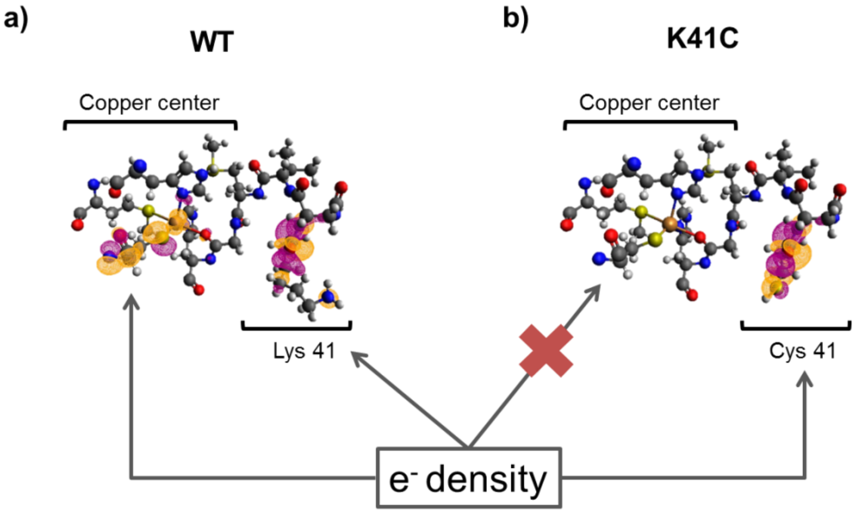

Figure 4.1. Electronic structure calculations. Isosurface plots (isovalue = 0.02) of the frontier molecular orbital (LUMO) involved in the electron transport of **a,** Wt and **b,** K41C fragments. Calculations were done at CAM-B3LYP/6311G+(d) level of DFT.

In our single-protein junction experiments, the electrons will be injected from the EC-STM probe electrode into the protein. Previous theoretical works relate the observed main electronic transitions in blue Cu proteins to the promotion of electrons to lowest unoccupied molecular orbitals (LUMO and LUMO+1)[26] bearing a high Cu character (~41%)[25]. Figure 4.1 shows the representation of the DFT-calculated LUMO frontier orbital for the ET-relevant fragment of the Wt Azurin showing significant LUMO-contribution at the metal centre and its first coordination sphere in the oxidized state of the protein. The orbital energy values resulting from the DFT calculation (figure 4.1) suggest a LUMO-transport for this system, assuming their uncertainty due to the poor DFT description of the electronic repulsion[31,32] and a low coupling between the protein/metal interface and the first Cu(II) coordination sphere[33]. Oppositely, figure 4.1 shows that the LUMO orbital in the K41C is mainly localized at the mutated *Cys*41 residue, with essentially no contribution at the Cu centre. The LUMO contribution at the metal site evidences the implication of the metal centre the observed charge transport through the Wt protein. While for K41C is seen a lack of the Cu centre participation in the LUMO transport channel, which is now located in less energetically accessible orbitals. The closest Cu(II)-contributing orbital appears now at the LUMO+2, further energetically separated, ~1.5 eV, from the LUMO frontier orbital.

The geometry of our studied Wt Azurin was obtained from the Protein Data Bank (PDB, http://www.rcsb.org/pdb/explore/explore.do?structureId=1AZU). In view of our spectroscopic results and molecular dynamics simulations (see next section 4.2), the K41C fragment structure was approached to be the same as the 1AZU by replacing the *Lys*41 for a *Cys*41. The calculated frontier orbitals for both fragments were obtained using *Density Functional* methods (DFT) using the software package *Gaussian 09*[1]. To predict correctly[2,3] the electron-transport pathways[4–6], a long-range-corrected variant *CAM-B3LYP* method was applied[7–11] using *6-311G+(d)* as basis set. All isosurface plots were obtained using *Avogadro* visualizing sofware[12]. Similar to QM/MM treatments, the *ab initio* calculations were conducted in the relevant fragment of the protein for the electron transport: Lys41 (or Cys41 for the K41C variant), Asn42, Val43, Met44, Gly45, His46, His117, Cys112, and Met121.

Protein fragment	**HOMO**	**LUMO**
Wt Azurin 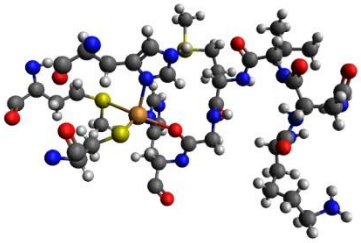	-7.26 eV	-6.64 eV
K41C mutant 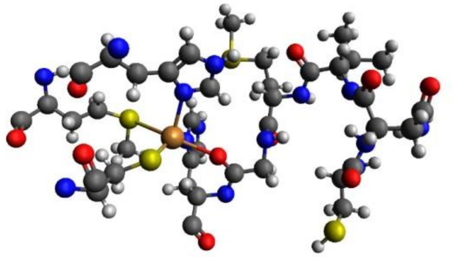	-7.46 eV	-6.01 eV

Figure 4.2. Molecular representations of the Wt (a) and K41C (b) and their calculated frontier orbitals energy at the CAM-B3LYP/6311G+(d) level of DFT.

4.2. Molecular Dynamics Simulations

Molecular Dynamics (MD) simulations has provide key information such as: quantitatively describe the structural changes on the WT-Azurin introduced by the K41C mutation; identify the possible adsorption conformations of the WT-Azurin over the Au (111) surface, and subsequently quantify the structural changes induced by such process; understand the influence of a gold STM tip on the structural stability of the Wt-Azurin as a function of the tip indentation height. For all the simulations, the protocol essentially consists on structural energy minimized, liquid medium, and with constant temperature.

4.2.1. MD simulations of Azurin in water: structural differences/similarities between Cu-Azurin, Wt and K41C mutant:

In this section we access the structure stability of three different Azurin structures: Wt Azurin, K41C mutant and Apo (without the copper) Azurin, which are freely floating in a water solution at a pH of 4.5. In figure 4.3, we show the initial configurations of the Wt (figure 4.3 a), K41C (figure 4.3 b) and Apo (Figure 4.3 c). In figure 4.3 d, the Cu-Azurin is represented with a Connoly surface where the residues are colored in agreement with their hydrophobicity index. In this figure, one can observe the protein hydrophobic patch (in dark blue), which is located near the cooper atom.

We have analyzed the dynamics of the Wt and the K41C structures during 500 ns of simulation, and the dynamics of the Apo structure during 300 ns. Looking at the time evolution of the total energy for the three Azurin structures in figure 4.4a, one realizes that in all cases a thermal equilibrium is reached before the 200ns of MD simulation. In Fig 4.5 we represent the final configurations of the three structures obtained at the end of the dynamics, showing that all the proteins preserve their initial structure. In particular, the mutation seems to have no effect on the overall structure of the protein. This can be quantified by looking at the evolution of the radius of gyration and the root-mean-square deviation (R_g and RMSD respectively, see Fig 4.4) that are practically identical for the Wt and for the K41C. The same happens to the secondary structure, whose time evolution is shown in Fig 4.6, *i.e.* for both molecules we observe an identical percentage of alpha-helices and beta-sheets as well as their similar changes induced by the thermal fluctuations occurring during the dynamics. Concerning the Apo structure, the same arguments exposed before for the mutant K41C apply, *i.e.* one barely notices any structural change with respect to the Wt.

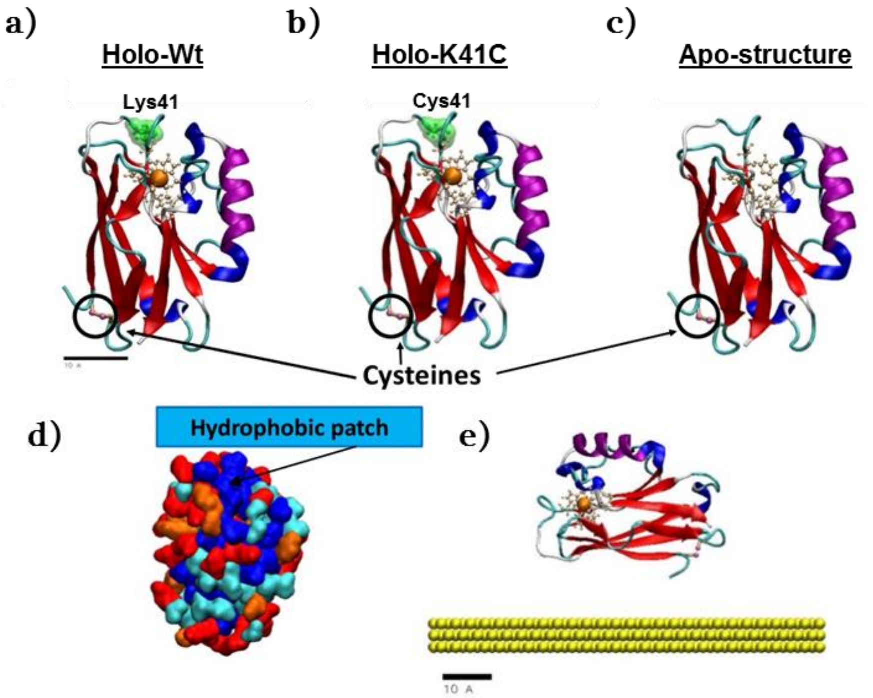

Figure 4.3. Initial configurations of the **(a)** Wt, **(b)** K41C and **(c)** Apo structures. The Azurin is represented with its secondary structure: beta-sheets (red), alpha-helix (purple), 310- helix (dark-blue), turns (cyan), and random-coils (white). The copper atom is shown using its Van- der-Waals representation in an opaque orange colour, and its coordination residues are represented with ball-stick model in a metallic-pastel orange colour. The disulphide bridge is shown in a bond representation coloured in light orange, and the main chain of two cysteines, which formed it are coloured in pink. Moreover, the position of the residue in which the mutation has been performed (Lysine replaced by a Cysteine) has been marked with a green Connolly surface. **(d)** Residue distribution for all the Azurin structures coloured in accordance with their hydrophobicity index: very hydrophobic (blue), hydrophobic (cyan), neutral (orange), and hydrophilic (red) residues. The orientation of the protein is the same as in a)-c). The Hydrophobic patch (near de cooper atom) of the protein is marked with a blue rectangle. **(e)** Representation of the configuration of the Cu-Azurin over the whole gold surface for one of the orientation studied (O1).

In summary, our molecular dynamics simulations for the free molecules indicate that both the structure and the dynamics of these three molecules are very similar. This conclusion is better seen in figure 4.7, where the aligned final configuration of the Wt and K41C structures (a) as well as the Wt and Apo structures (b) clearly show that structurally all these molecules are very similar.

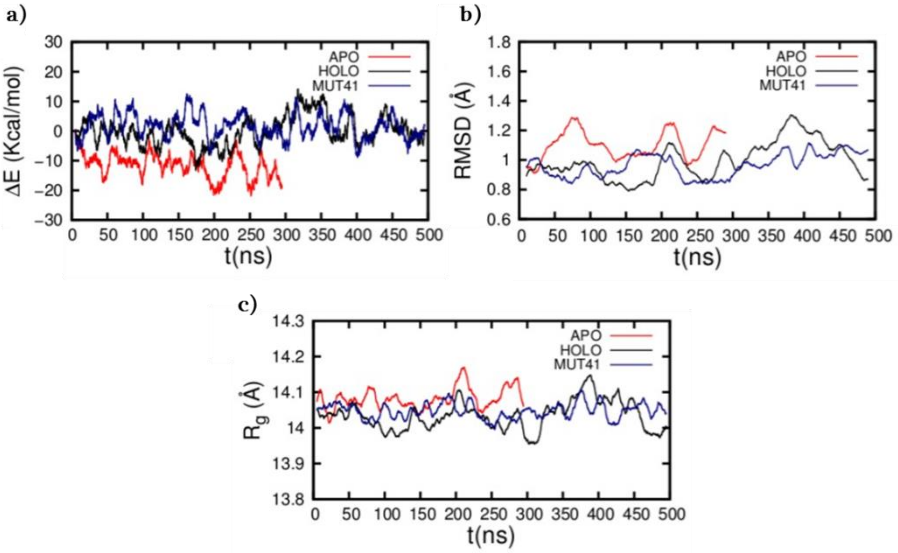

Figure 4.4. Evolution of the total energy change (top), the root-mean-square deviation, RMSD, (middle) and the radius of gyration, R_g, (bottom) for the Apo (red), Wt (black) and K41C (blue) structures during the simulation of its free dynamic in solution. The average of the total energy in the first 10 ns has been taken as our energy reference. RMSD has been calculated for all the backbone atoms of the protein. The Apo results go only until 300 ns as this simulation is shorter than the other two.

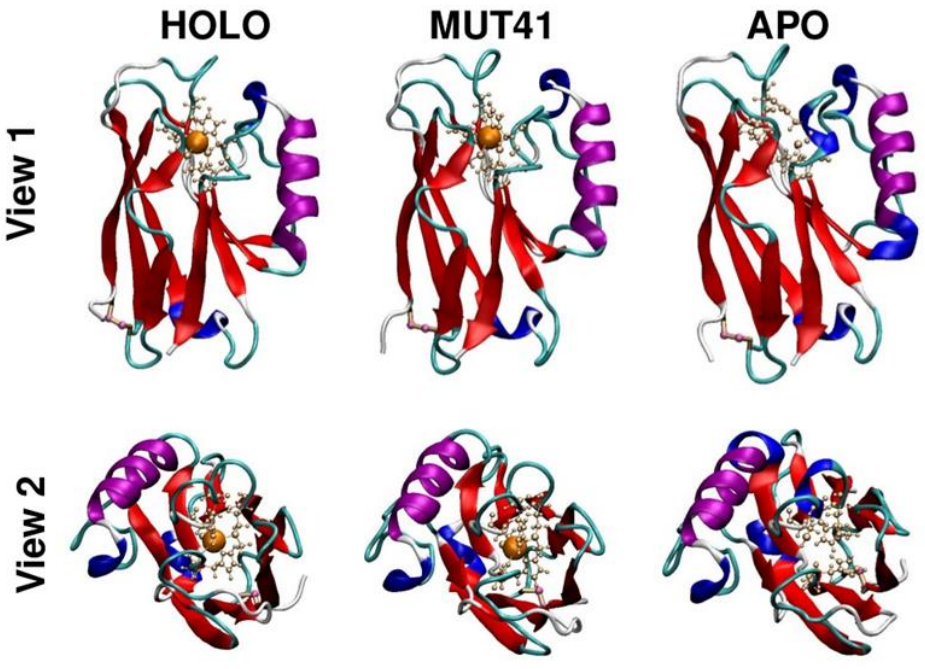

Figure 4.5. Final configurations obtained at the end of the simulation for the Apo (300 ns), Wt (500 ns) and K41C (500 ns) structures. Two different views of the protein are shown for each structure. The color representation used for the protein is the same as in figure 4.3.

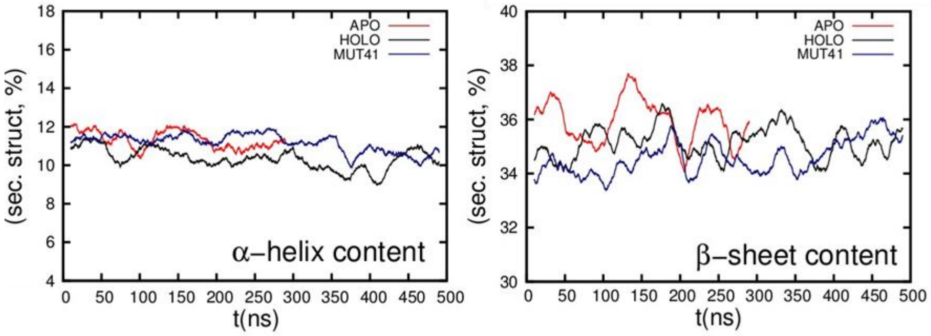

Figure 4.6. Time evolution of the percentage of α-helix and β sheet content for the Apo (red), Wt (black) and K41C (blue). As in figure 4.4, the Apo results go only until 300 ns as this simulation is shorter than the other two.

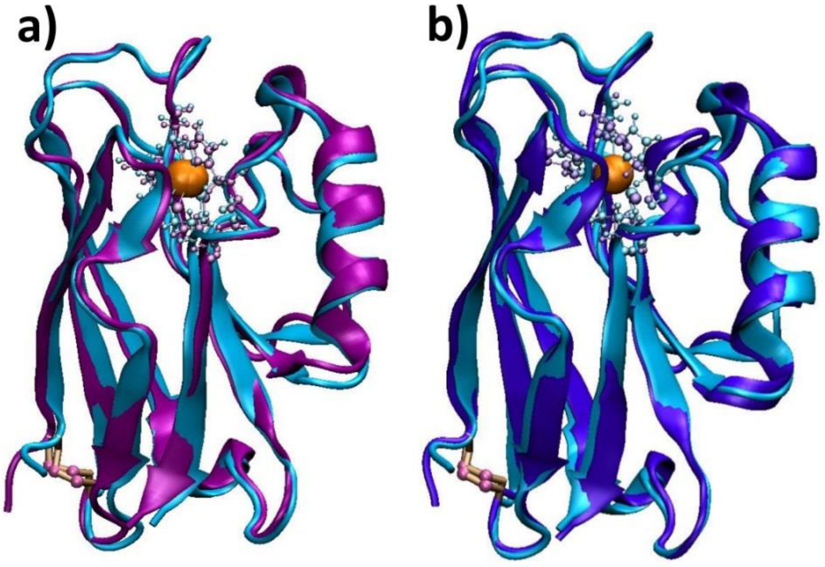

Figure 4.7. Comparison between the final configurations obtained at the end of simulation of **(a)** the Wt (cyan) and K41C (magenta) structures; and **(b)** the Wt (cyan) and Apo (purple) structures. In both cases, the two structures compared have been aligned with the program Visual Molecular Dynamics. The copper atom is shown in its Van-der-Waals representation in an opaque orange color, and the disulfide bridge is shown in a bond representation coloured in light orange.

4.2.2. MD simulations of Wt-Azurin adsorption over Au (111):

In this section, we access how the structure of the Wt-Azurin is affected by its adsorption to a gold surface, and also which are the most likely adsorption orientations for the Azurin on Gold. Note, that here we have only considered the Wt, given the structural similarity between the three molecules considered in the previous section.

We initially position the Azurin along four different orientations on top of the gold surface. The reasoning for these orientations is the following. Let us consider the Azurin as a cylinder, where its axis passes through the center of the beta-sheet barrel. Then one can orient this barrel either as being standing vertically over the surface with the cysteines close to it (figure 4.8 O2 initial) or with the cysteines the further away as possible from the surface (figure 4.8 O4 initial). Also we can place this barrel flat on top of the surface with the cysteins in close contact with the surface (figure 4.8 O1 initial), or with the cysteines the further away as possible from the surface (figure 4.8 O3 initial). In all cases the initial distance between the protein and the surface is above 1nm, so we give enough freedom for the protein to reorient itself if it must. Also it is important to notice that in all cases the system is fully embedded in water, which is not represented here for the sake of the simplicity of the representations. In all cases, once we have the protein oriented over the surface and the system solvated, we leave the protein to adsorb freely in a MD simulation that lasts 150ns, which we have found to be enough to reach a thermal equilibrium configuration.

Looking to the evolution of the total energy for the 4 orientations (see figure 4.9a, it is clear that the Wt is stably absorbed to the surface after 100ns of simulation, given that the time evolution of the total energy seem to be stable beyond that time for all orientations. Moreover, the absorption energy seems to be very similar in all cases. Note that although we have shown in previous works that total energies allow us to get a good estimate for relative energies of adsorption for the different orientations[33]. At last, concerning the adsorption process, we observed that in all cases the protein spontaneously absorbs over the gold surface, which is compatible with the fast sample preparation times seen in the experiments.

In figure 4.8, the final configurations obtained at the end of the simulation for the four Azurin orientations are showed. A close inspection of these figures allows us to concluded that the Cu-Azurin is absorbed to the gold surface via two different parts: the cysteines (O1 and O2), or the hydrophobic patch (O3 and O4). Note that in some cases, the protein needs a major reorientation. One clear example of this is seen for orientation O3, where the protein rotates over ninety degrees to adsorb via the hydrophobic patch. These two types of adsorptions are also evidenced by other observables. In fact, one realizes that the evolution of the RMSD of the protein (figure 4.9b) and the beta sheet content (figure 4.9b), clearly has two different trends. These two trends can be distinguish also in the evolution of the contact area (see figure 4.11 a): the O1 and O2 initial configurations are absorbed with larger contacts areas (more residues in contact with the surface, see footprints in figure 4.11 b), while de O3 and O4 orientations are less in contact with the surface, and use the hydrophobic patch as anchorage point.

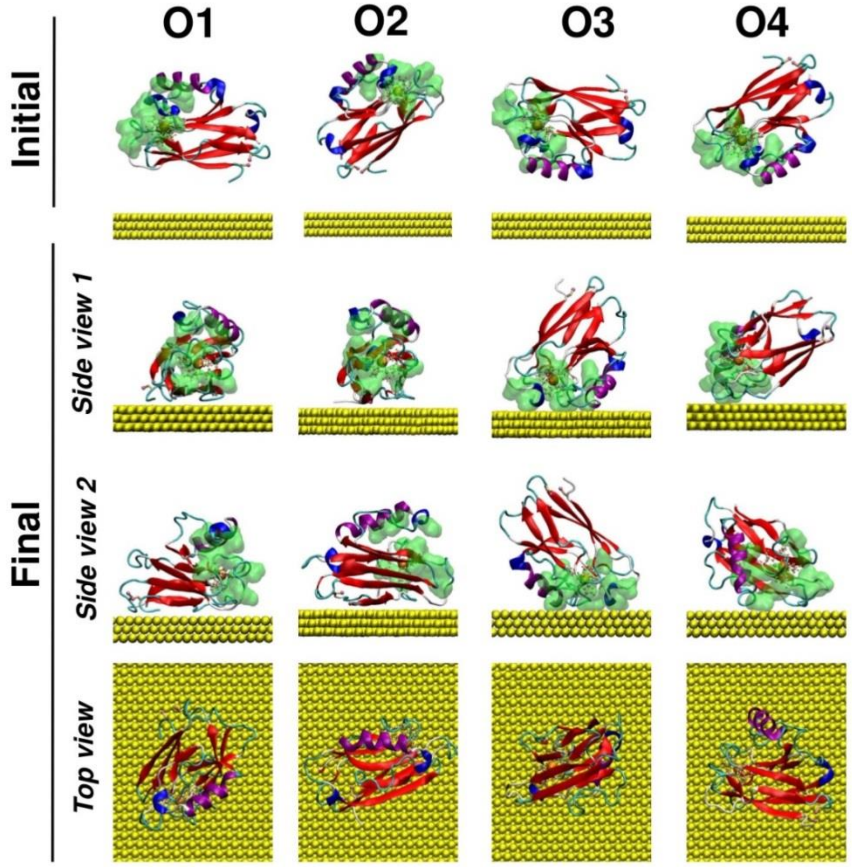

Figure 4.8. Snapshots of the initial and final configurations of the Cu-Azurin adsorbed in a gold surface for the four different orientations studied (O1, O2, O3 and O4). From top to bottom, the first row corresponds to the initial configuration of the Azurin. In the second and third rows, two different side views of the final configurations obtained after 150 ns of simulation are showed. The fourth row corresponds to the top view of the Azurin absorbed in gold at the end of the simulation. The color representation used for the protein is the same as in figure 4.3. Moreover, the position of the hydrophobic patch has been marked with a green Connolly surface[37].

In summary, we observed that upon adsorption to gold, Azurin seems to preserve most of its secondary structure (see figure 4.9 b). Furthermore, starting from four very different adsorption configurations, we saw that the Azurin stably adsorbed along two different orientations. These results highlight that process of adsorption of the Copper-Azurin is guided via two well-defined sites: the hydrophobic patch and the naturally cys3-cys26.

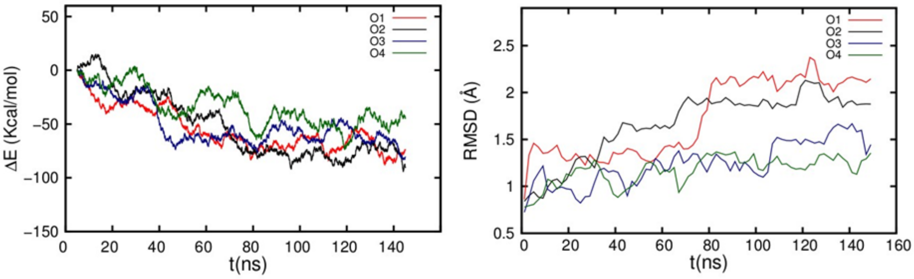

Figure 4.9. Evolution of the total energy change (left) and the root-mean-square deviation, RMSD, (right) for the four different orientations analyzed (O1, O2, O3 and O4) during the absorption of the Cu-Azurin in gold. The average of the total energy in the first 10 ns has been taken as our energy reference. RMSD has been calculated for all the backbone atoms of the protein.

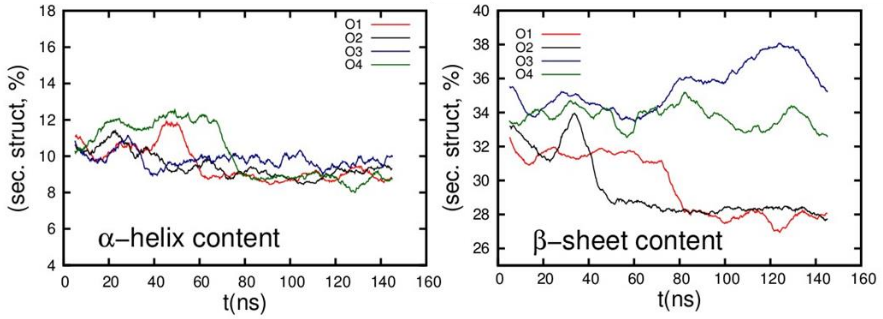

Figure 4.10. Time evolution of the percentage of α-helix and β sheet content for the four different orientations (O1, O2, O3, and O4) analyzed of the Cu-Azurin adsorbed to gold.

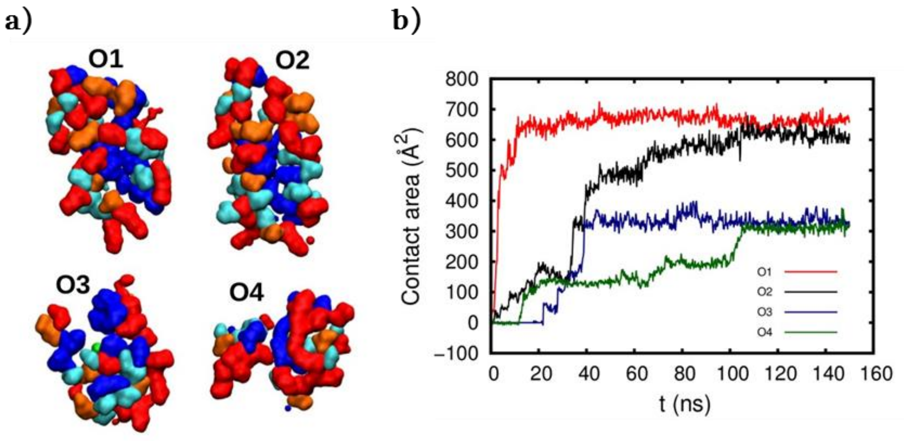

Figure 4.11. (**a**) Residue distribution for the Cu-Azurin zone facing the gold surface in the final configuration for the four orientations analyzed (O1, O2, O3, and O4). The residues color is in accordance with their hydrophobicity index: very hydrophobic, hydrophobic, neutral, and hydrophilic residues are colored in blue, cyan, orange, and red, respectively. The copper atom is colored in green. (**b**) Time evolution of the contact surface area in Å for the four orientations studied of the Cu-Azurin adsorbed in gold.

4.2.3. Influence of a gold tip on the structural stability of the Azurin as a function of the tip indentation height:

In this section, we access how the secondary structure of the Wt-Azurin is affected by the indentation of a gold tip. In these simulations, the tip moves towards the surface, while the protein adsorbed at the surface, is free to move and accommodate any deformation. In figure 4.12, we show some snapshots of such process. From these snapshots one observes that the secondary structure of the protein remains stable up to tip-surface distances of 2.3 nm. Beyond this indentation height, one observes that the Cu-Azurin starts to lose its secondary structure. This loss mostly occurs at the top alpha-helix. In contrast with this behavior we observe that the beta-barrel is able to sustain its secondary structure as we indent. In fact, during the indentation we observe how it goes from an almost cylindrical section barrel to a more ellipse alike. This additional degree of freedom allows this structure to better accommodate the deformation imposed by the tip. In fact, we observed that beta barrel seems to be stable even at tip-surface distances of 2 nm.

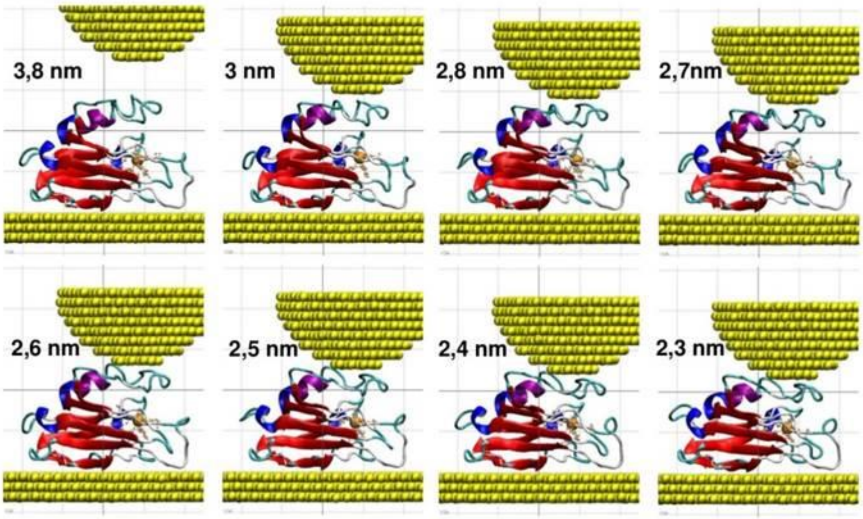

Figure 4.12. Snapshots of the configuration of the Wt-Azurin being indented by a gold tip. Here we have considered tip-surface separations ranging from 4 nm to 2 nm. From left to right, and top to bottom, the distance between the tip and the gold surface has been reduced. The color representation used for the protein is the same as in figure 4.3.

REFERENCES

1. Frisch, M. J. *et al.* Gaussian 09, Revision A.02. *Gaussian Inc Wallingford CT* **34,** Wallingford CT (2009).
2. Yanai, T., Tew, D. P. & Handy, N. C. A new hybrid exchange-correlation functional using the Coulomb-attenuating method (CAM-B3LYP). *Chem. Phys. Lett.* **393,** 51–57 (2004).
3. Peach, M. J. G. *et al.* Assessment of a Coulomb-attenuated exchange–correlation energy functional. *Phys. Chem. Chem. Phys.* **8,** 558–562 (2006).
4. Reimers, J. R., Cai, Z.-L., Bilić, A. & Hush, N. S. The appropriateness of density-functional theory for the calculation of molecular electronics properties. *Ann. N. Y. Acad. Sci.* **1006,** 235–251 (2003).
5. Reimers, J. R. *et al.* The Green's function density functional tight-binding (gDFTB) method for molecular electronic conduction. *J. Phys. Chem. A* **111,** 5692–5702 (2007).
6. Cai, Z. L., Crossley, M. J., Reimers, J. R., Kobayashi, R. & Amos, R. D. Density functional theory for charge transfer: The nature of the N-bands of porphyrins and chlorophylls revealed through CAM-B3LYP, CASPT2, and SAC-CI calculations. *J. Phys. Chem. B* **110,** 15624–15632 (2006).
7. Blanco-Rodríguez, A. M. *et al.* Phototriggering electron flow through ReI-modified pseudomonas aeruginosa azurins. *Chem. - A Eur. J.* **17,** 5350–5361 (2011).
8. Dreuw, A. & Head-Gordon, M. Single-reference ab initio methods for the calculation of excited states of large molecules. *Chemical Reviews* **105,** 4009–4037 (2005).
9. Jensen, L. & Govind, N. Excited states of DNA base pairs using long-range corrected time-dependent density functional theory. *J. Phys. Chem. A* **113,** 9761–5 (2009).
10. Orian, L., Carlotto, S., Di Valentin, M. & Polimeno, A. Charge transfer in model bioinspired carotene-porphyrin dyads. *J. Phys. Chem. A* **116,** 3926–3933 (2012).
11. Polander, L. E. *et al.* Solution-processed molecular bis(naphthalene diimide) derivatives with high electron mobility. *Chem. Mater.* **23,** 3408–3410 (2011).

12. Hanwell, M. D. *et al.* Avogadro: An advanced semantic chemical editor, visualization, and analysis platform. *J. Cheminform.* **4,** 1–17 (2012).

13. AMBER14. (2014). Available at: http://ambermd.org/.

14. Salomon-Ferrer, R., Götz, A. W., Poole, D., Le Grand, S. & Walker, R. C. Routine microsecond molecular dynamics simulations with AMBER on GPUs. 2. Explicit Solvent Particle Mesh Ewald. *J. Chem. Theory Comput.* **8,** 3878–3888 (2013).

15. Götz, A. W. *et al.* Routine microsecond molecular dynamics simulations with AMBER on GPUs. 1. generalized born. *J. Chem. Theory Comput.* **8,** 1542–1555 (2012).

16. Le Grand, S., Götz, A. W. & Walker, R. C. SPFP: Speed without compromise - A mixed precision model for GPU accelerated molecular dynamics simulations. *Comput. Phys. Commun.* **184,** 374–380 (2013).

17. Pérez, A. *et al.* Refinement of the AMBER force field for nucleic acids: improving the description of alpha/gamma conformers. *Biophys. J.* **92,** 3817–29 (2007).

18. Cornell, W. D. *et al.* A second generation force field for the simulation of proteins, nucleic acids, and organic molecules. *J. Am. Chem. Soc.* **117,** 5179–5197 (1995).

19. Van Den Bosch, M. *et al.* Calculation of the redox potential of the protein azurin and some mutants. *ChemBioChem* **6,** 738–746 (2005).

20. Paltrinieri, L. *et al.* The active site loop modulates the reorganization energy of blue copper proteins by controlling the dynamic interplay with solvent. *J. Phys. Chem. Lett.* **4,** 710–715 (2013).

21. Beedle, A. E. M., Lezamiz, A., Stirnemann, G. & Garcia-Manyes, S. The mechanochemistry of copper reports on the directionality of unfolding in model cupredoxin proteins. *Nat. Commun.* **6,** 7894 (2015).

22. Zanetti-Polzi, L. *et al.* A few key residues determine the high redox potential shift in azurin mutants. *Org. Biomol. Chem.* **13,** 11003–11013 (2015).

23. Zanetti-Polzi, L., Corni, S., Daidone, I. & Amadei, A. Extending the essential dynamics analysis to investigate molecular

properties: application to the redox potential of proteins. *Phys. Chem. Chem. Phys.* **18,** 18450–18459 (2016).

24. Jorgensen, W. L., Chandrasekhar, J., Madura, J. D., Impey, R. W. & Klein, M. L. Comparison of simple potential functions for simulating liquid water. *J. Chem. Phys.* **79,** 926 (1983).

25. Joung, S. & Cheatham, T. E. Molecular dynamics simulations of the dynamic and energetic properties of alkali and halide ions using water-model-specific ion parameters. *J. Phys. Chem. B* **113,** 13279–13290 (2009).

26. Li, P., Roberts, B. P., Chakravorty, D. K. & Merz, K. M. Rational design of particle mesh ewald compatible lennard-jones parameters for +2 metal cations in explicit solvent. *J. Chem. Theory Comput.* **9,** 2733–2748 (2013).

27. Heinz, H., Lin, T. J., Kishore Mishra, R. & Emami, F. S. Thermodynamically consistent force fields for the assembly of inorganic, organic, and biological nanostructures: The INTERFACE force field. *Langmuir* **29,** 1754–1765 (2013).

28. Heinz, H. & Ramezani-Dakhel, H. Simulations of inorganic-bioorganic interfaces to discover new materials: insights, comparisons to experiment, challenges, and opportunities. *Chem. Soc. Rev.* **45,** 412–448 (2016).

29. Berman, H. M. *et al.* The protein data bank. *Nucleic Acids Res.* **28,** 235–242 (2000).

30. Nar, H., Messerschmidt, A., Huber, R., van de Kamp, M. & Canters, G. W. Crystal structure analysis of oxidized Pseudomonas aeruginosa azurin at pH 5.5 and pH 9.0. A pH-induced conformational transition involves a peptide bond flip. *J. Mol. Biol.* **221,** 765–772 (1991).

31. Gordon, J. C. *et al.* H++: A server for estimating pKas and adding missing hydrogens to macromolecules. *Nucleic Acids Res.* **33,** 368–371 (2005).

32. Connolly, M. L. Analytical Molecular Surface Calculations. *J. Appl. Cryst.* **16,** 548–558 (1983).

33. Vilhena, J. G., Rubio-Pereda, P., Vellosillo, P., Serena, P. A. & Pérez, R. Albumin (BSA) Adsorption over Graphene in Aqueous Environment: Influence of Orientation, Adsorption Protocol, and Solvent

Treatment. *Langmuir* **32,** 1742–1755 (2016).

5

SINGLE-PROTEIN WIRES

5. SINGLE-PROTEIN WIRES

We have bioengineered Azurin from *Pseudomonas aeruginosa* to include a single point mutation in the outer shell (see chapter 3). The aim was to incorporate a new anchoring group that serves as a new chemical connection to one of the external device terminals (in our STM system is represented by the probe or the sample electrode) for single-protein wiring. Additionally, the different electrochemical behaviour observed in chapter 3 for the different Azurin variants is expected to change the transport regime through the protein matrix, due to the modification in the secondary copper coordination sphere.

After the expression, production and purification of the Azurin variants, we studied the electron transport (ETp) through the single-protein using an EC-STM configuration. We individually trap proteins between the STM probe and sample electrode in a physiological environment under a bipotentiostatic control (see chapter 2). The ETp was then characterized as a function of an applied electrochemical gate voltage, and in a particular mutant (K41C) and Wt Azurin as a function of temperature.

5.1. Wt and K41C Azurin electron transport

5.1.1. Electrochemical gate-dependent single-protein transport

We have built and electrically characterized single-protein wires in a physiological environment (ammonium acetate buffer pH 4.5) for both target systems, *i.e.* the Wt and the K41C variant. To this aim, the target proteins are absorbed onto a clean Au(111) electrode surface and an electrochemical Scanning Tunnelling Microscope (EC-STM) break-junction approach is used to bridge individual proteins between both the Au(111) substrate and the Au STM tip electrodes under electrochemical control (figure 5.1). Molecular simulations in chapter 4 showed that Cu-Azurin adsorption to gold occurs either through the naturally present *Cys* residues or through the hydrophobic patch through minor loss of the secondary structure of the protein. Both simulations and experiments indicate that the protein attachment to Au substrate is stable and allows imaging individual redox-active proteins on the electrode surface for long time periods of up to several hours (figure 5.2). A similar anchoring geometry will be expected for the K41C mutant given that this residue is located in the hydrophobic patch, which is one of the two preferential adsorption sites of the Wt.

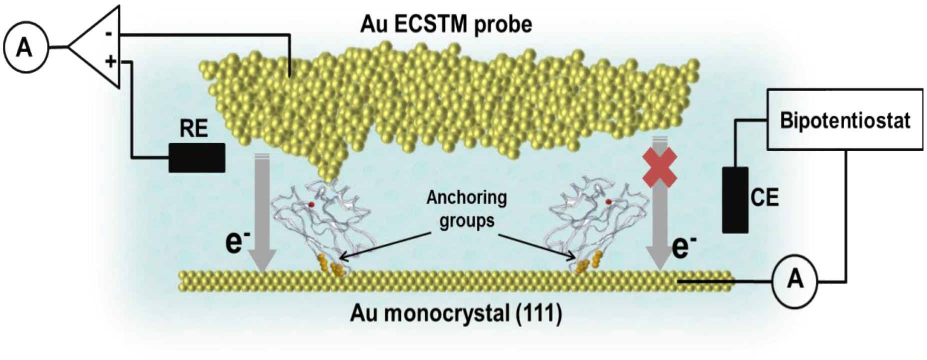

Figure 5.1. Schematic representation of the single-protein junctions in the EC-STM setup using the working electrolyte. The two natural *Cys* residues are used to form a stable thiol-gold protein attachment to the Au (111) substrate[27,31]. The top STM probe was used to close the electrical metal/protein/metal electrical contact.

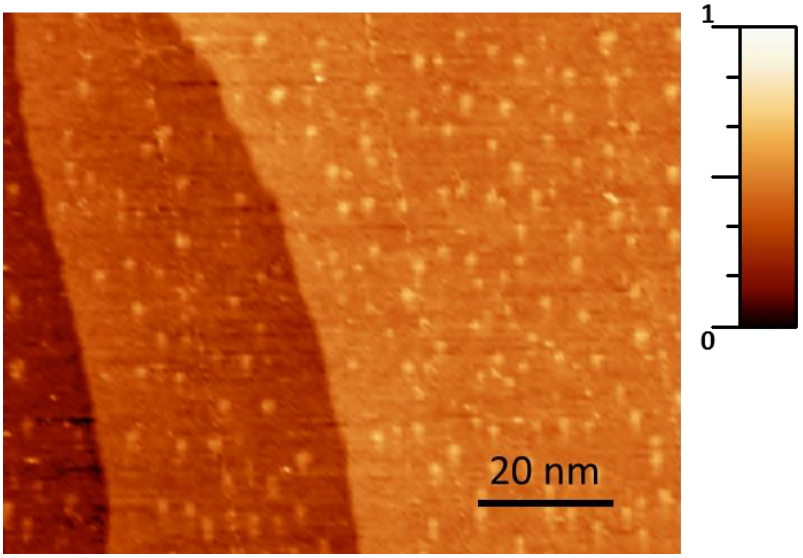

Figure 5.2. EC-STM image of a Wt Azurin-functionalized Au(111) surface in 50 mM ammonium acetate pH 4.5. The image was recorded at U_{sample} = 0.2 V and constant V_{bias} of 0.3 V.

To avoid interferences from protein-protein interactions in the single-protein junction experiments, we have used low protein coverage of the Au(111) substrate. To test the protein surface coverage, EC-STM imaging is performed prior to each single-protein junction experiment. Figure 5.2 shows a representative image of a protein functionalized Au(111) surface. Such distribution prevents the binding of multiple proteins in one molecule junction.

The EC-STM approach is operated in two different modalities, namely dynamic *tapping* and static *blinking*. In the former, the STM tip electrode is continuously approached and retracted to/from the Au electrode substrate where the target protein is anchored. When an individual protein binds the STM tip electrode and closes the gap, a single-protein junction is formed displaying a typical quantum conductance plateau feature in the current versus distance retracting curve[1]. Hundreds of such retracting curves (Fig. 5.3b-d) are then accumulated into a single 1D conductance histogram for each particular applied electrochemical potential (figure 5.3a). We have previously demonstrated the feasibility of this method to study the charge transport in a single-Azurin (Wt) junction as a function of the applied electrochemical (EC gate) potential[2] (EC gate = $-U_{sample}$, where U_{sample} is the substrate electrochemical potential). Figure 5.3 shows the dynamic measurements of the single-protein transport conductance values of the K41C mutant as a function of the applied EC gate. In stark contrast with the Wt behaviour, the single-protein junction of the K41C mutant shows no transistor behaviour, *i.e.* the conductance is invariable versus the EC gate within the relevant redox potential window. The transport behaviour in the Wt is characterized by a 2-step sequential tunnelling that results in a maximum in the conductance versus EC gate[2,3] (figure 5.3e, c), and the invariance of the conductance in the K41C suggests a direct tunnelling transport for the mutant[4].

This 2-step sequential tunnelling is considered in an adiabatic limit because the strong electronic coupling between the molecule and both adjacent electrodes. The first step of the sequential tunnelling is a situation where the Fermi level of the left electrode approaches the LUMO of the molecule due to the applied voltage, but is still located below it. The molecular LUMO may decrease its energy due to fluctuations and approach the Fermi level of the left electrode, causing the first ET. Then, the energy of the now occupied LUMO decreases due to the vibrational relaxation, and the second ET step occurs before complete vibrational relaxation and before the energy of the molecular level passes the Fermi level of the second electrode. Subsequently, the empty LUMO starts to relax toward higher energies and may accept another electron from the left electrode (substrate) before it passes its Fermi level, thus repeating the cycle. The process may comprise many cycles of consecutive molecular reduction and reoxidation steps per single initial fluctuation of the molecular level (figure 5.4).

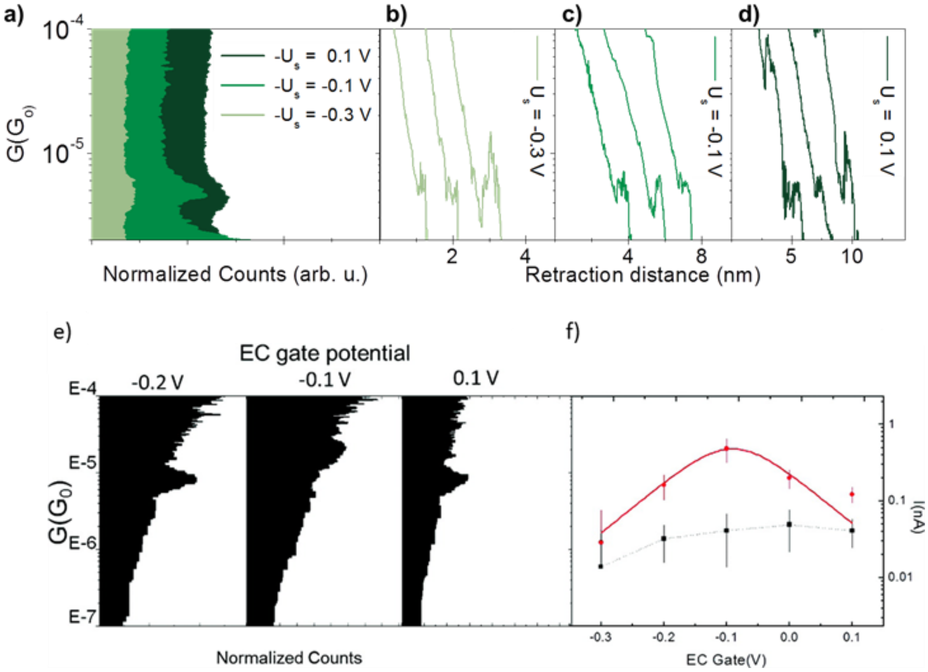

Figure 5.3. ***Dynamic* single-protein transport of the K41C junction. a**, Conductance histograms at three extreme EC gate potentials ($-U_{Sample}$ in our EC-STM configuration) covering the redox potential window for the K41C protein. The histograms were built out of hundreds of retracting curves (Conductance (G) *vs.* retraction distance (nm)) from the break junction experiments displaying quantum conductance plateau features. **b-d**, Three representative retracting curves containing plateau features at the three applied EC gate potentials (dark green 0.1 V, green -0.1 V, light green -0.3 V). An offset was applied in the X-axis in all plots for better visualization. A constant 300 mV voltage bias ($V_{bias} = U_{sample} - U_{tip}$, where U_{sample} and U_{tip} are the Au substrate and STM tip electrochemical potentials, respectively) was applied. **e)** Semilogarithmic conductance histograms obtained from Azurin experiments at different electrochemical gate voltages and constant bias conditions (300 mV). **b)** Conductance values obtained from the centre of the Gaussian fit of the histograms peaks as a function of EC gate potential at constant 0.3 V bias for Azurin (red circles) and non-redox Zn–Azurin junctions (black squares). Error bars indicate the full width half-maximum (fwhm) of the Gaussian fit on each conductance peak. All experiments were performed in 50 mM ammonium acetate solution (pH 4.55)[2] (With permission).

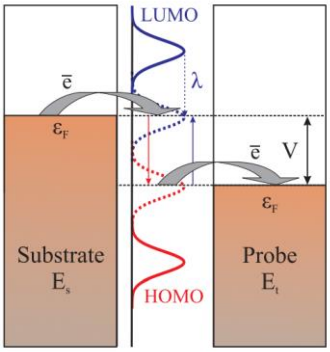

Figure5.4. Schematic electronic energy diagram of the two step ETp mediated by the redox-active molecule. The electron is transferred from the Fermi level of the sample (left) to the LUMO of the molecule and after partial vibrational relaxation to the Fermi level of the probe (right).

The total enhanced current I_{enh} (redox mediated enhanced) is given by

$$\frac{1}{I_{enh}} = \frac{1}{I_1} + \frac{1}{I_2} \qquad (1)$$

where I_1 and I_2 are the currents due to the substrate-molecule and molecule-tip ETp, respectively.

$$I_1 = e\kappa_1\rho_1(eV_{bias})\frac{\omega}{2\pi}exp\left[-\frac{(\lambda+e\xi\eta+e\gamma V_{bias})^2}{4\lambda\kappa T}\right]^{-1} \qquad (2)$$

$$I_2 = e\kappa_2\rho_2(eV_{bias})\frac{\omega}{2\pi}exp\left[-\frac{(\lambda-e\xi\eta+e\gamma V_{bias}+eV_{bias})^2}{4\lambda\kappa T}\right]^{-1} \qquad (3)$$

Here e is the elementary charge, κ is the electronic transmission coefficient, F is the density of electronic states in the metal near the Fermi level, ω is the characteristic nuclear vibration frequency, and k is the Boltzmann constant. ξ and γ are model parameters ranging between 0 and 1 describing the fraction of the overpotential η in Volts (η = U_{sample} - U_{redox}, where U_{redox} corresponds to the protein redox midpoint extracted from figure 3.8) and the V_{bias} (in Volts) felt by the reactive redox centre in the molecular junctions, respectively. T (in °C) is the temperature and λ (in eV) is the reorganization energy (the energy difference between the oxidised and reduced states of the protein). All other physical constants have been numerically processed for simplicity taking reasonable assumptions of our experimental setup such as fully adiabatic limit (strong molecule/electrode coupling), fixed junction geometry for every measured *blink*, Au as electrode materials and aqueous solution as the environment. Assuming the same values of κ and F for both ETs, one obtains the following dependence of I_{enh} on V_{bias} and η at a fixed geometry of the tunneling junction (eq 4):

$$I_{enh} = e\kappa\rho(eV_{bias})\frac{\omega}{2\pi}\left[e^{\left(\frac{e}{4\lambda\kappa T}(\lambda+\xi\eta+\gamma V_{bias})^2\right)} + e^{\left(\frac{e}{4\lambda\kappa T}(\lambda+V_{bias}-\xi\eta-\gamma V_{bias})^2\right)}\right]^{-1} \quad (4)$$

$$I_{enh} = 1820V_{bias}\left[e^{\left(\frac{2898}{\lambda T}(\lambda+\xi\eta+\gamma V_{bias})^2\right)} + e^{\left(\frac{2898}{\lambda T}(\lambda+V_{bias}-\xi\eta-\gamma V_{bias})^2\right)}\right]^{-1} \quad (5)$$

Single-biomolecular transport results by means of the dynamic STM break-junction approach has been previously shown in many instances[2,5–9]. However, the force exerted over the folding structure of the biomolecule in every pulling cycle (figure 5.3b-d) might disrupt its structure and lead to a misinterpretation of the single-biomolecule transport data. Here we rule out this uncertainty by using a static version of the EC-STM break-junction approach, namely, the *blinking* mode[10,11]. The STM tip electrode is initially approached to the Au(111) substrate where the proteins have been pre-adsorbed to a distance of few nanometres, which is achieved by imposing a small (~100 pA) tunnelling current set point at an applied bias voltage difference between the two electrodes (bias voltage (V_{bias}) = U_{sample} - U_{tip}). Once the STM tip-to-substrate gap is mechanically stable, the current feedback loop is turned off and the tunnelling current is monitored. Spontaneous trapping of proteins between both Au electrodes results in a telegraphic noise in the measured tunnelling current flowing between the electrodes, which appears in the form of sudden “jumps” (*blinks*) [10,12]. In support of this picture, our previous MD simulations of an STM tip approaching a Wt Azurin stably absorbed on the Au(111) substrate (see chapter 4) showed that the protein folding structure remains stable even after the STM tip establishes physical contact to it at distances close to 2.5 nm.

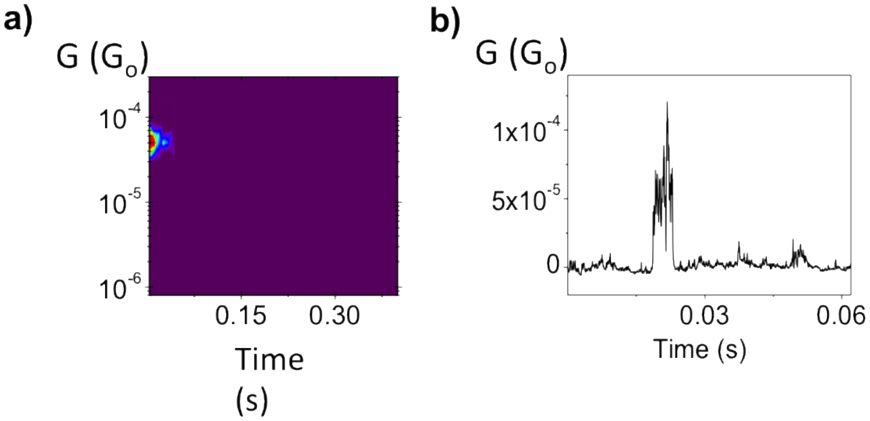

Figure 5.5. a) 2D-blinking map obtained for the single-protein Wt junction at an EC gate of -0.1 V (constant bias of 0.3 V). The tip was retracted 2 nm from the surface from the initial set point tunnelling distance. **b)** A representative *blink* obtained after retracting the STM tip electrode.

In order to corroborate that the observed *blinks* correspond to individual protein trapping events, larger electrode-electrode separations were imposed by retracting the STM tip electrode 2 nm further away from the distance set by the initial tunnelling current set point (~1.5 nm). At that moment the STM probe is no longer in tunnel regime. However, we observe that the large protein backbone is still capable of closing the larger electrode-electrode gap separation (~3.5 nm) resulting in a similar telegraphic signal in the *blinking* experiment (Figure 5.5).

Figure 5.6b panels show the accumulation of tens of such *blinking* traces into single 2D-maps at different applied EC gate potentials for the Wt (top panel) and the K41C mutant (bottom panel). Such 2D *blinking* maps[10,13] are built by setting all *blinking* features from individual current transients (figure 5.6a) to a common time origin and subtracted tunnelling background, and represent solely the net conductance flowing through the protein wire. The horizontal fringe observed in the 2D blinking maps represents the most likely conductance values of the single-protein wire, whose average values are represented as a function of the applied EC gate in the far right graph of figure 5.6b (1D conductance histograms used to extract such values). Comparable conductance values are obtained from the static 2D-maps (figure 5.6b) and the dynamic break-junction histograms (figure 5.3) for the K41C variant, $5{\cdot}10^{-6}G_o$ and $3{\cdot}10^{-6}G_o$ respectively (G_0=77.5 μS), being on average slightly larger in the former, which might evidence the detrimental effect of the protein “stretching” in the latter method. The single-protein conductance in figure 5.6b for the K41C follows the same non-dependent EC gate behaviour observed in the dynamic break-junction experiments (figure 5.3), with a slightly lower off-resonance current (at an EC gate voltage of -0.3 V) when compared to the single-Wt junction (figure 5.6b upper panel). As expected in the latter case, a maximum in the conductance versus the EC gate potential near the mid-redox value is observed for the Wt (figure 5.6b far right panel)[2] as opposed to the invariability for the single-K41C mutant junction conductance behaviour within the same relevant redox potential range. These results suggest a sharp change in the transport behaviour of the single-protein wire, going from a classic sequential 2-step tunnelling for the Wt, observed in a number of other redox molecular junctions[2,14,15], to a fully coherent tunnelling for the K41C mutant. A numerical version of the 2-step tunnelling model presented above is given in equation (5) and expresses the enhanced current (I_{enh} in nanoamps) flowing through the molecular junction[14]. A fit of the Wt experimental results (blue line in figure 5.6b far left graph) yields reasonable values for λ, ξ and γ, 0.27 eV, 0.95 and 0.79, respectively[2,16], evidencing low reorganization energies, large EC gating efficiencies and a slight asymmetric V_{bias} distribution due to the usually asymmetric location of the Cu centre in the molecular junction.

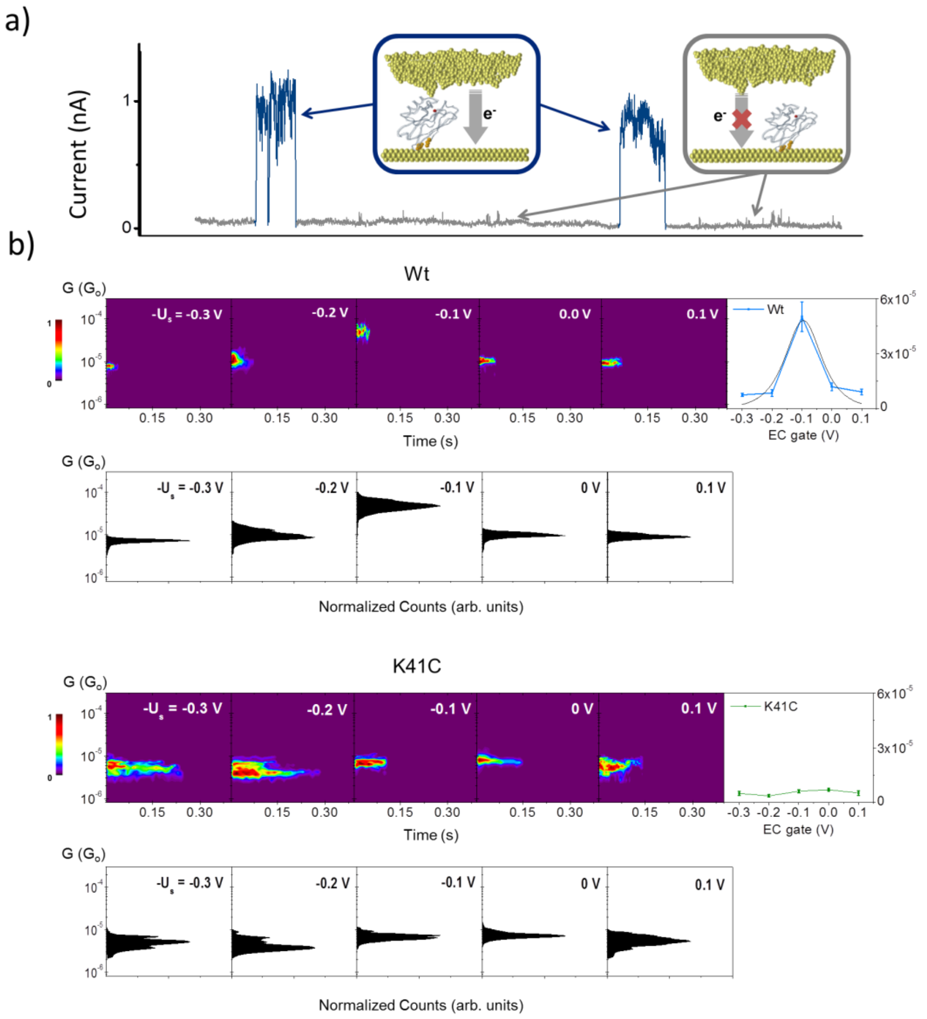

Figure 5.6. Gate-dependent single-protein transport. a, Representative "*blinks*" (blue lines) identified in the transients of the current flowing between the two electrodes at a constant distance (2 to 3.5 nm) and V_{bias} (300 mV). Such *blinks* are observed when a protein spans the gap between the EC-STM tip and the Au substrate electrodes. When the protein disconnects from one of the electrodes, the current drops down to the initial set point level. $G=I_{step}/V_{bias}$ is used to obtain the conductance values. **b**, 2D-blinking maps for both proteins (Wt top and K41C bottom) at different EC gate potentials. Several tens (up to a hundred) of individual blinking traces like that shown in **a** are accumulated to build each 2D-map without any selection. The counts have been normalized for each map versus the maximum value so that each 2D map has its maximum count set to 1. The far right graphs summarize the average single-protein conductance (G) vs. the EC gate (V) for both studied proteins. The average conductance values were obtained from the Gaussian fits of the maxima in the vertical 1D

histogram for each 2D map. The error bars in these plots are extracted from the full width half-maximum (FWHM) of the Gaussian fits.

5.1.2. Temperature-dependent single-protein transport.

In order to search for possible sources of fully incoherent transport in any of the studied single-protein wires (*i.e.* hopping transport regime, see figure 5.7[17,18]), we have conducted single-protein transport measurements as a function of temperature, because hopping mechanism is temperature activated process as observed in equation 6:.

$$I = e\frac{e^{-\Delta E/\kappa_B T}}{[1/\kappa_L + 1/\kappa_R + (N-1)/\kappa]}\left[e^{\frac{eV}{\kappa_B T}} f_L - f_R\right] \qquad (6)$$

Where f_R and $f_L$are the Fermi functions describing the electron occupations on the left and right electrodes, T is the temperature, and the N is the number of states and the incoherent tunnelling between them is described by the transfer rates κ. The influence of the activation energy, ΔE, of the bias voltage, V, is taken into account.

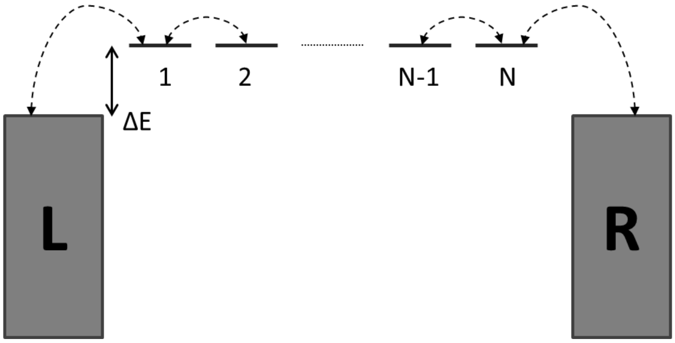

Figure 5.7. Schematic representation of the incoherent tunnelling model in a molecular junction. Here, N sites with the same energy are connected via nearest-neighbour transfer rates κ. The continua on the left and right correspond to the metallic states in the electrodes and ΔE is the activation energy.

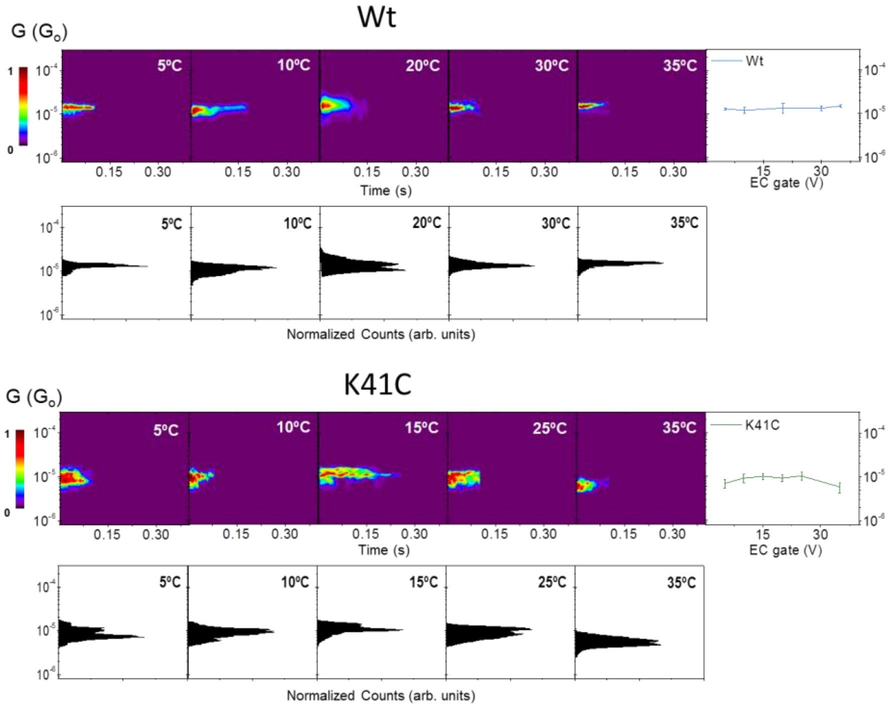

Figure 5.8. Temperature-dependent single-protein transport. 2D-blinking maps for both proteins (Wt top and K41C bottom) at different temperatures (from 5 to 35ºC), constant distance (2 to 3.5 nm) and V_{bias} (300 mV). The applied EC gate value was set to 0 and -100 mV for Wt and K41C mutant respectively. The counts have been normalized for each map versus the maximum value, so each 2D map has its maximum count set to 1. The far right graph summarizes the single-protein conductance (G) vs. temperature (°C) for both studied proteins. The average conductance values were obtained from the maxima Gaussian fits in the vertical 1D histogram for each 2D map. The error bars in these plots are extracted from the full FWHM of the Gaussian fits.

Figure 5.8 shows the temperature-dependent single-protein conductance results for both proteins at EC gate potentials of 0 and -100 mV (we select these potentials to set the 2-step sequential regime) for the Wt and the K41C mutant, respectively, near their respective redox midpoint potentials. The temperature range covers the room temperature conditions and approaches physiologically relevant values (~37 ºC)[19]. The maximum temperature values were kept below 40 ºC to prevent any denaturalization of the protein structures (84.4 ºC for the Wt[20] and >70 ºC for the K41C (see chapter 3)). The invariance of the single-protein wire conductance versus temperature in both proteins rules out any fully incoherence source of transport within the relevant temperature range and underscores the important fact that the protein is able to maintain a high level of coherence even for very different transport regimes, namely 2-step sequential and direct tunnelling. Similar behaviour has been also observed in microscale solid-state devices sandwiching a Wt Azurin protein[4]. The temperature-dependent conductance within the 2-step sequential scenario (see equation (1)) shows a very shallow trend as we approach the η=0 point ($U_{sample}=U_{redox}$), at which the measurements were performed. Figure 5.9 shows the conductance dependence on temperature for a sequential 2-step tunnelling mechanism described by the equation (4). Due to the sharp increase in conductance as the η=0 point is approached, the curves show the current-normalized first derivative at the different η. Building upon this mechanistic analysis, the invariance of the K41C single-protein wire against both EC gate potential and temperature suggests a complete loss of the Wt sequential tunnelling character, turning into a fully coherent tunnelling regime[21].

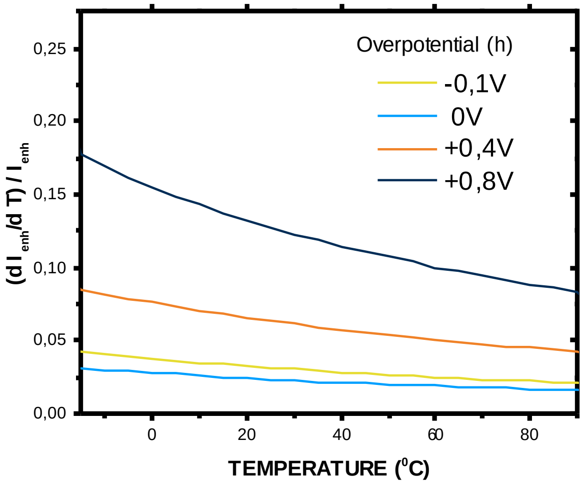

Figure 5.9. Temperature-dependent conductance in a sequential 2-step model. Temperature-dependent enhanced current plots at different values of applied overpotential η for a sequential 2-step tunnelling model. The representation shows the first derivative normalized by the current at each point.

5.1.6. *Blinking* control experiments

Additional controls of *blinking* experiments were conducted to ensure that no blinking features (absence of protein bridge formation) are obtained corroborating that only functional folded proteins are able to close the gap. *Blinking* current traces were recorded for three control samples: 50 mM ammonium acetate buffer pH 4.55 without any protein, denaturized-Wt (Den-Wt) and denaturized-K41C mutant (Den-K41C) both in the same buffer (ammonium acetate, pH 4.55). Up to a several tens of traces as for those recorded in figure 5.6b and 5.8. In the three cases, no apparent "*blinks*" were observed (figure 5.10), which means that 'blinks' are only produced by proteins in its 3D conformation. Neither the buffer nor denaturized proteins are contributing to the measurements.

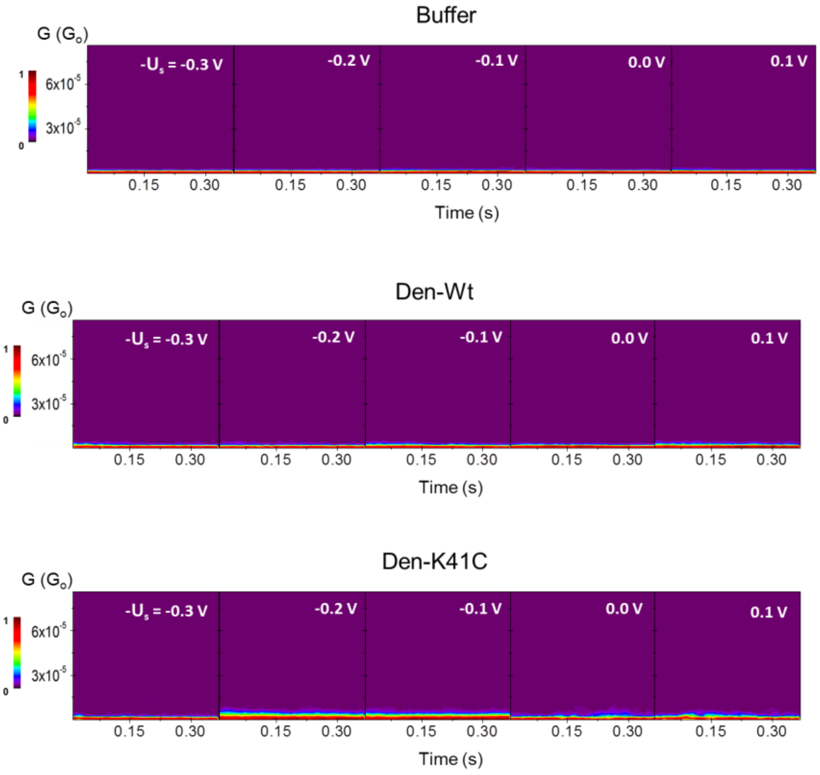

Figure 5.10. Control *blinking* measurements. 2D *blinking* maps are shown for Buffer, Den-Wt and Den-K41C corresponding to protein-free 50 mM ammonium acetate buffer pH 4.55, denaturized-Wt and denaturized-K41C (both in the same buffer) respectively. The histograms were recorded at different EC gate and constant bias of 0.3 V. 2D graphs have normalized counts being the maximum count level set to 1.

5.1.4. Blinking of Apo-proteins

To evidence the role of the Cu centre in the charge transport through the single-protein junction, we have recorded blinking traces as a function of the EC gate for the Apo-Wt and Apo-K41C mutant, both lacking the copper centre in their structure (figure 5.11). The results show conductance invariance against the EC gate in both cases. It evidences the direct involvement of the copper centre in the two-step sequential tunnelling in the former case, as well as the poor participation of the Cu centre in the mutated protein.

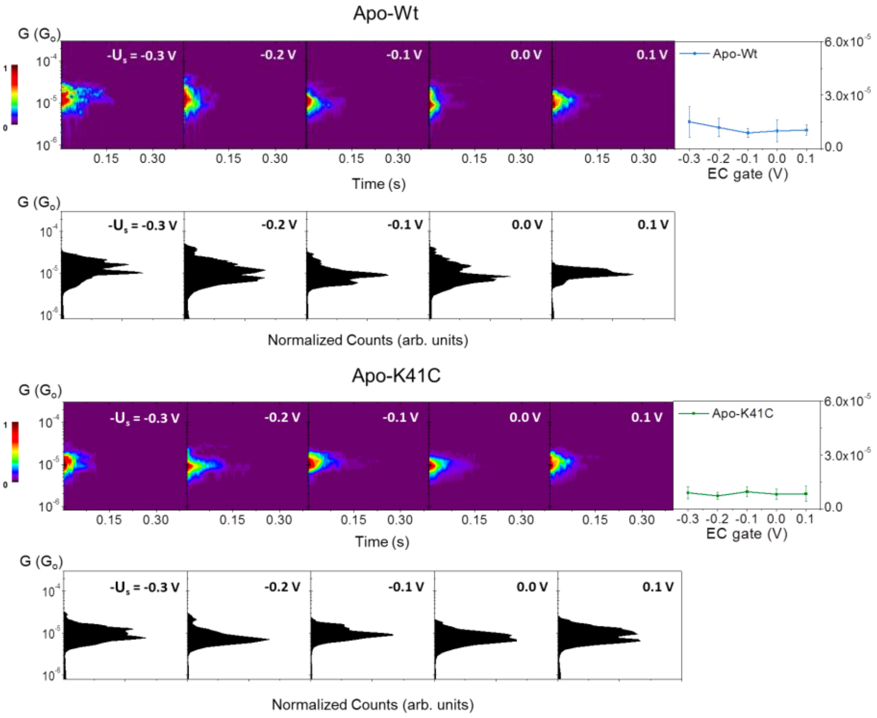

Figure 5.11. Gate-dependent single-Apo-proteins junction transport. Conductance behaviour versus EC gate ($-U_{sample}$ in our EC-STM configuration) at constant bias of 300 mV for the Apo-Wt and Apo-K41C. 2D *blinking* maps (top) and 1D histograms (bottom) are shown for each of the two proteins. The counts have been normalized for each map versus the maximum value so each 2D map has its maximum count set to 1. The far right graph summarizes the single-protein conductance (G) vs. the EC gate for both studied proteins. The conductance values were obtained from the Gaussian fit maxima of the 1D histogram. The error bars in these plots are extracted from the full width half-maximum (FWHM) of the Gaussian fits.

5.1.5. Analysis of the single-protein junction lifetimes

From the blinking experiments performed, we can extract additional information to compare the single-protein wire stability between Wt (only one covalent anchoring point) and K41C (two opposite sites for covalent bond formation to gold electrodes). Figures 5.12 and 5.13 show histograms of the extracted lifetime from each 2D *blinking* map (X-axis) recorded for the Wt and K41C variant (figure 5.12) and both Apo-proteins (figure 5.13). To construct these lifetime histograms we have considered all the blinks used in each case. From each blink we get the time value at what the blink is broken (considering as 0 the formation of the blink). This time difference is the lifetime of each single-protein wire. The lowest scored values correspond to the apo-proteins, which points toward a mechanical stabilization role of the Cu centre. It was previously reported by Giannotti et al. the copper function for structure stabilization[22]. They had mechanically unfolded Wt holo and apo Azurin using single-molecule force spectroscopy (SMFS) with an AFM. Though the comparison of force extension curves they saw that using the same force only apo-protein can be totally unfold, which let them to conclude the key role of copper in the 3D structure stability and not only for the ET. Likewise, the single-protein junction built with the holo proteins (with Cu centre) scores larger lifetimes. Interestingly, the mutation introduced at the second coordination sphere of the Cu centre in the K41C mutant enhances the mechanical stability of the single-protein junctions (significantly larger lifetimes scoring the longest lifetimes) thanks to the additional thiol anchoring group introduced at the bioengineered *Cys* residue at position 41. In support to this picture, we have functionalized Au nanoparticles (NP) with both Wt and K41C variants and detected a significantly larger percentage of multimeric Au NP structures (see chapter 3), evidencing the enhanced K41C bridging capability. Such configuration leads to a similar metal/protein/metal orientation in the K41C junction as compared to the Wt protein (see chapter 4).

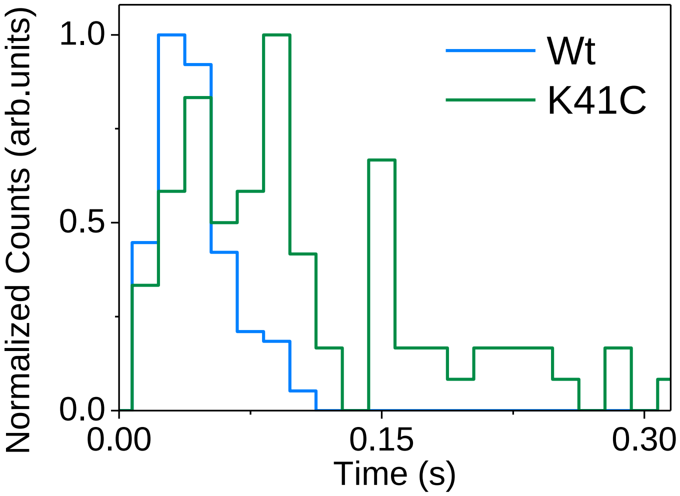

Figure 5.12. The lifetimes of the observed *blinks* for Wt (blue line) and K41C (green line) are represented. All the *blinking* traces from the gate dependent single-protein transport were included in the calculation. The counts of both Wt and K41C were normalized.

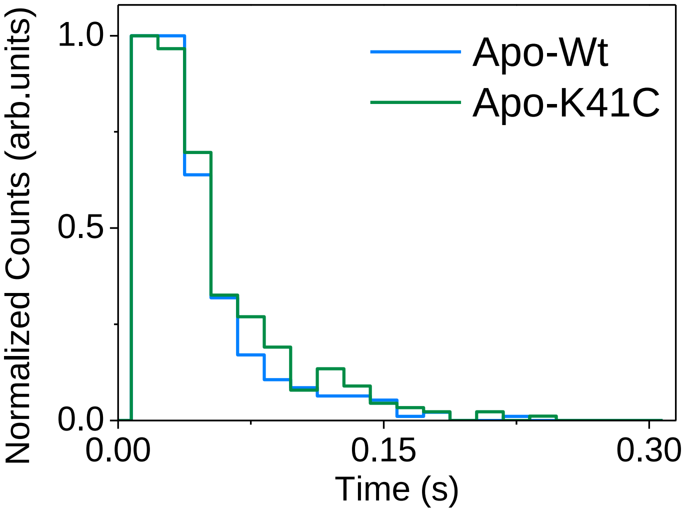

Figure 5.13. The lifetime of the observed *blinks* for Apo-Wt (blue line) and Apo-K41C (green line) are represented. All the *blinking* traces from the gate dependent single-protein transport were included in the calculation. The counts of both Apo-Wt and Apo-K41C were normalized.

5.2. Electron transport of bioengineered D76C, S89C, and L120C Azurin variants

5.2.1. Electrochemical gate-dependent single-protein transport

Although having comparable results from both EC-STM methods namely dynamic and static, we decided to continue with the static mode, the blinking EC-STM approach, to ensure that no structural modification is caused as a result of protein pulling. In this mode the tip is at the same constant distance throughout all the single-protein experiments. If any STM probe movement happens in the z-axis, it will be immediately evidenced in the transient curve. As criteria to record a single 'blinking' trace, the tunnelling background current before and after the blinking feature (lifetime of a single-protein bridge) should be within 10% difference because of the exponential distance-current dependence.

The D76C, S89C, and L120C mutants were measured at several EC gate potentials, always keeping a constant bias. In that case the EC gate range is selected in a range that covers both oxidized and reduced states of the protein mutants (see chapter 3). Figure 5.14 show the accumulation of several tens of blinking events for each of the three mutants into 2D-maps as a function of the EC-gate potential. Surprisingly, each of this new mutants show strikingly different ETp behaviour between them. D76C show the characteristic ETp behaviour of 2-step tunnelling mechanism, comparable to the Wt. This single point shows no deviation versus Wt, which implies pour or no deviation the main electron pathway inherent of the protein. Additionally to the results found for the Wt, this mutant show a high switching process at the redox mid-point observed in the 2D-map (figure 5.15a). We have previously observed switching behaviour in a Wt single-Azurin junction (figure 5.15b)[23]. J.M. Artés et al. have observed the switching events on the blink formation under electrochemical control. They have correlated this behaviour with the protein redox behaviour (since Zn-Azurin is no longer having this switching). This 2-step tunnelling behaviour is no longer standing for the next two Azurin mutants. S89C that has the point mutation close to Lys41 in terms of outer sphere surface, it was observed that the electron transfer process goes with the same mechanism as for K41C. That means that when we are disrupting the hydrophobic patch where the cofactor is enclosed the electron transfer is being modified.

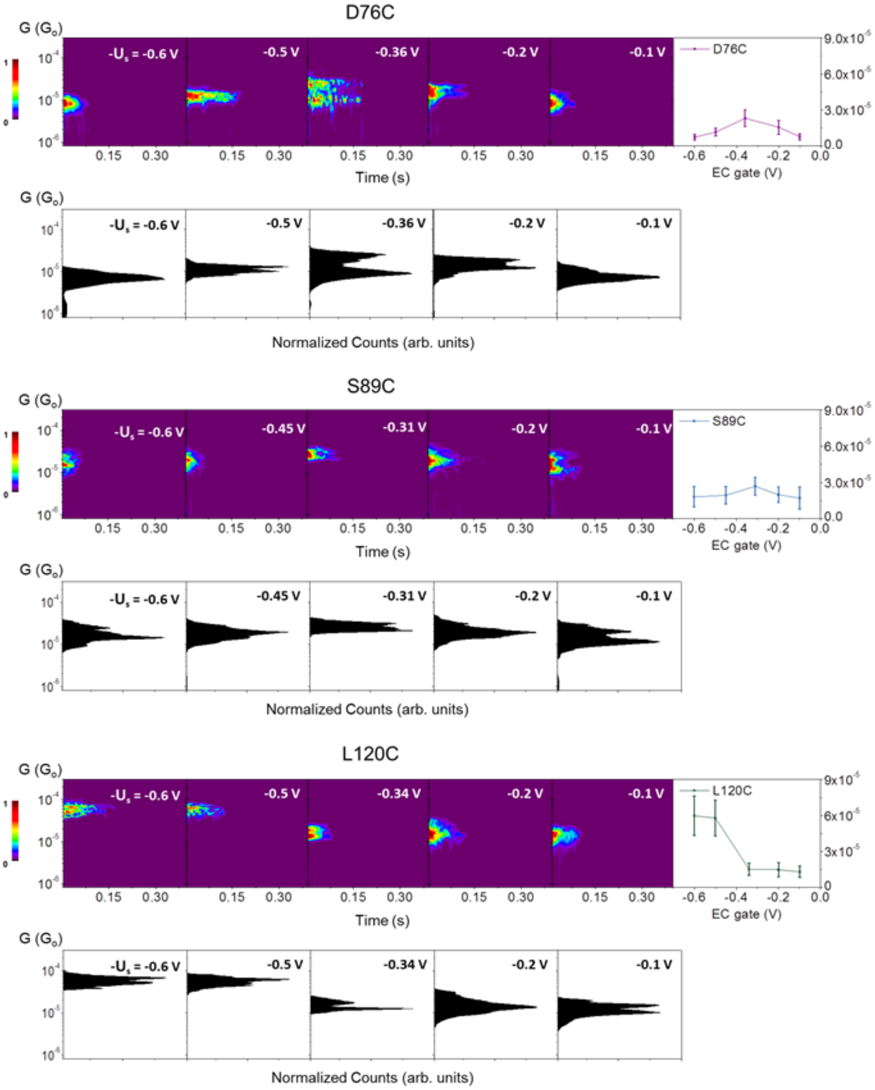

Figure 5.14. Gate-dependent single-protein transport. 2D-blinking maps for D76C, S89C and L120C proteins (D76C top, S89C middle and L120C bottom) at different EC gate potentials. Several tens (up to a hundred) of individual blinking traces like that shown in **a** are accumulated to build each 2D-map without any selection. The counts have been normalized for each map versus the maximum value so that each 2D map has its maximum count set to 1. The far right graphs summarize the average single-protein conductance (G) vs. the EC gate (V) for both studied proteins. The average conductance values were obtained from the Gaussian fits of the maxima in the vertical 1D histogram for each 2D map. The error bars in these plots are extracted from the full width half-maximum (FWHM) of the Gaussian fits.

Finally, L120C has the most different ET behaviour. It presents two conductance levels having a low conductance for reduced copper and a high conductance when the copper is oxidized. This ON/OFF behaviour is attractive for bioelectronics applications. This mechanism has been previously seen for another organic molecules reported in the literature[24]. N. Darwish et al. have shown an organic molecule with this ON/OFF mechanism. They have related this mechanism to the presence of destructive quantum interference between various conductance channels.

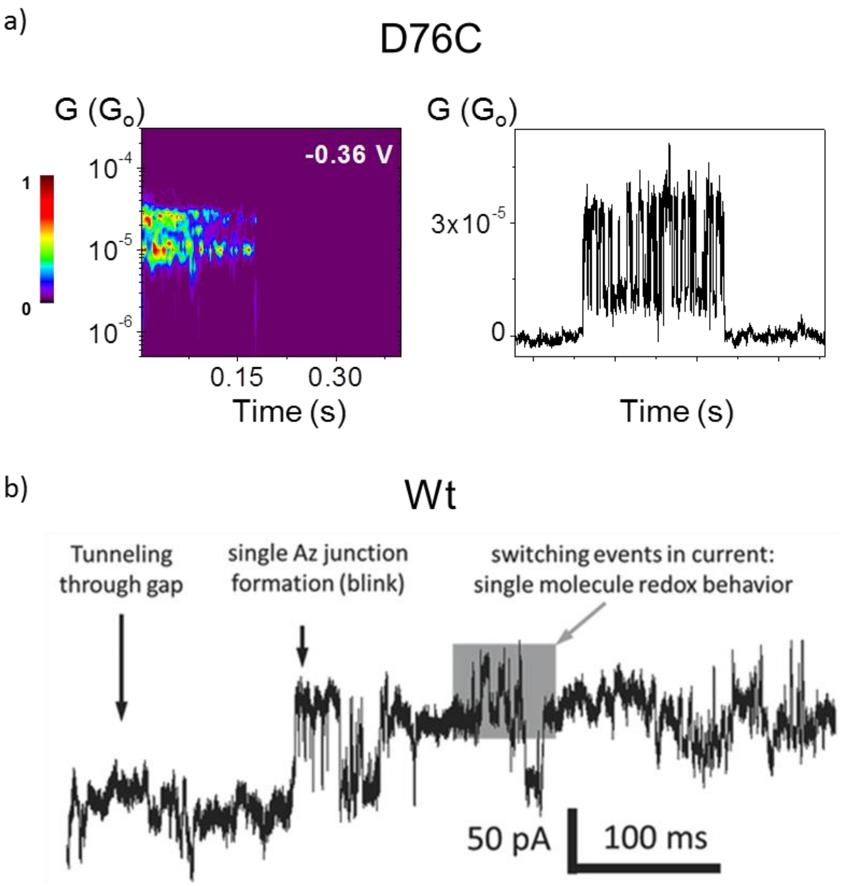

Figure 5.15. a) 2D-blinking map (left image) from the D76C at an EC gate -0.36 V (showed in the figure 5.14) with a representative blink used to construct it (right image). **b)** Example of a single-Azurin junction recording with the fluctuations marked with a grey square[23] (with permission from the journal).

5.2.2. Field Effect Transistor (FET) simulation

To corroborate the three different ETp mechanisms presented by D76C, S89C and L120C, we have simulated a FET analogous experiment. We can profit from the ability to identify single-protein junctions in a blinking experiment to collect I(V) characteristics. As for previous blinking experiments, the STM tip is approach to a tunnelling distance and when it is mechanically stabilized the feedback is removed. In that experiment when the program detects a 'blink' (sudden change in the tunnel current) an I(V) ramp is applied (a single protein is ramped trapped between the two electrodes). The I(V) ramp is done in a smaller time range that the blink lifetime. This current modulation in the junction is achieved by ramping up the probe and sample potentials at a constant bias voltage. Herein the drain and source of a FET system are represented by the EC-STM probe and substrate electrodes, and the gate electrode corresponds to the double electrochemical bilayer. Initially, we set up the blinking experiments at the highest sample potential (EC gate -0.1 mV) and when a blink occurs we ramp it to the lowest EC gate to cover the full range previously done in the point-by-point EC gate blinking experiments. Figure 5.16 show the source-drain current ($I_{SD,}$ current flowing from STM tip to substrate electrode) as a function of the EC gate, where the average is represent as a solid line. The ETp behaviour corresponds to the same observed at fixed EC gate conductance measurements (figure 5.14).

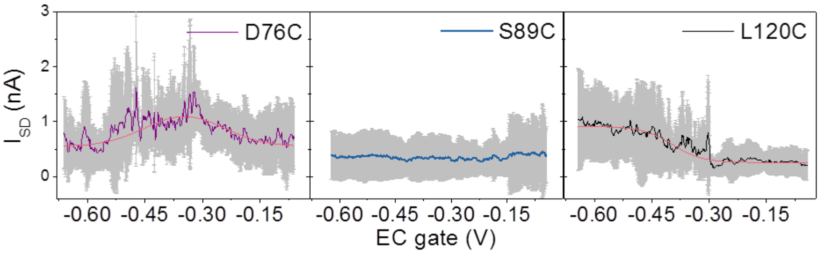

Figure 5.16. Source-drain current (I_{SD}) *vs* Ec gate is represented for D76C, S89C and L120 C mutants. It corresponds to the signal achieved after ramping the range for previous experiments (figure 5.14) directly to the probe-protein-electrode wire. The average for each mutant is represented with a solid line. The experiments were performed in 50 mM ammonium acetate solution (pH 4.55).

5.2.3. Blinking of Apo-proteins:

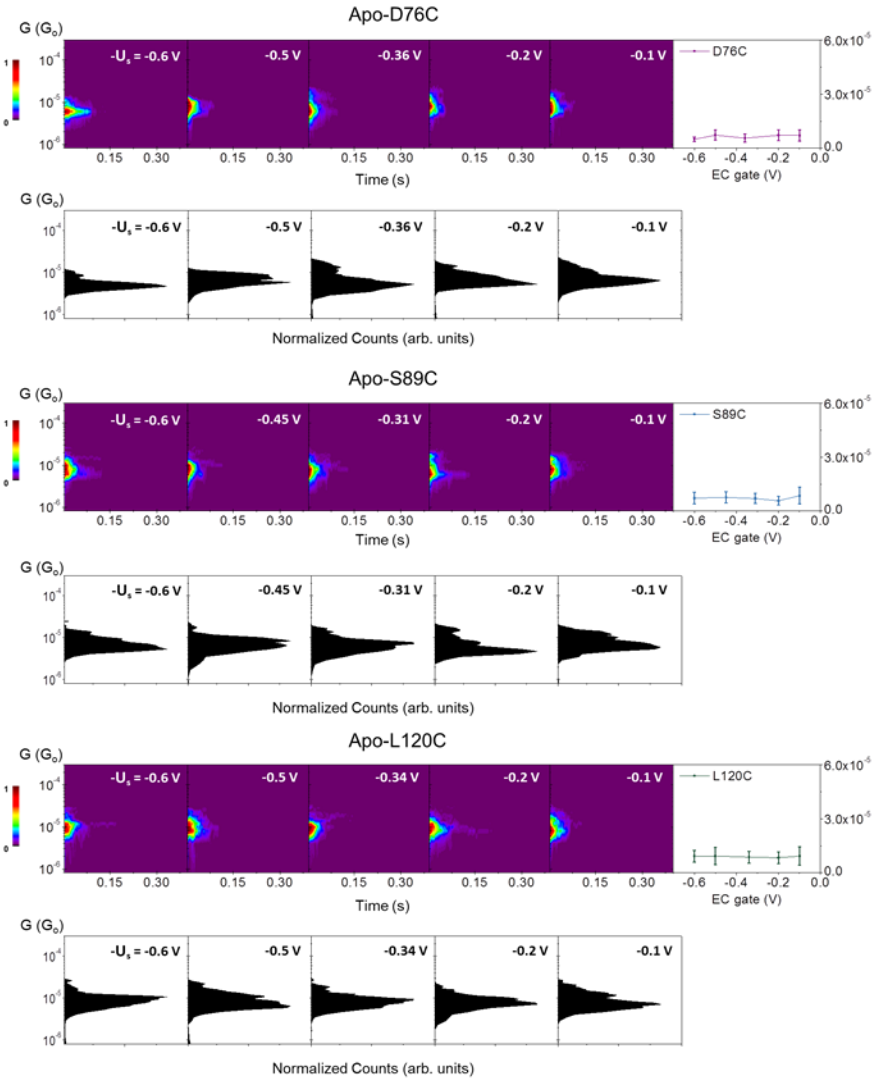

Figure 5.17. Gate-dependent single-Apo-proteins junction transport. Conductance behaviour versus EC gate ($-U_{sample}$ in our EC-STM configuration) at constant bias of 300 mV for the Apo-D76C, Apo-S89C and Apo-L120C. 2D *blinking* maps (top) and 1D histograms (bottom) are shown for each of the mutant proteins. The counts have been normalized for each map versus the maximum value so each 2D map has its maximum count set to 1. The far right graph summarizes the single-protein conductance (G) vs. the EC gate for both studied proteins. The conductance values were obtained from the Gaussian fit maxima of the 1D histogram. The error bars in these plots are extracted from the full width half-maximum (FWHM) of the Gaussian fits.

In order to evidence the role of the Cu centre in the ETp process, as we did for Wt and K41C, we proceed to repeat the ETp characterizations as a function of EC gate for the apo variants. Figure 5.17 represents the 1D histograms and 2D conductance maps for the apo-D76C, apo-S89C and apo-L120C. As for WT, all apo mutants show conductance invariance against EC gate. That evidences again the direct involvement of the Cu centre in any mechanism. On the other hand, S89C is comparable to K41C results where a poor copper participation is evidenced.

5.2.4. Analysis of the single-protein junction lifetimes for D76C, S89C and L120C

The D76C, S89C and L120C lifetimes analyses are represented in figure 5.18. The histograms are built from the extracted lifetimes of each 2D blinking map (X-axis) recorded for holo-mutants (figure 5.14) as well as for Apo-proteins (figure 5.17). The interpretation is in good agreement with the previous results. The lowest scored values correspond again to the apo-proteins, which points toward a mechanical stabilization role of the Cu centre as previously reported[24]. As for K41C, this new 3 mutants also show an enhancement of the lifetimes in comparison to the Wt (holo-proteins). These new bioengineered proteins enhanced the electrode-protein-electrode stabilization.

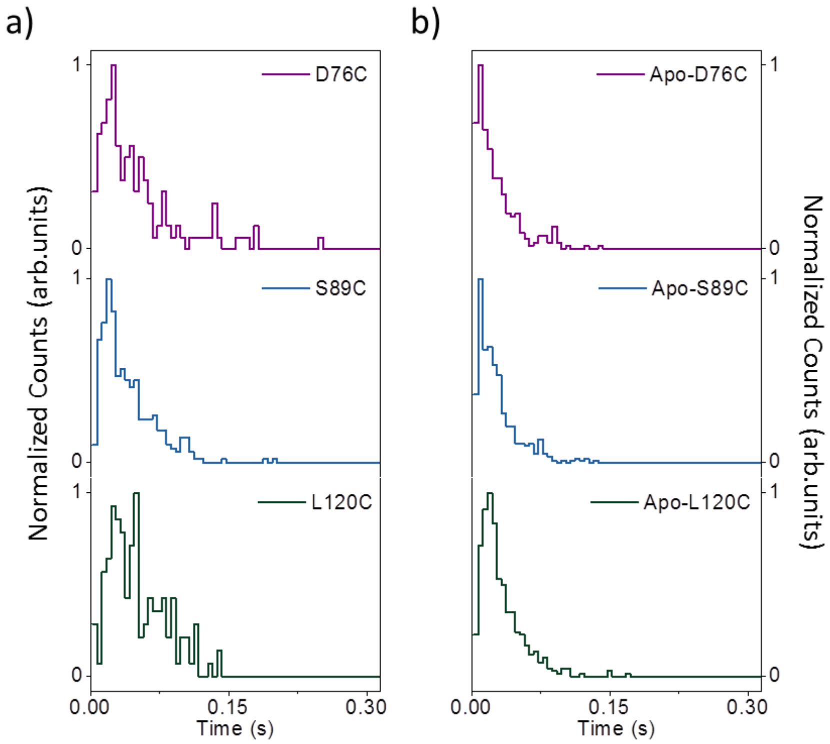

Figure 5.18. The lifetimes of the observed blinks for D76C (purple line), S89C (blue line) and L120C (green line) are represented. Column **a)** corresponds to the holo-proteins while column **b)** are for Apo-proteins. All the blinking traces from the gate dependent single-protein transport were included in the calculation. The counts for all the histograms were normalized.

REFERENCES

1. Xu, B. & Tao, N. J. Measurement of Single-Molecule Resistance by Repeated Formation of Molecular Junctions. *Science (80-.).* **301,** 1221–1223 (2003).

2. Artés, J. M., Díez-Pérez, I. & Gorostiza, P. Transistor-like behavior of single metalloprotein junctions. *Nano Lett.* **12,** 2679–2684 (2012).

3. Chi, Q., Zhang, J., Andersen, J. E. T. & Ulstrup, J. Ordered Assembly and Controlled Electron Transfer of the Blue Copper Protein Azurin at Gold (111) Single-Crystal Substrates. *J. Phys. Chem. B* **105,** 4669–4679 (2001).

4. Sepunaru, L., Pecht, I., Sheves, M. & Cahen, D. Solid-state electron transport across azurin: from a temperature-independent to a temperature-activated mechanism. *J. Am. Chem. Soc.* **133,** 2421–3 (2011).

5. Hihath, J. *et al.* Thermal and electrochemical gate effects on DNA conductance. *J. Phys. Condens. Matter* **19,** 215202 (2007).

6. Artés, J. M. *et al.* Conformational gating of DNA conductance. *Nat. Commun.* **6,** 8870 (2015).

7. Slawomir Sek, *, Aleksandra Misicka, Karolina Swiatek, and & Maicka, E. Conductance of α-Helical Peptides Trapped within Molecular Junctions. (2006). doi:10.1021/JP063073Z

8. Scullion, L. *et al.* Large Conductance Changes in Peptide Single Molecule Junctions Controlled by pH. *J. Phys. Chem. C* **115,** 8361–8368 (2011).

9. Pia, E. A. Della *et al.* Single-molecule mapping of long-range electron transport for a cytochrome b(562) variant. *Nano Lett.* **11,** 176–82 (2011).

10. Aragonès, A. C. *et al.* Electrostatic catalysis of a Diels-Alder reaction. *Nature* **531,** 88–91 (2016).

11. Haiss, W. *et al.* Precision control of single-molecule electrical junctions. *Nat. Mater.* **5,** 995–1002 (2006).

12. Chang, S. *et al.* Tunnelling readout of hydrogen-bonding-based recognition. *Nat. Nanotechnol.* **4,** 297–301 (2009).

13. Aragonès, A. C. *et al.* Highly conductive single-molecule wires with controlled orientation by

coordination of metalloporphyrins. *Nano Lett.* **14,** 4751–6 (2014).

14. Pobelov, I. V., Li, Z. & Wandlowski, T. Electrolyte Gating in Redox-Active Tunneling Junctions⍰An Electrochemical STM Approach. *J. Am. Chem. Soc.* **130,** 16045–16054 (2008).

15. Díez-Pérez, I. *et al.* Ambipolar transport in an electrochemically gated single-molecule field-effect transistor. *ACS Nano* **6,** 7044–7052 (2012).

16. Chi, Q., Farver, O. & Ulstrup, J. Long-range protein electron transfer observed at the single-molecule level: In situ mapping of redox-gated tunneling resonance. *Proc. Natl. Acad. Sci. U. S. A.* **102,** 16203–16208 (2005).

17. Engelkes, V. B., Beebe, J. M. & Frisbie, C. D. Length-Dependent Transport in Molecular Junctions Based on SAMs of Alkanethiols and Alkanedithiols: Effect of Metal Work Function and Applied Bias on Tunneling Efficiency and Contact Resistance. *J. Am. Chem. Soc.* **126,** 14287–14296 (2004).

18. Hines, T. *et al.* Transition from tunneling to hopping in single molecular junctions by measuring length and temperature dependence. *J. Am. Chem. Soc.* **132,** 11658–11664 (2010).

19. Tsuji, A., Kaneko, Y., Takahashi, K., Ogawa, M. & Goto, S. The effects of temperature and pH on the growth of eight enteric and nine glucose non-fermenting species of gram-negative rods. *Microbiol. Immunol.* **26,** 15–24 (1982).

20. Guzzi, R., La Rosa, C., Grasso, D., Milardi, D. & Sportelli, L. Experimental model for the thermal denaturation of azurin: a kinetic study. *Biophys. Chem.* **60,** 29–38 (1996).

21. Migliore, A. & Nitzan, A. Irreversibility and hysteresis in redox molecular conduction junctions. *J. Am. Chem. Soc.* **135,** 9420–32 (2013).

22. Giannotti, M. I. *et al.* Direct Measurement of the Nanomechanical Stability of a Redox Protein Active Site and Its Dependence upon Metal Binding. *J. Phys. Chem. B* **119,** 12050–12058 (2015).

23. Artés, J. M., Lõpez-Martínez, M., Díez-Pérez, I., Sanz, F. & Gorostiza, P. Conductance switching in single wired redox proteins. *Small* **10,**

2537–2541 (2014).

24. Darwish, N. *et al.* Observation of electrochemically controlled quantum interference in a single anthraquinone-based norbornylogous bridge molecule. *Angew. Chemie - Int. Ed.* **51,** 3203–3206 (2012).

6

CONCLUSIONS

6. CONCLUSIONS

We present a mechanistic analysis of bioengineered charge transport in a single-protein wire. We have exploited our static STM-based *blinking* approach[1] to transiently trap individual Cu-Azurin metalloproteins between two metal leads and characterize their electrical properties as a function of the two key experimental parameters for charge transport for such redox molecular systems, namely, the electrochemical gate voltage and the temperature.

The results prove that the conduction channels in the single-protein device can be finely tuned by performing point-site mutations in the outer protein structure involving mild structural changes in the protein backbone.

We have modified a wild-type *Pseudomonas aeruginosa* blue Cu-Azurin at its secondary Cu coordination sphere (*Lys*41 residue) by introducing a *Cys*41 residue that caused minor structural modifications, as seen by both spectroscopy and MD simulations. Such minor structural changes have been ascribed to variations in the hydrophobicity and/or H-bonding network in the protein peptidic structure[2]. The slight reduction of charge density at the Cu centre originated by the newly introduced *Cys*41 residue dramatically alters the charge transport behaviour of the single-protein wire. Our MD simulations of the Au substrate/protein/STM tip junction show that the protein structure is preserved during our measurements, discarding the possibility that these changes arise from any major structural rearrangement. The original 2-step sequential charge transport in the Wt is shut down to give rise to a single-protein wire displaying an almost fully coherent transport mechanism in the mutant. DFT orbital calculations within the relevant segment to the protein transport provide a simple yet intuitive explanation for the observed sharp transport transition, which is based on the lack of contribution of the Cu metal centre in the transport-dominant frontier orbital for the modified protein.

TEM experiments have demonstrated that the bioengineered protein is actually incorporation an opposite anchoring point to wire the protein.

In addition to Lys41Cys we also have successfully bioengineered eight Azurin mutants at its secondary Cu coordination sphere by exchanging a single amino acid for a cysteine achieving: Glus12Cys, Val43Cys, Ala65Cys, Leu68Cys, Asp76Cys, Ser89Cys, Pro115Cys and Leu120Cys. From the structural and electrical characterization we have seen that some effects have been caused to the 3D conformation or to the Cu electronic density in every mutant. Some of them have been modified the active site preserving the overall conformation, while other have shown modification in the secondary coordination sphere while the copper geometry is preserved. The ETp characterization of the Asp76Cys, Ser89Cys, and Leu120Cys has shown three different tunnelling regimes. Asp76Cys presented the original 2-step tunnelling transport from the WT, while the other two have been altered. Ser89Cys, as for Lys41C, has switched its charge transport regime to a fully coherent. Finally, Leu120Cys mutant show a new on/off ETp regime previously seen in an organic molecule[3].

FUTURE PERSPECTIVES

These results demonstrate the feasibility of tailoring the charge transport in a nanoscale bio-molecular device and bring new horizons toward real bottom-up approaches to engineer the next generation of bio-sensors, bio-transistors or any platform requiring the optimization of the biomolecule/electrode electrical communication. The outcomes of this work go beyond a detailed interfacial study of the protein/electrode electrical contact. The observed abrupt transition in the ETp behaviour upon a single external mutation in the protein-protein “docking” patch of a functional redox protein points toward a plausible biological mechanism to control coherence in biological ETp through minor structural changes. Similar mechanisms have been recently suggested in relevant bimolecular structures such as DNA[4].

REFERENCES

1. Aragonès, A. C. *et al.* Electrostatic catalysis of a Diels-Alder reaction. *Nature* **531,** 88–91 (2016).
2. Marshall, N. M. *et al.* Rationally tuning the reduction potential of a single cupredoxin beyond the natural range. *Nature* **462,** 113–6 (2009).
3. Darwish, N. *et al.* Observation of electrochemically controlled quantum interference in a single anthraquinone-based norbornylogous bridge molecule. *Angew. Chemie - Int. Ed.* **51,** 3203–3206 (2012).
4. Liu, C. *et al.* Engineering nanometre-scale coherence in soft matter. *Nat. Chem.* **8,** 941–945 (2016).

APPENDIX A

MOLECULAR DYNAMICS: SIMULATION DETAILS

MOLECULAR DYNAMICS: SIMULATION DETAILS

Here we report the supporting Molecular Dynamics (MD) simulations results which allow us to:

i) quantitatively describe the structural changes on the WT-Azurin introduced by the K41C mutation;

ii) identify the possible adsorption conformations of the WT-Azurin over the Au(111) surface, and subsequently quantify the structural changes induced by such process;

iii) Understand the influence of a gold STM tip on the structural stability of the Wt-Azurin as a function of the tip indentation height.

iv) In what follows, we provide the technical details associated with the MD simulations, which are common to all these sub-sections.

All the simulations were performed using the AMBER14 software suite[13] with NVIDIA GPU acceleration[14–16]. The parmbsc0 modification[17] of the Cornell ff99 force field[18] was used to describe all standard amino acids present in the Azurin. The inter-atomic potentials of the copper atom and its corresponding 5 ligands were described using a force field derived from quantum mechanical simulations[19]. This force-field, has been widely used to model the blue-copper Azurin protein[20–23]. In particular recent experiments[21] have shown how early stages of mechanical unfolding of this protein are well described by this force-field. In all our simulations, the system is fully embedded in a water medium. The water is described using explicit TIP3P model[24], while Joung/Cheatham parameters were used to describe the sodium counter-ions[25,26]. For the gold atoms we have resorted to CHARMM-METAL force-field[27,28], since it is thermodynamically consistent with the AMBERFF used to describe the protein and it has been successfully employed to study inorganic-bioorganic interfaces[28]. We have used periodic boundary conditions and Particle Mesh Ewald (with standard defaults and a real-space cutoff of 10 Å) was used to account for long-range electrostatic interactions. Van der Waals contacts were truncated at the real space cutoff of 10 Å for all the simulations also. SHAKE algorithm was used to constrain bonds containing hydrogen, thus allowing us to use an integration step of 2 fs. Coordinates were saved every 1000 steps.

The X-ray crystallographic structure of Azurin was obtained from the protein data bank (PDB)[29] with the PDB code 4AZU[30]. Protons were added to the protein structure according to the calculated ionization states[31] of its titratable groups, at a pH of 4.5, which corresponds to the one used in the experiments. The resulting structure net charge was zero for Wt-Azurin (with and without the copper atom) and -1 for the mutant K41C. The gold surface used to study the protein adsorption is a (111) surface (along z direction, *i.e.* the direction perpendicular to the surface) with dimensions of 8x8 nm^2 (see figure 4.2. e) along the xy plane and a thickness along the z direction of three atomic layers. In all simulations the gold atomic positions are weakly restrained (with a positional elastic constant of 5Kcal/mol). Note that we have performed one simulation where the gold atoms are unrestrained and we found no difference on the adsorption with respect to the restrained case. At last, the gold tip used to perform the indentation has a radius of 2 nm and the (111) planes are perpendicular to the indentation direction.

For all the simulations here shown the protocol essentially consists of three stages:

i) structures were energy minimized to avoid steric clashes using a combination of steepest descent and conjugate gradient methods;

ii) then, given that all the simulations are performed in a liquid medium, we perform a 2 ns simulation in the NPT ensemble, *i.e.* keeping the pressure constant at 1 atm and the temperature constant at 300K;

iii) at last, given the stabilization of the pressure to 1 atm in the simulation box, and the higher computational cost associated to the NPT simulations with respect to the NVT simulations (Number of atoms, Volume and temperature are fixed), the production MD runs were performed in the NVT ensemble.

APPENDIX B

SYMBOLS AND ABBREVIATIONS

SYMBOLS

E_a	activation energy
E_{ox}	oxidation potential
E_{red}	reduction potential
G	conductance
G_0	quantum contact (or Landauer) conductance
$\hbar$	Plank constant
H_{AB}	electronic coupling
I	intensity
k_{et}	electron transfer rate constant
N	number of samples/objects
R	radius of gyration
RT	room temperature
T	temperature
t	time
T_m	Melting Temperature
U	Potential
U_{Bias}	Bias potential /voltage
U_{probe}	ECSTM probe/tip potential
U_{sample}	ECSTM sample potential
V	Voltage
β	Distance decay factor
γ	Parameter describing the shift of the bias voltage in a redox center
ΔH	enthalpy
ΔS	Entropy
η	Overpotential
λ	The reorganization energy
ξ	Parameter describing the shift of the overpotential in a redox center
φ	Work function
ψ	Probability amplitude
Ψ	Wavefunction
ω	The nuclear vibration frequency
ΔG_0	Driving force for the ET reaction

ABBREVIATIONS

A, Ala	alanine
AFM	atomic Force Microscopy
Ag	silver
AgCl	silver chloride
Apo	without the prosthetic group
Au	gold
C, Cys	cysteine
C	cytosine
Cu	copper
CV	cyclic voltammetry
D, Asp	aspartic Acid
Den	denaturalized
DFT	density functional methods
DNA	deoxyribonucleic acid
DN_{ase}	deoxyribonuclease
DSC	differential scanning calorimetry
E. coli	*Escherichia coli*
EC	electrochemistry/electrochemical
EC-gate	electrochemical gate potential
EC-STM	electrochemical scanning tunnelling microscopy
EDS	energy-dispersive X-ray spectroscopy
EPR	electron paramagnetic resonance
ET	electron transfer
FAD	flavine adenine dinucleotide
FET	field effect transistor
FMN	flavin mononucleotide
FWHM	full width half-maximum
G	guanine
His	histidine
Holo	with the prosthetic group
HOMO	highest occupied molecular orbital
K, Lys	lysine
L, Leu	leucine
LB	culture media
LMCT	ligand-to-metal charge transfer
LUMO	lowest unoccupied molecular orbital

MD	molecular dynamics
Met	methionine
NP	nanoparticle
NPT	constant number (N), pressure (P), and temperature (T)
O/N	overnight
O	orientation
P, Pro	proline
PCR	polymerase chain reaction
PDB	protein data bank
Phe	phenylalanine
Pt	platinum
Q, Glu	glutamine
RMSD	root-mean-square deviation
RNA	ribonucleic acid
RN_{ase}	ribonuclease
S, Ser	serine
S	Sulphur
SAM	Self Assembled Monolayer
SDS-PAGE	sodium dodecyl sulfate- Polyacrylamide gel electrophoresis
SPM	Scanning Probes Microscopy
SSC	Ag/AgCl reference electrode
STM	Scanning Tunneling Microscopy
STM-BJ	Scanning Tunneling Microscopy-Break Junction mode
T7	Standard primer for sequencing
TEM	Transmission electron microscopy
Trp	Tryptophan
Tyr	Tyrosine
UV	Ultraviolet
UV-vis	Ultraviolet–visible spectroscopy
Wt	Wild type
Zn	Zinc

APPENDIX C

PUBLICATION LIST

PUBLICATIONS

- Marta Pozuelo, Pascal Blondeau, Marta Novell, Francisco J. Andrade, F. Xavier Rius, Jordi Riu. Paper-based chemiresistor for detection of ultralow concentrations of protein. *Biosensors and Bioelectronics* 49 (**2013**) 462–465.

- Marta Pozuelo, Albert C. Aragonès, Nuria Camarero, Pau Gorostiza, Ismael Díez-Pérez. Bioengineering Charge Transport in a Single-Protein Wire. Nature Materials. Submitted

- Marco Carini, Marta P. Ruiz, Manuel Melle-Franco, Ismael Diez-Perez, and Aurelio Mateo-Alonso. Exceptionally Small Attenuation Factors in π-Folded Molecular Wires. Accepted

CONGRESSES AND SEMINARS

- M. Pozuelo-Ruiz, J. M. Artés, F. Sanz, P. Gorostiza, I. Díez-Pérez. Studying charge transport in Single-Protein wires. Assistance. 67th Annual ISE Meeting of the international Society of Electrochemistry. **2016** La Haya. Oral presentation.

- M. Pozuelo-Ruiz, J. M. Artés, F. Sanz, P. Gorostiza, I. Díez-Pérez. Studying charge transport in Single-Protein wires. Asistencia. Fuerzas y túnel. **2016** Girona. Poster

- Jornada d'Investigadors Predoctorals Interdisciplinària. **2015** Barcelona.
- M. Pozuelo-Ruiz, F. Sanz, P. Gorostiza and I. Díez-Pérez. Mapping electronic pathways in redox proteins by single-molecule junction measurement. 7th IBEC Symposium. Bioengineering for Future Medicine. **2014** Barcelona. Poster.

- “Single-Molecule Charge Transport in Organometallic systems”, I. Díez-Pérez, A. C. Aragonès, M. Pozuelo, N. Darwish, D. Aravena, E. Ruiz, J. Puigmarti-Luis, D. B. Amabilino, 64rd Annual Meeting of the International Society of Electrochemistry. **2014** Suiza. Presentación oral

- M. Pozuelo-Ruiz, F. Sanz, P. Gorostiza and I. Díez-Pérez. Estudi del Transport Elèctric en Contactes amb una Sola Proteïna. VIII Trobada joves Investigadors Països Catalans. **2013** Andorra. Oral presentation.

- "Mapping electron transport in metalloproteins by using single-molecule junction approaches". M. Pozuelo et al. EC Meeting/School at the University of Bern, Switzerland, **2013**. Oral presentation.

APPENDIX D

RESUMEN EN CASTELLANO

OBJETIVOS

El objetivo principal de esta tesis es la bioingeniería de una proteína para su unión entre dos electrodos. Para este objetivo se seleccionó la azurina como modelo de partida. Es una proteína robusta que presenta alta estabilidad estructural frente al tiempo y la temperatura. Los objetivos específicos de esta tesis han sido:

i) Realizar mutantes de azurina con la ayuda de la bioingeniería con el fin de insertar grupos de anclaje (mutaciones de un solo punto en la capa exterior) para la unión electrodo-proteína-electrodo.

ii) Caracterización estructural y eléctrica de los mutantes de azurina para determinar cualquier perturbación provocada por la mutación puntual.

iii) Estudiar los cambios de conformación 3D producidos por una única mutación puntual.

iv) Estudiar la orientación de anclaje de la Azurina frente a los electrodos.

v) Caracterizar el transporte de electrones en función del potencial electroquímico a través de una única proteína.

vi) Caracterización del transporte de electrones en función de la temperatura.

1. INTRODUCCIÓN

La Transferencia Electrónica (ET) Biológica es el paso clave en muchos procesos celulares básicos como la respiración y la fotosíntesis. La naturaleza ha desarrollado bloques moleculares capaces de transportar carga con una eficiencia sin precedentes. Estos bloques están compuestos por muchas proteínas involucradas en la ET. A través de la comprensión fundamental del mecanismo de ET, se podrá correlacionar las alteraciones en la actividad de la proteína con cambios en la ET. Pero, ¿por qué es importante localizar una función alterada de la proteína? Debido a la estrecha relación entre las malformaciones o ausencia de proteínas con una enfermedad, como por ejemplo: enfermedad de células falciformes (mutación del ADN que interrumpe la hemoglobina, por lo que los vasos sanguíneos son incapaces de transportar oxígeno eficazmente); fibrosis quística (una mutación de ADN afecta a la proteína a cargo del transporte de cloruro de sodio a través de las células); enfermedad de Huntington (la mutación del ADN se traduce en una alteración de la proteína que afecta la capacidad de una persona para pensar, hablar y moverse); etc.

El conocimiento fundamental o la identificación de mutaciones proteicas específicas no son la única ganancia del estudio de ET biológico. Este conocimiento también puede usarse para diseñar dispositivos bioelectrónicos, es decir, explotando la maquinaria molecular ET en biología a nuestro favor, ya que la ET biológica ha mejorado durante miles de años para lograr el comportamiento más eficiente. Por lo tanto, es necesario descifrar el mecanismo ET con el fin de revelar cuáles son los parámetros clave para la transducción de la señal eléctrica entre las biomoléculas activas y los electrodos.

Transferencia electrónica en biología

Componentes redox biológicos

Existen muchos procesos en la vida que requieren la presencia de proteínas transportadoras de electrones. Los procesos más relevantes son la fotosíntesis y la respiración debido a su papel en la producción de la energía principal necesaria para el funcionamiento de la célula. Además, la respiración aeróbica y la fotosíntesis son procesos complementarios, ya que CO_2 y H_2O son los principales componentes nutricionales de los organismos fotosintéticos, que son al mismo tiempo constituyen los productos finales de la respiración aeróbica. Lo mismo ocurre en la dirección opuesta. La producción de energía se encarga de algunos ciclos catabólicos, oxidan compuestos orgánicos a oxígeno y agua y obtienen reductores solubles en agua. Estos reductores donan electrones a la membrana interna mitocondrial, que son manejados por una cadena ET y están acompañados por translocación de protones. La complejidad de los procesos de ET radica en la enorme red de composición de proteínas que son responsables de que el electrón puede moverse distancias largas dentro del tiempo mínimo con la mayor eficiencia.

A lo largo de los años se han desarrollado centros de oxidación-reducción (redox) excepcionalmente eficientes para el proceso ET agrupados dentro de la proteína, conocidos como metaloproteínas o electrón-transferasas. El centro redox en las metaloproteínas desempeña el papel de cofactor o grupo protésico, que se colocan típicamente en un entorno hidrofóbico con enlaces de hidrógeno adicionales proporcionados por la cadena peptídica para ayudar a estabilizar tanto las formas oxidada como las reducidas del cofactor. El cofactor redox podría ser un ion metálico coordinado directamente con la cadena peptídica de la proteína o un pequeño complejo con un ion metálico que está agrupado dentro de la proteína. Los enlaces metal-ligando permanecen intactos tras la transferencia de electrones para minimizar la reorganización de la esfera interna.

Las proteínas redox están a cargo de los procesos ET y algunas pueden difundir libremente. En general, grandes los complejos más grandes de proteínas pueden difundirse de alguna manera en la membrana mitocondrial, pero algunas proteínas más pequeñas, como el citocromo c, la plastocianina o la ferrodoxina, son capaces de moverse a través de distancias más grandes dentro de la célula para conectar los complejos más grandes.

Las proteínas se caracterizan por interacciones muy específicas y afines generando complejos proteína-proteína muy estables, lo que asegura un trasferencia de carga altamente eficiente. Esto se logra mediante la interacción de la región en la esfera externa cercana al lugar del cofactor. La orientación del acoplamiento y la naturaleza de la región de interacción juegan un papel importante. Cuanto más hidrófobo sea la región, más fuerte será el acoplamiento. El electrón sólo propagará cuando para el acoplamiento exacto entre los centros activos.

Cupredoxins

Una de las metaloproteínas más comunes son las cupredoxinas. Las cupredoxinas son transferasas de electrones localizadas en plantas y bacterias. Poseen un solo átomo de cobre. Estas proteínas componen una familia bastante grande de proteínas de transferencia de electrones distribuidas ampliamente en la naturaleza. Tanto las azurinas como las plastocianinas son las más caracterizadas. La plastocianina desempeña su función de transferencia de electrones en el proceso fotosintético en los cloroplastos, conectando el fotosistema I al fotosistema II; Se cree que la azurina transfiere electrones entre el citocromo c-551 a la citocromo oxidasa en las bacterias. La estructura secundaria típica de las proteínas de cobre azul contiene ocho laminas β que forman dos estructuras de hoja β retorcidas que rodean el interior hidrófobo. El ion de cobre se coloca en un parche hidrofóbico en el extremo 'norte' del sándwich, y se coordina con los aminoácidos de ambas láminas β. El cobre está coordinado en una configuración de tetraédrica distorsionada, mientras que en la azurina tiene un ligando extra, que da la geometría bipirámide trigonal. A pesar de que el cobre está en el parche hidrofóbico cuenta con un ligando (histidina) accesible por el solvente. Este aminoácido está al mismo tiempo rodeado de residuos hidrofóbicos. Este parche de esfera externa es el responsable en la mayoría de los procesos de unión para la transferencia de electrones. Al igual que en azurina no se identificaron más sitios para tal transferencia de electrones, para la plastocianina se ha postulado un segundo sitio. Consiste en residuos cargados negativamente alrededor de un residuo de tirosina.

Azurina

En esta tesis hemos seleccionado la proteína Azurina de Pseudomonas aeruginosa. La azurina tiene el centro de cobre tipo 1 con tres fuertes residuos coordinados (His46, His117 y Cys112) y dos ligandos axiales más débiles (Gly45 y Met121) en una geometría tetraédrica distorsionada. Esta proteína es una proteína ampliamente robusta estudiada por varios grupos, que ha sido electroquímica y estructural caracterizada tanto en volumen como a nivel de moléculas individuales. La modificación de los potenciales redox se realiza fácilmente intercambiando residuos de la segunda esfera de coordinación. De hecho, se ha investigado la importancia de las contribuciones de los enlaces de hidrógeno y la hidrofobicidad de los residuos para aumentar el potencial redox. De manera que al jugar con estos parámetros se han alcanzado altos potenciales redox. Met121, un ligando axial del cobre es un aminoácido clave para ajustar los valores redox de la Azurina, a su vez es también un residuo clave para modificar el sitio activo. Estos estudios de bioingeniería han señalado una serie de funciones que el ligando axial puede desempeñar en el centro de cobre azul, incluyendo la protección estérica del ion de cobre de la interacción con el agua y los ligandos exógenos, el control de la geometría del centro de cobre azul y el ajuste de la estabilidad de los estados de oxidación del ion de cobre y, por lo tanto, el potencial de reducción del sitio de cobre azul.

Teoría del transporte electrónico en proteínas

Hemos visto previamente que tanto la respiración como la fotosíntesis son procesos tan importantes en la vida. Implicaban una gran cantidad de transferencia de electrones. En ambos procesos, el gradiente de potencial redox se correlaciona con el gradiente de protones transmembrana, que se conoce como hipótesis quimiosmotica. Este gradiente es generado por proteínas de membrana en su función de transferencia de electrones. El mecanismo para esta transducción de energía biológica está construido por tres componentes:

i) El movimiento de los portadores de electrones entre los principales complejos redox.

ii) El acoplamiento del movimiento de electrones y protones en los sitios específicos para controlar el enlace de la química de formación / ruptura.

iii) El mecanismo túnel. Este caso implica la transferencia de electrones a través del medio sin ninguna transferasa.

La parte iii) trata del túnel de electrones. Pero, ¿cómo funciona? Empecemos por el evento más simple en el que un túnel de electrones. Considerando que un electrón como una partícula libre, que tiene una función de onda, | ψ2 (x) |, que golpea una 'barrera impenetrable', será imposible para el electrón atravesarla de acuerdo con la teoría de la mecánica clásica. Puesto que el electrón tiene una energía más baja, E, que el potencial de la barrera, V. Pero la ecuación de Schrödinger no permite que la función de onda vaya a cero repentinamente. Así que la función de onda y su derivada deben ser continuas y derivarse en todos los puntos. Se ve claramente que la función de onda se convierte en un decaimiento exponencial real (figura 1). La mecánica cuántica presenta una pequeña pero finita probabilidad de encontrar el electrón dentro de la barrera potencial, a pesar de que la mecánica clásica no lo permite. Cuando el electrón penetra la barrera de potencial existe una oportunidad para alcanzar otra región permitida clásica.

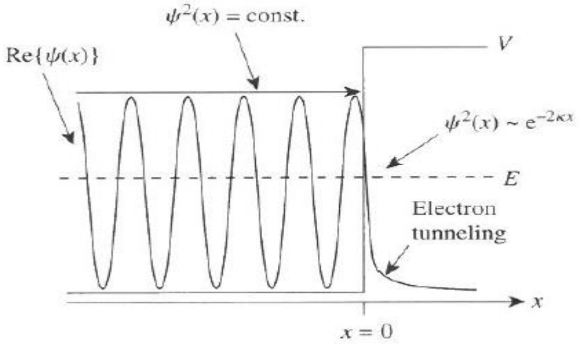

Figure 1. Se muestra la parte real de la función de onda como una partícula libre (izquierda de x = 0) que choca con una región donde V> E y el electrón no se deja entrar clásicamente. La función de onda tiene dos componentes, una parte real, oscilando como cos (kx) y una parte imaginaria (kx) a la izquierda de la barrera, y ambos oscilan entre valores positivos y negativos. La distribución de la probabilidad es el cuadrado de estos componentes, y es constante (recordar sin2 + cos2 = 1).

En la visión mecánica cuántica más simple, el electrón pasará del donante al aceptor y luego de nuevo al donante, y así sucesivamente cuando ambos pozos de energía son de la misma magnitud. En realidad en biología los pozos de energía del aceptor y del donante son ligeramente diferentes. Estas diferentes energías rompen la resonancia de la transferencia de electrones, en este caso dependerá del tiempo.

Teoría de Marcus

Teniendo en cuenta que la transferencia de electrones es una reacción de esfera externa, la molécula que posee el electrón se estabiliza mediante la polarización, que es una contribución de la polarización del disolvente y la polarización procedente de las distorsiones de los enlaces dentro de la molécula. Toda esta polarización es un almacenamiento de energía libre. Cuando se transfiere el electrón, no toda la polarización es transferida y se debe hacer algún trabajo para restaurarla. Este trabajo es lo que se llama energía de reorganización, λ

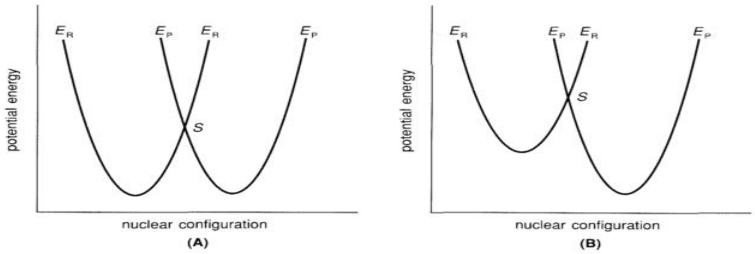

Figure 2. Diagrama de energía potencial: (A) reacción de intercambio propia; (B) reacción cruzada. El punto S representa el complejo activado. ER y EP son las superficies del reactivo y del producto, respectivamente.

El principio de Frank-Condon afirma que la transferencia de electrones ocurre tan rápidamente que el sistema no tiene suficiente tiempo para ser modificado. De esta manera, la transferencia de electrones ocurre en una configuración de núcleos no variable.

Marcus hizo una interpretación del principio de Frank-Condon. Representa con un único oscilador armónico a lo largo de una coordenada de reacción, como el del producto. Ambos pozos mínimos corresponden al estado de equilibrio, teniendo una energía menor el producto y se desplazan a lo largo de la coordenada de reacción para alcanzar la geometría de equilibrio. La variación de la geometría se correlaciona con la energía de reorganización.

La teoría de Marcus afirma que la probabilidad de que un electrón se transfiera de un donante a un aceptor durante un estado de transición disminuye con el aumento de la distancia entre el donante y el aceptor. Los factores que controlan la constante de velocidad de transferencia de electrones implicados en una transferencia de electrones unimoleculares incluyen: la distancia entre el complejo donador-aceptor; La energía de Gibbs de activación; y la reorganización de la energía. La distancia entre el complejo donador-aceptor (r) determina la probabilidad de una transferencia de electrones y es el concepto general de la teoría de Marcus de la transferencia de electrones. La energía de Gibbs de activación (ΔG) está determinada por la energía de Gibbs de reacción estándar (ΔG°) y la energía de reorganización (λ). La energía de reorganización (λ) es un cambio de energía resultante del reordenamiento molecular que se produce cuando la carga se distribuye a lo largo del complejo donador-aceptor en el medio.

Para las reacciones no adiabáticas (interacciones débiles entre los complejos donador-aceptor) es necesario cruzar el estado de transición muchas veces antes de que el electrón se transfiera. En ese caso, la velocidad dependerá del acoplamiento electrónico. En estas reacciones no adiabáticas el electrón atraviesa una determinada barrera de potencial (región no permitida clásica) donde el H_{AB} experimenta, en función de la distancia, un decaimiento exponencial. El electrón cruzará varias veces el punto de intersección hasta que se establezca un acoplamiento débil que permita que el electrón se transfiera.

Para las reacciones adiabáticas -donador-aceptor son altamente acoplamiento por las interacciones de van der Waals y la transferencia de electrones sólo está limitada por H_{AB}, que depende de la frecuencia de movimiento a lo largo de la coordenada de reacción. Por lo tanto, se caracterizan por una transferencia del electrón tan rápidamente debido a la fuerte interacción entre el donante y el aceptor.

Energía de reorganización

Anteriormente hemos visto que para la transferencia de electrones extremadamente rápida la geometría del donador-aceptor no tiene tiempo de ser afectada. Este sistema posee una energía de reorganización baja porque no existe tal requisito de trabajo para construir un ambiente estabilizador. Por lo tanto, es posible relacionar una baja energía de reorganización con una alta transferencia de electrones eficiente y ultra rápida. La reorganización de la energía en las proteínas es controlada por el plegamiento. Como el centro de activación está más agrupado en un parche hidrófobo menor será la energía de reorganización. De modo que, el λ de la esfera externa puede ser disminuido sobre un 50%. Además, el λ de la esfera interior también podría ser controlado mediante el endurecimiento del entorno de coordinación alrededor del sitio activo.

Túnel en proteínas

La transferencia de electrones intraproteína sigue a la dependencia de energía libre similar a Marcus. Muchos ejemplos se encuentran en centros de reacción fotosintética. Dado que la transferencia de electrones por túnel ocurre en el orden de submilisegundos, implica que los cofactores deben estar a no más de 17 Å de la superficie. Esta distancia juega un papel clave para el sitio activo, porque es necesario tenerlo protegido para cualquier aceptor redox exógeno. Sin embargo, cuando una proteína se toma un papel en la transferencia de electrones interproteinica, es esencial que el cofactor no esté a más de 9 Å de la superficie.

Los procesos de túnel ocurren desde temperaturas criogénicas hasta temperaturas ambiente. Esta insensibilidad a la temperatura es lo que caracteriza los procesos túnel. La transferencia de electrones está compuesta por el movimiento del electrón entre el donador-aceptor y el movimiento asociado con la energía de reorganización de los propios núcleos. La transferencia de electrones en biología ocurre comúnmente a través de interacciones débiles entre los complejos donador-aceptor. Esto se debe a los cofactores enterrados dentro de las proteínas que no permiten una interacción directa. Son reacciones no adiabáticas que sólo dependen de la barrera nuclear. Cuando se forma el complejo donador-aceptor se logra una geometría singular. En ese punto ambas energías para el donante y el aceptador son resonantes y sólo en ese instante el electrón puede túnel.

Recorrido del electrón

El camino de los electrones implica dos tipos diferentes de pasos: túnel de enlace directo y espacio de paso. Cada interacción posee un factor de decaimiento diferente. El acoplamiento podría ser fácilmente estimado mediante la inclusión de todos los posibles a través de enlace y el espacio de decadencia entre cada par de átomos de la proteína. Habrá una vía predominante que conecte al donante al aceptor que tenga un valor mínimo de β. β se obtienen fácilmente a partir de estimaciones teóricas, así como a partir de datos experimentales. El acoplamiento electrónico estará dominado por una vía, sin embargo no significa que si una conexión se rompe también lo hará la transferencia de electrones. En ese punto el electrón seguirá otro camino para llegar al aceptador.

Bioelectrónica

Bioelectrónica es un campo interdisciplinario que está aumentando increíblemente rápido. Evolucionó a partir de la necesidad de entender las cuestiones fundamentales y sus prometedoras aplicaciones útiles. Se trata de la combinación de biomoléculas con electrónica, gracias a los avances de la nanotecnología. Pero, ¿cuál es la razón para coger biomoléculas y utilizarlas en electrónica? Dado que la Naturaleza ha logrado durante miles de años de evolución los biocomponentes perfectos, con enzimas (las mejores moléculas catalíticas de la historia) y las biomoléculas que poseen la capacidad de reconocimiento específico y selectivo de otros objetivos (antígeno-anticuerpo, hormona-receptor o dúplex ADN complejos). A través de un intenso estudio bioquímico y biotecnológico de estas biomoléculas, es posible sintetizar nuevas biomoléculas (como enzimas, receptores de proteínas, anticuerpos, etc.) a través de ingeniería genética o bioingeniería para su implementación en sustratos no biológicos. Con esta fuente de nuevos grupos funcionales, se abre una amplia ventana a nuevas aplicaciones. En cuanto a su estudio e implementación, estarán involucrados algunos elementos electrónicos: electrodos, dispositivos de transistores de efecto de campo, cristal piezoeléctrico, medios de grabación de magnetorresistencia, sondas de microscopía de barrido de exploración (STM) y otros.

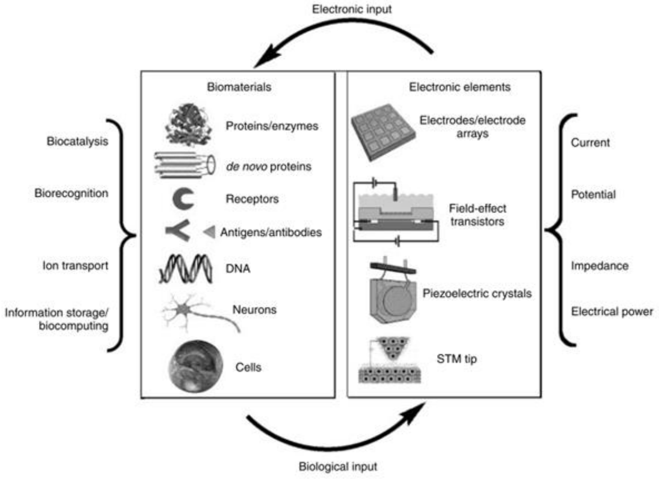
Electronic input
Biomaterials
Electronic elements
Biocatalysis
Biorecognition
Ion transport
Information storage/ biocomputing
Proteins/enzymes
de novo proteins
Receptors
Antigens/antibodies
DNA
Neurons
Cells
Electrodes/electrode arrays
Field-effect transistors
Piezoelectric crystals
STM tip
Current
Potential
Impedance
Electrical power
Biological input

Figura 3. Sistemas integrados de biomateriales y elementos electrónicos para aplicaciones bioelectrónicas.

Los dispositivos bioelectrónicos deben funcionar de dos maneras. En primer lugar, el sistema bioelectrónico debe poder activar la función deseada de la biomolécula. Y segundo, necesita una configuración donde el elemento biológico modifica las propiedades interfaciales del componente electrónico. Esta alteración tiene que ser una respuesta complementaria a la reacción de la biomolécula, por lo que su función podría ser transferida como señal de lectura como impedancia, potencial, transporte de carga o cualquier otra señal electrónica (figura 3).

El aspecto más importante en un sistema bioelectrónico es la cuestión de la transducción. Por lo tanto, es un paso clave que se logra un acoplamiento perfecto de la biomolécula con la parte electrónica. Esta parte esencial condujo a diseñar métodos especiales para inmovilizar biomoléculas en soportes sólidos electrónicos sin interrumpir su actividad nativa / interna. Por supuesto, la biomolécula debe ser estable en esa conformación en períodos de tiempo bastante largos. Hasta ahora se han descrito varios métodos inventivos para la fijación de biomoléculas. El siguiente paso es miniaturizar el dispositivo bioelectrónico, que requiere patrones altamente organizados de biomoléculas sobre el soporte electrónico.

La comprensión fundamental de la transferencia de electrones en los complejos biológicos ha sido estudiada durante las últimas décadas y sigue siendo una cuestión importante en la actualidad, ya que todavía hay mucho por descubrir. Se están desarrollando tanto trabajos experimentales como teóricos para investigar más a fondo estos procesos eficientes. Para estudios de procesos de transferencia de electrones se ha trabajado mucho en metaloproteínas de bioingeniería. Con el coworking experimental y teórico es posible hacer frente al estudio de tal flujo de electrones en proteínas.

El electrodo de acoplamiento biomolécula es una característica esencial para casi todos los sistemas bioelectrónicos. Varias enzimas redox interactúan con otros complejos biológicos para el intercambio de electrones. Entre ellos podemos reconocer proteínas redox, cofactores o sustratos de moléculas. Por lo tanto, si los electrones son transferidos desde el electrodo a la enzima, que es el acoplamiento al electrodo, podría ser posible activar la función biocatalítica de la misma. Esto puede contribuir con un nuevo mecanismo para algunos biosensores amperométricos. Sin embargo, hay algunas proteínas que todavía no tienen un acoplamiento apropiado con el electrodo. Esta falta de comunicación directa de transferencia de electrones entre el electrodo de la biomolécula de la interfaz es uno de los problemas actuales que se resolverán en la bioelectrónica, que podría ser el estado como la mayor dificultad.

2. TÉCNICAS

Las proteínas tienen estructuras terciarias excepcionalmente bien definidas que hacen posible sus funciones dentro de la célula. La estructura es una parte clave en cada proteína, ya que pequeñas variaciones conformacionales pueden producir cambios dramáticos en su actividad. Sorprendentemente, fuera del entorno biológico, las proteínas parecen ser más estables de lo que se esperaba. Esta estabilidad no fisiológica junto con sus características excepcionales en la transferencia de electrónica (ET), reacciones catalizadoras, interacciones de alta especificidad, etc., las hacen prometedoras en el área de la bioelectrónica.

Por ello, ha surgido un campo de bioingeniería de proteínas para la comprensión fundamental del ET y también para el desarrollo de la unión proteína-electrodo en componentes electrónicos. La bioingeniería hace posible a través de algunas modificaciones de proteínas dichas uniones. Aunque, estas alteraciones podrían introducir cambios estructurales que afectan la función de la proteína nativa. Por este motivo son importantes las técnicas de caracterización tanto de las propiedades estructurales como funcionales de las proteínas para comprobar que todo funciona correctamente.

Técnicas de caracterización estructural

Fluorescencia

La fluorescencia de la proteína se origina por los aminoácidos aromáticos intrínsecos triptófano (trp), tirosina (tyr) y fenilalanina (phe). De ellos, trp es el que se destaca, porque su posibilidad de ser selectivamente excitado sin tener contribuciones adicionales de tyr o phe.

La proteína Azurina de Pseudomonas aeruginosa posee un único Trp48 en una región hidrofóbica interna en la proteína. La emisión de fluorescencia para la Azurina nativa esta alrededor de 300 nm cuando el indol se excita a 295 nm. Así, cualquier cambio que afecte estructuralmente a la conformación 3D de la azurina se visualizará en un pico de emisión de fluorescencia desplazado hacia 350 nm.

Espectroscopia ultravioleta-visible (UV-vis)

En proteínas, la absorbancia es una contribución de aminoácidos aromáticos (trp, tyr y phe) y enlaces disulfuro de la estructura proteica. El pico de absorción resultante se localiza entre 240 - 300 nm. Además, las proteínas que contienen un grupo heme o cofactores de cobre tienen bandas de absorción extra en la región visible. En el caso de la Azurina, esta técnica permite observar modificaciones en el sitio activo, ya que la azurina tiene una banda de absorción a 600 nm que se desplaza cuando el sitio activo sufre cualquier interrupción. Es originada por el enlace del cobre al residuo 112Cys.

Técnicas de caracterización eléctrica

Voltamperometría

Las proteínas redox son excelentes en los procesos ET de largo alcance en diferentes funciones celulares. Se puede estudiar el avance de esta característica por electroquímica directa. Las proteínas redox se unen al electrodo de superficie para un intercambio directo de superficie de proteínas de electrones sin ningún mediador. Para ello se deben cumplir algunas condiciones. En primer lugar, la proteína tiene que ser suficientemente estable en la superficie del electrodo para evitar la desnaturalización. Y en segundo lugar, la ET en la interfaz tiene que ser rápida (reversible), lo que requiere una baja energía de reorganización y un alto acoplamiento electrónico entre proteína-electrodo.

Técnicas SPM

Las técnicas de SPM se presentan también como técnicas clave para el desarrollo de la bioelectrónica. Son esenciales para la caracterización de las interacciones interfaciales, así como para caracterización a nivel unimolecular sobre una superficie (comprender la estructura de proteínas, explorar el uso de las propiedades de la proteína para la bioelectrónica) para la miniaturización de los dispositivos.

Nuestro sistema

La microscopía de efecto túnel (STM) ha demostrado su capacidad para estudiar las superficies a nivel atómico/molecular así como para interactuar/manipular dichos átomos/moléculas. Estas habilidades han impulsado el campo de la nanociencia y la nanotecnología. La capacidad de manipulación atómica de una muestra así como la posibilidad de trabajar bajo condiciones prácticas, por ejemplo en aire, medio fisiológico, etc. ha facilitado al STM superar a las microscopías electrónicas para muchas aplicaciones.

En un STM, una sonda metálica afilada se aproxima a una superficie plana y limpia. La sonda STM se aproxima a la superficie hasta que se alcanza una corriente de túnel de pocos picoampers. Debido a la dependencia exponencial de la corriente túnel con la distancia, cada vez que la punta "ve" alguna diferencia en la superficie el valor de la corriente túnel se ve modificado. La señal que se genera se representará como un punto de intensidad. Como consecuencia de la fuerte descomposición exponencial, sólo los átomos más cercanos a la superficie contribuyen al túnel, lo que da como resultado una resolución atómica.

En esta tesis queremos obtener información sobre el transporte electrónico (ETp) de una sola proteína en función de diferentes modificaciones. Para ello hemos utilizado un STM con control electroquímico (EC-STM) ya que permite trabajar en condiciones fisiológicas. Todas las medidas se realizan bajo control bipotenciostático para el control del estado redox de la proteína (potencial de electrodo superficial) al mismo tiempo que se establece la "dirección" del flujo de corriente (potencial de punta).

Más concretamente, hemos utilizado dos metodologías EC-STM para estudiar la conductancia de las uniones uniproteicas: el método dinámico de 'break junction' (STM-BJ) y el método estático "blinking". El modo de trabajo con el STM-BJ se ve esquematizado en la figura 4. La punta STM se retira y se aproxima a la muestra para formar y romper el contacto entre la punta STM y el sustrato. Las curvas que contienen escalones de corriente correspondientes a la unión de la proteína se usan para construir el histograma 1D donde un pico representará el valor de conductancia medio para una sola proteína. Por el contrario, en el método de "blinking" la punta se ajusta a la distancia del túnel de la muestra y el feedback se desconecta. Cuando una proteína se une entre punta y sustrato, se observa un "salto" o "blink" en la corriente túnel en forma de ruido telegráfico (figura 5). Asimismo, la corriente se transforma en valor de conductancia de la unión de una sola proteína. Varias decenas de blinks se utilizan para construir mapas 2D y su correspondiente histograma de conductancia 1D. Los mapas 2D muestran la conductancia frente a la vida útil de los blinks, que proporciona información adicional sobre la estabilidad de las uniones uniproteicas.

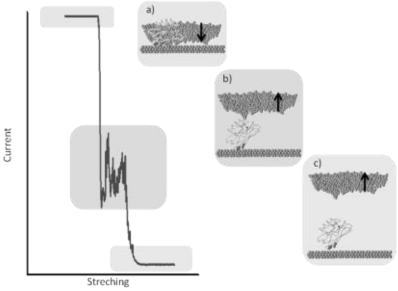

Figura 4. Esquema de la formación de uniones uniproteicas con el modo dinámico del EC-STM (BJ-STM). a) la punta se acerca a la superficie en el momento que la corriente tiene su valor máximo; b) conforme la punta se separa puede producirse la unión punta-proteína-sustrato lo que produce un escalón en la corriente correspondiente a la conductancia de dicha proteína; c) cuando la unión se rompe la corriente decae exponencialmente hasta cero.

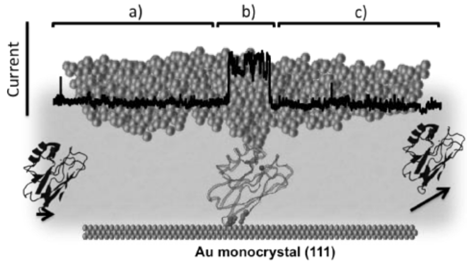

Figura 5. Esquema de la formación de la unión unión uniproteica y la señal obtenida (blink). a) La punta del STM se coloca a una distancia túnel y se quita el control de feedback; b) se produce la unión punta-proteína-sustrato y se observa un salto en la corriente, lo que llamamos blink; c) la unión uniproteica se rompe y la corriente vuelve a su valor inicial establecido.

3. BIOENGENIERÍA DE UN MODEL PROTEICO REDOX

El objetivo de la parte de bioingeniería es introducir un punto de anclaje en la capa externa de proteína para conectarlo entre dos electrodos de oro (punta del STM y electrodo de muestra). La Azurina de *Pseudomonas aeruginosa* es nuestra proteína seleccionada para trabajar. Hemos elegido esta proteína porque es un modelo ampliamente estudiado. Esta azurina específica es una pequeña proteína con un ion cobre que tiene un papel de transportador de carga en la cadena respiratoria de varias bacterias. El cobre está situado en un parche hidrofóbico fuertemente coordinado a tres residuos (His46, His117 y Cys112) con dos contribuciones axiales más débiles (Gly45 y Met121) en una geometría tetraédrica distorsionada. En la superficie opuesta del metal de cobre situado metal hay un puente disulfuro (Cys3-Cys26), que se ha demostrado ser un excelente punto de anclaje a las superficies de oro. A través de la imagen STM hemos observado las proteínas individuales unidas al electrodo de muestra. También se ha caracterizado electroquímicamente y estructuralmente.

Mutante K41C: segunda esfera de coordinación

El primer residuo elegido para mutar es la Lys41. Especialmente Lys41 se destaca como el aminoácido prioritario para la interacción, debido a su grupo de carga lateral que se piensa que está implicado en la interacción con otras proteínas complementarias. Vamos a utilizar estos dos puntos para anclar la proteína en la unión y estudiar el transporte de electrones (ETp) a través del enlace disulfuro Cys3-Cys26 y el nuevo Cys41.

Caracterización

Una vez que producido el mutante K41C, procedemos con la caracterización para estudiar y discernir cualquier cambio que se haya producido en el mutante frente a la Wt.

Caracterización estructural: Métodos espectroscópicos.

Espectroscopia UV-visible.
Los espectros de absorción UV-visible para la Wt y su variante K41C muestran bandas de absorción dentro del intervalo típico de las proteínas de Cu; 634 y 615 nm respectivamente para Wt y K41C. El desplazamiento leve observado para el K41C sugiere una pequeña perturbación del sitio de unión de Cu tras la mutación.

Espectroscopia de fluorescencia

Se midieron tanto las variantes de Wt como de K41C, así como su homólogo desnaturalizado. Ambas proteínas presentan máximos fluorescentes centrados a 315 nm antes de la desnaturalización, lo que indica que ambas proteínas conservan la estructura plegable en 3D y la trp48 mantiene enterrada. Después de la desnaturalización térmica de las muestras (90ºC durante 20 minutos), el pico fluorescente se desplaza a ~ 360 nm, lo que indica que Trp48 ha sido expuesto al disolvente, evidenciando su estado desplegado para ambas proteínas. Por lo tanto, estos resultados evalúan que la estructura plegable en 3D se conserva en la variante K41C con mínimos o no modificaciones frente a la azurina Wt.

Caracterización electroquímica

Voltamperometría cíclica (CV)

Una vez que tenemos una prueba estructural de la conformación 3D de ambas proteínas, probamos su actividad eléctrica por medidas electroquímicas. Se seleccionó la selección del electrodo de trabajo (una superficie funcionalizada con una SAM de hexanotioles) porque la proteína azurina tiene un parche hidrófobo cerca del centro de cobre que permite las interacciones directas de van der Waals con el extremo metilo de los alcanotioles forzando al centro de cobre a estar más cerca de la superficie del electrodo. De acuerdo con las mediciones UV-vis, el potencial medio-redox medido muestra un desplazamiento anódico de ~ 50 mV para el mutante K41C con respecto al Wt, lo que indica una reducción de la densidad de electrones alrededor del centro de Cu con la desestabilización correspondiente del estado de oxidación del Cu (II). Además, la mayor separación de los picos catódicos (E_{red}) a anódico (E_{ox}) evidencia una pérdida de reversibilidad en el mutante K41C frente a la Wt.

Racionalización del ET en proteínas redox

Proponemos a continuación una variedad de mutaciones puntuales en la parte exterior de la Azurina con fines de anclaje. Nos centramos únicamente en el sitio de unión más adecuado para la sonda EC-STM. Enumeramos todos los aminoácidos disponibles en la esfera externa de la proteína. El residuo tiene que ser accesible para la interacción de la punta del EC-STM. Como queremos preservar la estructura terciaria, todos los aminoácidos que forman enlaces de puente de hidrógeno, cuya contribución afirma a la estructura 3D, son rechazados. El último paso fue evaluar varios grupos de aminoácidos que son secuenciales en la cadena peptídica de la proteína. En este punto, la lista ha disminuido a principalmente 8 aminoácidos prioritarios: glutamina (Glu, Q) 12, valina (Val, V) 43, alanina (Ala, A) 65, leucina (Leu, L) 68, ácido aspártico (Asp, D) 76, Serina (Ser, S) 89, Prolina (Pro, P) 115 y Leu120.

Caracterización

Procedemos a través del proceso de caracterización para estudiar los posibles cambios estructurales ocurridos después del intercambio de residuos mediante técnicas de caracterización espectroscópica y electroquímica.

Se esperan variaciones estructurales y diferencias electroquímicas debido al hecho de que un residuo polar no cargado (cisteína) es reemplazar en algunos puntos un residuo realmente diferente en las propiedades de la estructura a. Glu12 es un residuo polar no cargado como cys, pero cys es más hidrófobo. Glu12 no está directamente unido a ningún ligando, sino que está posicionado sobre el sitio de unión de cobre. Es una posición clave cercana al sitio de unión de Azurina para ET con su socio redox. Se espera que esta modificación no perturbe la geometría del centro de cobre. Val43 es un residuo no polar cargado en el parche hidrófobo de la Azurina. En contraste, cys presenta alta polaridad y menos carácter hidrófobo, por lo que se espera que modifique ligeramente la estructura 3D. Los residuos Ala65 y Leu68 están ambos en la hélice α, de modo que estas modificaciones van a interrumpir parcialmente la estructura de la hélice, sin embargo el centro de cobre y la lámina β no deben ser modificados. La hélice está implicada en el aislamiento del trp48 del disolvente, de modo que una interrupción mínima en la hélice afectaría los espectros de fluorescencia. En este caso intercambiamos residuos no polares por uno polar. Además, leu es altamente hidrófobo, mientras que cys no lo es mucho. Asp76 está cerca de la hélice α en la conformación 3D. Por lo tanto, también se coloca en la parte superior de la trp48. Asp es un residuo polar y más hidrofílico que cys. Probablemente afectará la fluorescencia de la trp48, pero no el centro de cobre, ya que está muy lejos de esa región. Ser89 es como cys, residuos polares y sin carga, pero menos hidrófobo. Su ubicación en la estructura plegada está en la misma región que el residuo 41 y 43. Suponemos cambios mínimos en el sitio activo y no hay grandes variaciones en 3D. Tal vez la fluorescencia trp48 mostrará algún cambio porque está muy cerca de los residuos que cubren trp48. Pro115 y Leu120 son residuos contiguos a ligandos coordinados de cobre. Estamos buscando una modificación del sitio activo de cobre, pero preservando la conformación 3D total. Ambos son residuos no polares en contraste con cys, y leu tiene más carácter hidrofóbico que cys.

Caracterización estructural: Métodos espectroscópicos.

Utilizamos de nuevo dos técnicas diferentes: espectroscopia UV-visible aprovechando la banda de absorción típica de las proteínas de cobre y espectroscopia de fluorescencia relacionada con el efecto de la fluorescencia del residuo try48.

Espectroscopia UV-visible.

Seis de ocho mutantes Q12C, V43C, A65C, D76C, S89C y L120C presentan bandas de absorción similares a las del mutante K41C. Todos presentan pequeños cambios azules del pico de absorción entre 11 a 25 nm. Hemos atribuido este efecto a una pequeña perturbación en el sitio de unión de cobre, más específicamente a una disminución de la energía de campo ligando. Para el S89C y el L120C ha aparecido otra banda alrededor de 390 nm. Esta banda corresponde a la transferencia de carga de ligando de pσ (Cys) → CuII a metal. Esta banda es el resultado de un ligando debilitado Cu (II) → S (Cys) por una coordinación axial más fuerte. Para L120C, el aminoácido intercambiado es adyacente al cobre axial coordinado his121. Supusimos que el intercambio del leu ha producido un cambio en la longitud his121-Cu que se refleja en la banda de absorción del Cu (II) → S (Cys). Cys presentan menos interacción estérica que leu, así que quizás el his121 podría penetrar más hacia el centro de cobre. Por otra parte S89C está relativamente lejos de cualquier resto coordinado en la cadena peptídica secuenciada, sin embargo en la conformación 3D se coloca en la parte superior de la cadena lateral de imidazol de la fuerte coordinación his46. El alargamiento del enlace de coordinación Cu (II) → S (Cys112) da lugar a una rotación del d_{x2-y2}, por lo que el estado fundamental del ion Cu (II) se superpone de manera mejor con el orbital pσ de Cys112 que corresponde a un banda de transferencia de carga a mayor energía (~ 400 nm). Finalmente, tanto P115C como L68C muestran un desplazamiento del pico de absorción a ~ 700 nm. Esta banda de absorción débil está relacionada con las transiciones d-d prohibidas. La variante P115C ha modificado un residuo entre dos ligandos fuertemente coordinados al cobre (cys121 y his117).

Espectroscopia de fluorescencia

Para ese conjunto de nuevos mutantes, los resultados en la emisión de fluorescencia de Trp48 podría dividirse en dos tendencias. El primer grupo de mutaciones, que está formado por Val43C, Ala65C, Leu68C, Pro115C y Leu120C, muestra un comportamiento similar al de la Wt: todos ellos tienen un pico de emisión de fluorescencia típico del estado plegado de la Azurina. El pico de emisión de fluorescencia para estos mutantes desnaturalizados térmicamente irreversibles se ha desplazado hacia ~ 360 nm (el mismo comportamiento mostrado por el Wt desnaturalizado). Cuando la proteína empieza a abrir su estructura plegada, el disolvente penetra en el núcleo. Por lo tanto, cuando el trp48 está siendo expuesto al disolvente, su fluorescencia comienza a verse afectada. Val43C, Pro115C y Leu120C muestran los mayores cambios de fluorescencia entre ambos estados, mientras que para Ala65C y Leu68C la diferencia es casi insignificante. Esto evidencia que la mutación está en la hélice que está cubriendo parcialmente el Trp48. Así, en el estado plegado, el nuevo aminoácido puede incorporar una modificación estructural mínima enfrentando un poco al Trp48 hacia el disolvente. Por otra parte, Glu12C, Asp76C y Ser89C no tienen ningún cambio en los espectros de fluorescencia entre la proteína plegada y la proteína desnaturalizada térmicamente, lo que significa que la estructura 3D ha sido modificada por la mutación. Algunas modificaciones en la esfera externa de la proteína podría traducirse en reordenamientos geométricos mínimos. Debido a que la interrupción mínima alrededor del Trp48 que abre una ventana al disolvente se traducirá en una fluorescencia del Trp48 a 360nm. Estas tres variantes de Azurina han incorporado un cambio conformacional 3D que implica una exposición del trp48 al disolvente.

Caracterización electroquímica

Voltamperometría cíclica (CV).

Para Q12C y A65C no se observa actividad electroquímica. Una explicación corresponde a una ligera modificación de estructura en 3D que dificulta o bloquea el flujo de electrones en la interfaz proteína-electrodo. Los residuos 12 y 65 se colocan cerca del parche hidrófobo, que es la región que interactúa con la SAM del electrodo para estas medidas. Otra posibilidad en el caso del Q12C se relaciona con el Trp48 expuesto al disolvente. Es posible que este residuo pueda estar involucrado en el proceso de transferencia de electrones. Por lo tanto, cuando se expone su capacidad de alojar un electrón se vea perturbada. En el caso del P115C sólo se observa el pico de oxidación desplazado hacia valores más altos. Este mutante ha mostrado evidencias de haber sufrido una modificación del sitio activo. Puesto que el campo del ligando de cobre no es el mismo podría haber afectado al mecanismo de transporte de carga. Sin embargo, otra posibilidad podría ser un mayor desplazamiento del pico redox hacia valores negativos debido a un gran aumento de la energía de reorganización. 43C, L68C, D76C, S89C y L120C muestran grandes desplazamientos de los potenciales redox. En la literatura se ve cómo la mutación puntual aumenta los potenciales redox a valores realmente más altos. Es posible que para el caso de D76C y S89C el Trp48 parcialmente expuesto juegue un papel clave, y también afecte aumentando las energías de reorganización, que se aprecia en los picos de separación más altos. Para L68C, S89C y L120C la modificación sufrida por el sitio activo parece desempeñar un papel en ella. Por supuesto, cada modificación no tiene el mismo efecto sobre el potencial redox. Además también depende de la hidrofobicidad, la modificación de las interacciones de puente de hidrogeno y las perturbaciones incluidas en la densidad de electrones alrededor del cobre.

4. MÉTODOS COMPUTACIONALES

Este trabajo descrito en este capítulo está en colaboración con los profesores Juan Carlos Cuevas y Rubén Pérez de la Universidad Autónoma de Madrid. Debido a que hemos modificado una proteína y no tenemos información sobre la estructura cristalina del mutante, necesitamos acceder a la mayor cantidad de información computacional posible sobre su estructura de plegado bajo las condiciones de trabajo. De modo que, en esta colaboración, se realizaron varios cálculos para estudiar las modificaciones de la estructura terciaria del mutante K41C. Los métodos computacionales también brindan la oportunidad de observar la estabilidad de las proteínas cuando están conectadas con un electrodo. Esta rápida evaluación es importante para reforzar la fiabilidad del método, así como la proteína más probable a la orientación superficial

Visualización de los orbitales frontera y cálculo de sus energías

Hemos realizado cálculos computacionales ab initio en el segmento de proteínas estructuralmente relevantes para el transporte de carga, con el fin de visualizar la distribución de los orbitales fronterizos cercanos al centro de cobre para las variantes Wt Azurina y K41C. Debido a las limitaciones computacionales intrínsecas, hemos considerado solamente la fracción de secuencia que implica la primera esfera de coordinación del centro Cu (II) y el segmento de la segunda coordinación incluyendo el residuo mutado en la posición 41: Lys41 (o Cys41 para la variante K41C), Asn42, Val43, Met44, Gly45, His46, His117, Cys112 y Met121. Tal fragmento proteico constituye la vía ET que conecta el parche hidrofóbico expuesto al disolvente de la proteína, que será más accesible al electrodo de punta STM. Los resultados demostraron para la WT una contribución del LUMO significativa en el centro metálico y su primera esfera de coordinación en el estado oxidado de la proteína. En contraposición, para el mutante K41C el LUMO se deslocaliza principalmente al residuo Cys41 mutado, con ninguna contribución al centro activo. La contribución de LUMO en el sitio de metal evidencia la implicación del centro de metal del transporte de carga observado a través de la proteína Wt.

Simulaciones de dinámica molecular (MD)

Las simulaciones de Dinámica Molecular (MD) han proporcionado información clave como: la descripción cuantitativa de los cambios estructurales sufridos en el K41C, identificación de las posibles conformaciones de absorción de la Wt sobre superficies de oro y la comprensión de la influencia en la estructura de la proteína.

Simulaciones de MD de la Azurina en agua: diferencias/similitudes estructurales entre WT y K41C

En esta sección se accede a la estabilidad estructural de tres diferentes estructuras de Azurina: la Azurina Wt, el mutante K41C y la Azurina Apo (sin el centro de cobre), consideradas flotando libremente en una solución de agua.

Hemos analizado la dinámica de las estructuras observando la evolución temporal de la energía total de las tres estructuras de Azurina y se observa que en todos los casos se alcanza un equilibrio térmico antes de los 200 ns de simulación MD. Las configuraciones finales de las tres estructuras obtenidas al final de la dinámica muestran para todas las proteínas una conservación de su estructura inicial. En particular, la mutación parece no tener ningún efecto sobre la estructura global de la proteína. En resumen, nuestras simulaciones de dinámica molecular para las moléculas libres indican que tanto la estructura como la dinámica de estas tres moléculas son muy similares.

Simulaciones de MD de la absorción de la Azurina Wt sobre el sustrato Au (111):

En esta sección, tenemos acceso a cómo la estructura de la Wt-Azurina se ve afectada por su adsorción a una superficie de oro, y también cuáles son las orientaciones de adsorción más probable para la Azurina. Obsérvese que aquí sólo hemos considerado el Wt, dada la similitud estructural entre las tres moléculas consideradas en la sección anterior. En resumen, se observó que a la adsorción al oro de la Azurina parece conservar la mayor parte de su estructura secundaria. Además, partiendo de cuatro configuraciones de adsorción muy diferentes, vimos que la Azurina se adsorbe establemente a lo largo de dos orientaciones diferentes. Estos resultados ponen de relieve que el proceso de adsorción de la proteína se guía a través de dos sitios bien definidos: el parche hidrófobo y puente disulfuro nativo cys3-cys26.

Influencia de la punta STM en la estabilidad estructural de la Azurina

En esta sección, tenemos acceso a cómo la estructura secundaria de la Wt-Azurin se ve afectada por la indentación de una punta de oro. En estas simulaciones, la punta se mueve hacia la superficie, mientras que la proteína adsorbida en la superficie, es libre de moverse y acomodar cualquier deformación. Se observa que la estructura secundaria de la proteína permanece estable hasta distancias de 2,3 nm entre punta y sustrato. Amayor proximidad la helice empieza a perder su configuración.

5. UNIONES UNIPROTEICAS

Después de la expresión, producción y purificación de los variantes de azurina, se estudió el transporte de electrones (ETp) a través de uniones uniproteicas.

Transporte electrónico en la Azurina Wt y K41C

Efecto del potencial de muestra al transporte electroquímico de las uniones uniproteicas

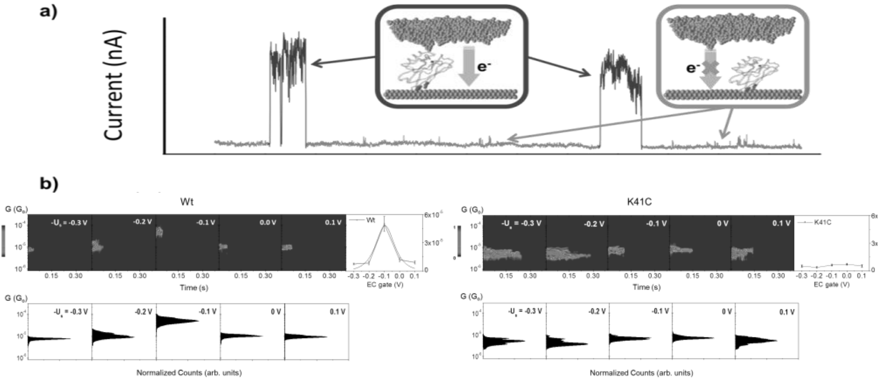

Figura 6. Dependencia del transporte en del potencial de muestra. a) Representación gráfica de las uniones uniproteicas en el modo estático del EC-STM y el tipo de respuesta obtenido (*blinks*). Dichos *blinks* son acumulados en decenas para elaborar los mapas 2D y 1D. b) Mapas de conductancia 2D e histogramas de conductancia 1D representados para las medidas de transporte para la Azurina Wt y la K41C a diferentes potenciales de muestra (el potencial de muestra está representado en signo contrario como EC gate). Ambos histogramas han sido normalizados tomando el valor máximo en cada uno como 1. El gráfico situado a la derecha de los mapas 2D representa el valor medio de conductancia para cada caso, extraído del ajuste gaussiano de los histogramas 1D.

Hemos construido y caracterizado eléctricamente uniones uniproteicas en un ambiente fisiológico para la Wt y la variante K41C. Las proteínas se absorben sobre una superficie de oro. Usando un microscopio de efecto túnel en con control electroquímico (EC-STM) se realizaran las uniones y las medidas de las proteínas. Las simulaciones moleculares en el capítulo 4 mostraron la orientación de absorción de dichas proteínas en el oro. Tanto las simulaciones como los experimentos indican que la fijación de la proteína al sustrato es estable y permite la obtención de imágenes de proteínas redox activas individuales en la superficie del electrodo durante largos períodos de tiempo. Se espera una geometría de anclaje similar para el mutante K41C, dado que este residuo se encuentra en el parche hidrófobo, que es uno de los dos sitios de adsorción preferidos del Wt.

Dos modos de trabajo para el EC-STM han sido usados: *tapping* (modo dinámico) y *blinking* (modo estático). En el primero, el electrodo de punta STM se aproxima y se retrae continuamente hacia/desde el sustrato para formar las uniones uniproteicas mientras que para el modo estático se aproxima la punta al sustrato a una distancia túnel y se espera hasta que la proteína cierra el circuito.

La figura 6 muestra los resultados obtenidos para la Wt y la K41C en dos tipos de histogramas. La franja horizontal observada en los mapas de conductancia 2D representa los valores de conductancia más probables de la unión uniproteica representados en función del potencial de muestra ($U_{muestra}$, donde EC gate = - $U_{muestra}$). Dichos valores están representados en el gráfico de la derecha (extraídos mediante un ajuste de Gauss de los histogramas 1D de conductancia). Estos resultados sugieren un fuerte cambio en el comportamiento de transporte uniproteico, pasando de un transporte túnel en dos pasos para el Wt a un túnel completamente coherente para el mutante K41C.

Dependencia del transporte en función de la temperatura

Para corroborar los anteriores resultados se han medido dichas proteínas en función de la temperatura, ya que el transporte coherente no se ve modificado por la temperatura. En cambio en transporte incoherente se activa térmicamente. La Figura 7 muestra los resultados de conductancia para ambas proteínas, en condiciones de potencial de muestra próximo a sus respectivos potenciales medios redox. El rango de temperatura cubre las condiciones de temperatura ambiente y se aproxima a valores fisiológicamente relevantes (37 ºC). Los valores máximos de temperatura se mantuvieron por debajo de 40 ºC para evitar cualquier desnaturalización de las estructuras proteínicas. Ambos resultados muestran una no dependencia de la temperatura. Esto corrobora los mecanismos expuestos anteriormente, descartando un mecanismo incoherente para cualquiera de las dos proteínas.

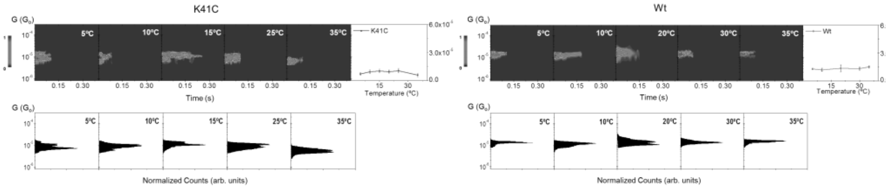

Figure 7. Dependencia del transporte en función de la temperatura. Mapas de conductancia 2D e histogramas de conductancia 1D representados para las medidas de transporte para la Azurina Wt y la K41C a diferentes temperaturas. Ambos histogramas han sido normalizados tomando el valor máximo en cada uno como 1. El gráfico situado a la derecha de los mapas 2D representa el valor medio de conductancia para cada temperatura, extraído del ajuste gaussiano de los histogramas 1D.

Con el fin de corroborar que los blinks observados corresponden a eventos de captura de proteínas individuales, se impusieron separaciones de electrodo-electrodo mayores retrayendo más la punta del STM. En ese momento la punta del STM ya no está en régimen de túnel (distancia de 3.5 nm aproximadamente). Sin embargo, en este experimento se detectaron blinks lo que relaciona las señales con las uniones uniproteicas.

Estabilidad de las uniones uniproteicas

De los ejes X de los mapas 2D se puede extraer información adicional sobre la estabilidad de las uniones. Estos valores corresponden al tiempo que las proteínas son capaces de estar unidas entre ambos electrodos (su estabilidad de unión). Después de analizar los valores obtenidos para ambas proteínas (habiendo considerado todos las blinks obtenidos) se pudo observar que para el mutante estos tiempos eran mayores. Curiosamente, la mutación introducida en la segunda esfera de coordinación del centro de Cu en el mutante K41C mejora la estabilidad mecánica de las uniones de uniproteicas gracias al grupo adicional de anclaje introducido en comparación con la Wt.

Transporte electrónico en los mutantes D76C, S89C y L120C

Efecto del potencial de muestra al transporte electroquímico de las uniones uniproteicas

Los mutantes D76C, S89C y L120C se midieron en varios potenciales de muestra. En ese caso, el intervalo se selecciona en un intervalo que cubre tanto los estados oxidados como los reducidos de los mutantes (véase el capítulo 3). La Figura 8 muestra la acumulación de varias decenas de blinks para cada uno de los tres mutantes en mapas 2D. Sorprendentemente, cada uno de estos nuevos mutantes muestra un comportamiento de ETp diferente entre ellos. D76C muestra el comportamiento característico de ETp del mecanismo de túnel de 2 pasos, comparable al Wt. Adicionalmente a los resultados encontrados para el Wt, este mutante muestra un alto proceso de conmutación en el punto medio redox observado en el mapa 2D. S89C que tiene la mutación puntual cerca del residuo Lys41 en términos de superficie de la esfera externa, se observó que el proceso de ETp corresponde con el mismo mecanismo que para K41C. Esto significa que cuando estamos interrumpiendo el parche hidrófobo donde el cofactor está situado, la transferencia de electrones está siendo modificada. Finalmente, L120C tiene el comportamiento ET más diferente. Presenta dos niveles de conductancia con una baja conductancia para el cobre en estado reducido y una alta conductancia cuando el cobre se oxida. Este comportamiento on/off es atractivo para aplicaciones bioelectrónicas.

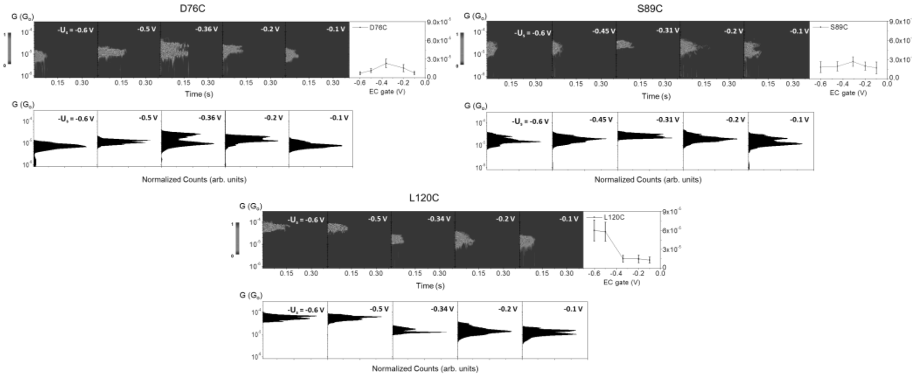

Figura 8. Dependencia del transporte en función del potencial de muestra. Mapas de conductancia 2D e histogramas de conductancia 1D representados para las medidas de transporte para los mutantes D76C, S89C y L120C a diferentes potenciales de muestra (el potencial de muestra está representado en signo contrario como EC gate). Ambos histogramas han sido normalizados tomando el valor máximo en cada uno como 1. El gráfico situado a la derecha de los mapas 2D representa el valor medio de conductancia para cada caso, extraído del ajuste gaussiano de los histogramas 1D.

Simulación de transistor de efecto campo (FET)

Para corroborar los tres diferentes mecanismos ETp presentados por D76C, S89C y L120C, hemos simulado un experimento FET análogo. En ese experimento, cuando el programa detecta un "parpadeo" (cambio repentino en la corriente del túnel) se aplica una rampa I (V). La rampa I (V) se realiza en un intervalo de tiempo más pequeño que el tiempo de unión uniproteica. Esta modulación de corriente en la unión se logra aumentando los potenciales de muestra y punta a una tensión de polarización constante. Con este experimento se pretende aplicar todos los potenciales anteriormente medidos de una sola vez y ver como la conductancia varia. Los resultados muestran comportamientos de ETp correspondientes a los mismos observados en las mediciones anteriores.

Estabilidad de las uniones uniproteicas de los mutantes D76C, S89C y L120C

De igual manera que para la Wt y el K41C se procede a estudiar la estabilidad de la unión uniproteica de estos tres mutantes. La interpretación está en buen acuerdo con los resultados anteriores. Los tiempos de unión para los 3 mutantes muestran una mejora en la estabilidad de unión en comparación con la Wt. Estas nuevas proteínas han sido mejoradas para la estabilización del electrodo-proteína-electrodo.

6. CONCLUSIONES

Hemos presentado un análisis del transporte de carga a través de una sola proteína, realizado con el EC-STM en modo blinking. Los resultados demuestran que los canales de conducción de una sola proteína pueden ser ‘seleccionados’ mediante la realización de mutaciones en la estructura externa de la proteína que implican ligeros cambios estructurales en el esqueleto de esta. Hemos modificado el residuo 41 (lisina41) intercambiándolo por una cisteína, este se encuentra localizado en la segunda esfera de coordinación del cobre. Esta modificación ha introducido pequeñas modificaciones estructurales, como se observó tanto por espectroscopia como mediante simulaciones de MD. Dichos cambios estructurales menores se han atribuido a las variaciones en la hidrofobicidad y los enlaces de hidrogeno en la estructura peptídica de la proteína. La ligera reducción de la densidad de carga en el centro de Cu originada por el recién introducido Cys41 residuo altera el comportamiento de transporte de carga. Nuestras simulaciones de MD de la unión sustrato-proteína- STM muestran que la estructura proteica se conserva durante nuestras mediciones, descartando la posibilidad de que estos cambios surjan de cualquier reordenamiento estructural importante. El transporte de carga secuencial en dos etapas original en la Wt no se ve reflejado en la K41C, sino que esta nueva variante da lugar a un contacto uniproteico que muestra un mecanismo de transporte casi totalmente coherente en el mutante.

Además de Lys41Cys también hemos realizado con bioingeniería ocho mutantes de azurina con éxito. Se ha intercambiado un único residuo en la esfera de coordinación en cada caso obteniendo: Glus12Cys, Val43Cys, Ala65Cys, Leu68Cys, Asp76Cys, Ser89Cys, Pro115Cys y Leu120Cys. De la caracterización estructural y eléctrica hemos visto que algunos han sido afectados a nivel estructural y otros a la densidad electrónica del centro activo. Algunos de ellos han sido modificados cerca del sitio activo preservando la conformación general, mientras que otros han mostrado modificación en la esfera de coordinación secundaria conservando la geometría de cobre. La caracterización ETp de los Asp76Cys, Ser89Cys y Leu120Cys ha mostrado tres regímenes de túnel diferentes.